First Principles Quantum Mechanical Studies of Iridium: A Focus on Bulk and Surface Properties

by

Sharon Joy Grussendorff

Submitted in partial fulfilment of the requirements
for the degree of Doctor of Philosophy in Physics in the
School of Chemical and Physical Sciences,
University of Natal

Pietermaritzburg, 2003

DECLARATION

The work described in this thesis was carried out in the School of Chemical and Physical Sciences, University of Natal, Pietermaritzburg, under the supervision of Dr Nithaya Chetty.

These studies represent original work by the author and have not otherwise been submitted in any formfor any degree or diploma at any university.

Signed: 

S. Grussendorff

Supervisor signature: 

Dr N. Chetty

Abstract

Recent high-pressure experiments on iridium show a transition to a 14 atomic layer superlattice structure. Since iridium has a high bulk modulus, it is used in many high-pressure applications, for instance as a gasket for high-temperature, high-pressure diamond anvil cell experiments. The effects of pressure on this material are hence of interest.

Of the transition metals, the iridium surface has been one of the most extensively studied surfaces experimentally. The field ion microscope has made it possible to observe in detail the behaviour of adatoms on the surface, and has led to interesting discoveries of the nature of atomic adsorption on the Ir(111) surface. A number of theoretical and semi-empirical studies have been made on this topic. However, none of these studies take atomic relaxations into account in a satisfactory manner, and therefore do not give a complete understanding of the process of incorporation of adatoms onto the surface.

In the present work, first-principles total energy calculations based on the plane wave pseudopotential method within the framework of the density functional theory are employed in the study of the bulk properties of iridium, and the crystal phases and defect structures of iridium under pressure. The bond-orientation model is extended to include the effects of pressure, and used to compute all of the $\sim 2^N$ defect structures of iridium as a function of atomic volume.

Allowance for full atomic relaxations is made in computing the ideal and relaxed surface formation energies of the three low-index surfaces of iridium, and in investigating the nature of adsorption of single adatoms on the Ir(111) surface. The formation energy of a vacancy on the Ir(111) surface is also computed. This is the first time such a calculation has been made.

Acknowledgements

I would like to acknowledge the incredible support of my thesis supervisor, Dr Nithaya Chetty, who has very generously supported me not only academically and financially, but also with warm personal support and friendship. I would also like to thank Berenice Meintjes for your spiritual and emotional companionship and support. To my deeply supportive family, my wonderful church community, (Vernon Lund in particular), and my many friends who have hung in there with me, and put up with my ups and downs throughout this process, I want to say a huge and sincere thank you. Thank you to my colleagues in the Science Foundation Programme for your amazing support and understanding. I finally, but most importantly, want to acknowledge God, without whom I most certainly would not have completed this process.

Contents

Chapter 1

Introduction

Iridium is a 5th row transition metal with an extremely high bulk modulus. It has a high degree of thermal and mechanical stability. It is therefore used in a number of high-pressure high-temperature applications, for instance as a gasket for high-pressure diamond anvil cell experiments. The effects of pressure on this material are hence of interest.

Of the transition metals, the iridium surface has been one of the most extensively studied surfaces experimentally. With the field ion microscope, it is possible to observe in detail the behaviour of adatoms on the surface. A number of interesting insights into the nature of atomic adsorption on the Ir(111) surface have hence been made[1,2,3,4,5].

Computational modelling has gained considerable attention in recent years. The development of new and more powerful computers has meant that systems such as iridium, which until recently were extremely difficult to model from first principles, are now relatively easily and accurately modelled. The exponential growth in the speed of

computer processors means that the near future holds even greater possibilities in the area of scientific computing than have been realised until now. The relative cost of computational modelling is low, as only one piece of equipment is required to calculate a wide range of physical properties. Desktop PC's have developed to the extent that they are now able to perform calculations which, a few years ago, were solvable only on expensive supercomputers.

Electronic structure calculations involve the calculation of the total energy by modelling the quantum mechanics of a system. From this energy, one can determine a number of properties of the system, such as the equilibrium lattice constant, the bulk modulus and cohesive energy, the energy of formation of surfaces and defect structures, and phase transitions between the various crystallographic structures of the solid. In addition, the derivative of the energy with respect to the positions of the ions yields the Hellmann-Feynman forces on the ions, which can be used to propagate the ions in such a way as to find the relaxed structure, and hence the minimum energy configuration of the system.

The task of analytically solving anything but the simplest of systems, such as hydrogen, by means of quantum mechanics is an extremely complex and intractable task. In addition, in order to obtain a realistic modelling of defects in a system, a sizable unit cell is required. Efficient numerical algorithms are thus required to enable such modelling to be achievable.

The current work makes use of a set of codes, namely the **B**rookhaven **E**lectronic **ST**ructure Codes (BEST), in which various of these algorithms have been implemented. These codes were developed by Chetty and Weinert during the period 1993 to 1995. They have been used to successfully predict the energetics of a number of solid state systems.[6,7] A dual-AMD-processor desktop PC with 1GBytes of RAM and running at a speed of 1.8GHz per processor was used for the calculations in this thesis.

The theory underpinning the BEST codes is density functional theory (DFT), which was developed in 1964 by Hohenberg and Kohn[8]. As Chapter 2 of this thesis shows, DFT is, in principle, an exact theory which has provided a means of quantum mechanically calculating the total energy of a system in its ground state. It has thus gained considerable attention in recent years, and has been used in many applications to compute the properties of solid state systems. Chapter 2 goes on to discuss the exchange and correlation energy due to interactions between the electrons. In the present work, this energy term is taken into account by means of the local density approximation (LDA).

Among the numerical algorithms which are implemented in the BEST codes is the pseudopotential approximation, in which the ionic core is treated as chemically inert. This is a reasonable assumption since the chemical properties of an atom are primarily determined by its valence electrons. It is therefore possible to replace the strong ionic potential by a much weaker pseudopotential, which mimics the effect of the core on the valence electrons. This weaker pseudopotential is less computationally demanding than the full ionic potential, since it has fewer electrons and smoother pseudo orbitals, and has consequently enabled the solution of electronic structure calculations to be even more accessible. Chapter 3 outlines the history of the development of this approximation, and describes the manner in which pseudopotentials are constructed.

A number of further improvements in the efficiency of total energy calculations are discussed in Chapter 4. The discretisation of the Brillouin zone for the purpose of efficient integration is discussed, with particular reference to the special $\boldsymbol{k}$-point technique, which is the method of choice in the current work. This is followed by a discussion of the Ewald summation, which is a rapidly converging means of computing the interaction energy between the ions in the system. Without the use of this summation, the calculation of this energy involves a slowly converging series. Chapter 4 goes on to outline a number of electronic structure techniques used in the field at present,

examples being the linear muffin tin orbital (LMTO) method, the tight-binding method, and the full potential linearised augmented plane wave (FLAPW) method. The iterative method is then outlined. In particular, the Car-Parrinello molecular dynamics method[9] is presented in detail. This method is computationally more efficient than the usual iterative matrix diagonalisation techniques. Chapter 4 goes on to discuss a variation on this, namely the preconditioned steepest descent (PSD) algorithm[6], which is applied in the current work, together with a subspace diagonalisation which serves to orthogonalise the wavefunctions between successive iterations. Finally, atomic relaxations through the application of the Hellmann-Feynman theorem are discussed, in which the BFGS algorithm[10] is used as the update scheme for the atomic positions.

The mixing of charge densities between successive iterations is an important means of accelerating the convergence of total energy calculations. Three distinct mixing schemes, namely the linear, Anderson, and modified Broyden schemes, are discussed in Chapter 5. Computer codes were developed to implement these schemes, and their relative efficiency is compared in this chapter.

Chapter 6 contains a discussion on the application of electronic structure calculations to iridium. The bulk properties are computed and compared with experimental values. Recent high-pressure experiments on iridium show a transition to a superlattice structure comprising 14 atomic layers[11]. This claim is investigated in this chapter through an application of a novel technique, developed by ourselves, called the "pressure dependant bond-orientation model".

Chapter 7 investigates the energetics of the three principal surfaces of iridium, namely the (100), (110), and (111) surfaces. The results of these computations are compared with other experimental and theoretical results.

The deposition of adatoms on the (111) surface of iridium is investigated in Chapter 8, and the results compared with experimental and theoretical work. The formation energy of the surface vacancy is investigated in this chapter. This is a new result that has not been calculated or measured before.

Finally, a number of concluding remarks are made in Chapter 9. Amongst these are an outline of a way forward for further work to be done on the Ir(111) surface.

Chapter 2

Basic Theory

Quantum theory has provided a very precise means of predicting the total energy of a system of electrons and nuclei, and hence the many physical properties of the system that may be related to the total energy, for instance the equilibrium lattice constants, bulk moduli, phonons, piezoelectric constants, and phase transition pressures and temperatures. In addition, the Hellmann-Feynman theorem enables one to compute forces on the atoms from the gradient of the energy, which enables one to perform first principle molecular dynamics simulations. One may also compute the gradient of the energy with respect to the strain, which yields the quantum mechanical stress on the system. This enables one to calculate, for example, the elastic properties of the system. In practice, however, the exact solution of the Schrödinger equation for a many-body system is impossible to achieve.

2.1 The many-body problem

The non-relativistic Schrödinger equation for a system of interacting electrons and nuclei may be written in the form:

$$\left\{ T_{elec} + T_{ion} + V_{ion-elec} + V_{elec-elec} + V_{ion-ion} \right\} \Phi = E \Phi \quad , \tag{2.1}$$

where T_{elec} is the kinetic energy operator of the electrons, given by

$$T_{elec} = - \frac{\hbar^2}{2m} \sum_i \nabla_i^2 \quad , \tag{2.2}$$

and the kinetic energy operator of the ions, T_{ion}, is:

$$T_{ion} = - \frac{\hbar^2}{2M_I} \sum_I \nabla_I^2 \quad . \tag{2.3}$$

The potential energy due to the ion-electron interactions, $V_{ion\text{-}elec}$, is

$$V_{ion-elec} = - \sum_{i\ I} \frac{Z_I e^2}{|\boldsymbol{r}_i - \boldsymbol{R}_I|} \quad . \tag{2.4}$$

The electron-electron interaction potential is given by

$$V_{elec-elec} = \frac{1}{2} \sum_{i \neq j} \frac{e^2}{|\boldsymbol{r}_i - \boldsymbol{r}_j|} \quad , \tag{2.5}$$

and the interaction potential between the ions is

$$V_{ion-ion} = \frac{1}{2}\sum_{I\neq J}\frac{Z_I Z_J e^2}{|\boldsymbol{R}_I - \boldsymbol{R}_J|} \quad . \tag{2.6}$$

Here the electrons have coordinates $\boldsymbol{r}_i$ and charge -e, and the ions have coordinates $\boldsymbol{R}_I$ and charge $+Z_I\, e$. Hartree atomic units are used, where the distances are measured in Bohr and the energies in Hartree. This sets the values for e^2 , $\hbar$ and m at 1. These factors have been retained in many of the equations for purposes of clarity.

In this formulation, the Hamiltonian is known exactly. The many-body wavefunction Φ must be solved for subject to the constraints of antisymmetry as is required by the Pauli exclusion principle. This problem is intractable for all but the one-electron problem, e.g. hydrogen.

The large mass difference between the electrons and the nuclei, together with the much slower movement of the nuclei compared with that of the electrons, leads to the *Born-Oppenheimer* approximation, otherwise known as the adiabatic approximation. Here the electrons are assumed to be in the ground configuration for the instantaneous positions of the ions. The kinetic energy and the mutual repulsion of the ions is hence constant for a fixed nuclear configuration. Equation **(2.1)** may therefore be simplified to

$$\left\{ T_{elec} + V_{ion-elec} + V_{elec-elec} \right\} \Psi = E\Psi \quad , \tag{2.7}$$

where Ψ is the many-electron wavefunction, related to the many-body wavefunction Φ and the ionic wavefunction $\boldsymbol{\chi}$ by

$$\Phi = \chi \Psi \quad . \tag{2.8}$$

$\Psi(\boldsymbol{r}_1\sigma_1 , \boldsymbol{r}_2\sigma_2 , \ldots \boldsymbol{r}_N\sigma_N)$ is a function of the space and spin variables $\boldsymbol{r}_i\sigma_i$ of the i-th electron. For simplicity, we will use $\boldsymbol{r}_i$ to indicate both the spatial and spin variables in subsequent equations.

In spite of the simplification offered by the *Born-Oppenheimer* approximation, the solution of equation **(2.7)** remains an impossible task for present-day computers beyond the simplest of systems. This is due to the intractable nature of the electron-electron interactions. Direct solution of the Schrödinger equation would require solving approximately 10^{23} coupled differential equations. Further approximations are therefore required in order for a solution to be achievable.

2.2 The Hartree approximation

In the Hartree theory, the ground-state wavefunction of the many-electron system is expressed as the product of orthonormal one-electron spin-orbitals in the form

$$\Psi_0(\boldsymbol{r}_1, \boldsymbol{r}_2, \ldots, \boldsymbol{r}_N) = \psi_1(\boldsymbol{r}_1)\, \psi_2(\boldsymbol{r}_2) \ldots \psi_N(\boldsymbol{r}_N) \quad . \tag{2.9}$$

The set of one-electron Schrödinger equations become:

$$-\frac{\hbar^2}{2m}\nabla^2 \psi_i(\boldsymbol{r}) + V(\boldsymbol{r})\psi_i(\boldsymbol{r}) = \varepsilon_i \psi_i(\boldsymbol{r}) \quad , \tag{2.10}$$

where the first term is the one-electron kinetic energy operator and $V(\boldsymbol{r})$ is the potential in which the electron is moving:

$$V(\boldsymbol{r}) = V_{Hartree}(\boldsymbol{r}) + V_{ion}(\boldsymbol{r}) \quad , \tag{2.11}$$

where

$$V_{ion}(\boldsymbol{r}) = -Ze^2 \sum_I \frac{1}{|\boldsymbol{r}-\boldsymbol{R}_I|} \quad , \tag{2.12}$$

and

$$V_{Hartree}(\boldsymbol{r}) = -e \int \frac{n(\boldsymbol{r}')}{|\boldsymbol{r}-\boldsymbol{r}'|} \, d\boldsymbol{r}' \quad . \tag{2.13}$$

The electron charge density $n(\boldsymbol{r})$ is given by:

$$n(\boldsymbol{r}) = -e \sum_i |\psi_i(\boldsymbol{r})|^2 \quad . \tag{2.14}$$

Here the summation is over all occupied single-electron levels.

The Hartree potential is thus decoupled from the individual motions of all of the electrons in the system, and instead depends simply on the time-averaged electron distribution of the system.

The Hartree approximation was an important breakthrough in the attempts for a solution to the many-body problem. However, it is clear that equation **(2.9)** does not allow for antisymmetry of the wavefunction under the exchange of any two electrons, as required by the Pauli exclusion principle. Nevertheless, the Hartree theory did provide surprisingly good results considering its simplicity.

2.3 The Hartree-Fock approximation

The Hartree-Fock approach was an attempt to improve on the Hartree theory. This approach makes use of a *Slater determinant* of single particle orbitals to ensure antisymmetry of the wavefunction. The expression in **(2.9)** may instead be written in the form

$$\Psi_0(\boldsymbol{r}_1,\boldsymbol{r}_2,\ldots,\boldsymbol{r}_N) = \frac{1}{\sqrt{N!}} \begin{vmatrix} \psi_1(\boldsymbol{r}_1) & \psi_1(\boldsymbol{r}_2) & \ldots & \psi_1(\boldsymbol{r}_N) \\ \psi_2(\boldsymbol{r}_1) & \psi_2(\boldsymbol{r}_2) & \ldots & \psi_2(\boldsymbol{r}_N) \\ \ldots & \ldots & \ldots & \ldots \\ \psi_N(\boldsymbol{r}_1) & \psi_N(\boldsymbol{r}_2) & \ldots & \psi_N(\boldsymbol{r}_N) \end{vmatrix} \quad . \tag{2.15}$$

In addition to the Hartree potential, an *exchange potential* is included in the single-particle Hamiltonian, which arises as a result of this antisymmetry condition. The Hartree-Fock equations are:

$$-\frac{\hbar^2}{2m}\nabla^2\psi_i(\boldsymbol{r}) + V_{ion}(\boldsymbol{r})\psi_i(\boldsymbol{r}) + V_{Hartree}(\boldsymbol{r})\psi_i(\boldsymbol{r}) - e^2\sum_j \int \frac{d\boldsymbol{r}}{|\boldsymbol{r}-\boldsymbol{r}'|}\psi_j^*(\boldsymbol{r}')\psi_i(\boldsymbol{r}')\psi_j(\boldsymbol{r})\psi_i^*(\boldsymbol{r}) = \varepsilon_i\psi_i(\boldsymbol{r}) \quad . \tag{2.16}$$

Surprisingly, the Hartree-Fock approach, in some instances, yields less satisfactory results than the Hartree theory. This is because the electrostatic correlation due to Coulomb repulsion of the electrons has not been taken into account in the Hartree-Fock approximation, and this to some extent screens the exchange effect. The Hartree-Fock approximation does yield fairly good results for single atoms, and for molecular solids, and has thus been used extensively by chemists. However, it fails dramatically for the homogeneous electron gas, which is a prototypical metal, for a number of reasons. The

electrons most important for metallic properties, namely those with energy close to the Fermi energy, are calculated to have infinite velocities within the Hartree-Fock theory. Also, the density of states function, which should resemble that for a free electron gas, instead approaches zero at the Fermi energy, which is an entirely incorrect result for metals.

In order to understand more accurately the reasons for the shortcoming of the Hartree-Fock theory, we will need to take a closer look at the exchange and correlation energy.

2.4 The energy of exchange and correlation

The *exchange energy* is the term given to the reduction in the energy of a many-electron system due to the antisymmetry of the wavefunction, a direct consequence of the Pauli exclusion principle. Qualitatively, the region around an electron of a particular spin will be depleted of other electrons of the same spin, giving rise to an "exchange hole", therefore reducing the overall electron-electron Coulomb energy. The exchange energy is accounted for exactly in Hartree-Fock theory.

The term *correlation energy* is used to describe the difference between the true ground-state energy of the many-body electronic system and the Hartree-Fock approximation for the total energy. In other words it is used to describe all effects on the total energy of the system due to electron-electron interactions that are not accounted for by the Hartree-Fock theory. It is extremely difficult to calculate the correlation energy of a many-electron system. A reliable approximation for the effects of the electron-electron interactions is thus required.

2.4.1 Exchange energy in the Hartree-Fock approximation

When the Hartree-Fock approach is applied to the homogeneous electron gas, with the electronic wavefunctions represented as a set of plane waves

$$\psi_i(\boldsymbol{r}) = \frac{1}{\sqrt{V}} e^{i\boldsymbol{k}\cdot\boldsymbol{r}} \quad , \tag{2.17}$$

the total energy of the N-electron system is evaluated to be:

$$E = N\left[\frac{3}{5}\varepsilon_F - \frac{3}{4}\frac{e^2 k_F}{\pi}\right] \quad . \tag{2.18}$$

When written in the conventional form, with the energy expressed in Rydberg (2 Rydberg≡1 Hartree), we obtain an expression for the energy per electron:

$$\frac{E}{N} = \left[\frac{2.21}{(r_s/a_0)^2} - \frac{0.916}{(r_s/a_0)}\right] Ry \quad , \tag{2.19}$$

where the second term is the exchange term. Here a_0 is the Bohr radius, which has the value 5.2918×10^{-11} m, and r_s is the radius of a sphere whose volume is equal to the volume per electron.

Since the second term in equation **(2.19)** gives an average value for the exchange energy of an electron, Slater[12] suggested that, for non-uniform systems, one could replace the exchange term in equation **(2.16)** by a local energy given by double the exchange energy term from equation **(2.19)**. In other words, he developed an exchange potential, to be added to the Hartree term $V_{Hartree}$, which has the form

$$V_{exchg}(\boldsymbol{r}) = -2.95\left(a_0^{\,3}\, n(\boldsymbol{r})\right)^{\frac{1}{3}} Ry \quad . \tag{2.20}$$

Apparent in this formulation is a resemblance to the local density approximation, which will be looked at in detail in Section 2.4.4. The Hartree-Fock-Slater approach has been used widely by solid-state physicists, particularly in band-structure calculations. Many attempts have been made to improve on the Slater expression in **(2.20)**. One such attempt was the "X_α" approximation[13] in which a semi-empirical parameter α was multiplied by the original Slater expression. One can recognise in the expression for the exchange potential in equation **(2.20)** a precursor to density functional theory, since here the exchange energy is expressed purely in terms of the electronic charge density. It is worth noting that the exchange energy is a non-linear function of the density.

2.4.2 The Wigner approximation for the correlation energy

In the 1930s, Wigner[14] calculated the correlation energy for the electron gas at a high density ($r_s/a_0 = 1$) using second-order perturbation theory. He found the correlation energy per electron to be

$$\frac{E_{corr}}{N} = -\frac{0.88}{7.8} Ry = -0.11\, Ry \quad . \tag{2.21}$$

He then went on to look at the low-density limit, where $r_s/a_0 \geq 20$. At this low density the electrons with a uniform positive charge background can be considered to crystallise in an ordered array. This low density crystal is in a stable state, as the electron-electron potential energy is proportional to $1/r_s$. Since the kinetic energy effects depend upon $1/r_s^2$, at high values of r_s this is not sufficient to oppose the potential energy term which

gives rise to the formation of the ordered array. For this low-density limit, Wigner calculated the ground state energy per electron to be

$$\frac{E_0}{N} = \left(-\frac{3}{r_s/a_0} + \frac{3}{(r_s/a_0)^{3/2}} \right) Ry \quad . \tag{2.22}$$

He then calculated the Hartree-Fock value for the ground-state energy per electron at this low density limit:

$$\frac{E_0^{HF}}{N} = -\frac{2.12}{r_s/a_0} Ry \quad . \tag{2.23}$$

The difference between the Hartree-Fock energy and the leading term in equation **(2.22)** yield a value for the correlation energy per electron up to terms of the order $(r_s/a_0)^{-3/2}$:

$$\frac{E_{corr}}{N} = -\frac{0.88}{r_s/a_0} Ry \quad . \tag{2.24}$$

Interpolating between these high-density and low-density values for the correlation energy, Wigner obtained the following formula for the correlation energy per electron:

$$\frac{E_{corr}}{N} = -\frac{0.88}{r_s/a_0 + 7.8} Ry \quad . \tag{2.25}$$

Use of this approximation for the correlation energy yields a vast improvement to the calculated cohesive energy, compared with Hartree-Fock values[15].

2.4.3 The Gell-Mann and Brueckner calculation

In 1957 Gell-Mann and Brueckner[16] performed an exact calculation of the leading terms in the expansion of the ground-state energy in the high-density limit ($r_s/a_0 \ll 1$) for the electron gas using a field-theoretic approach. They showed that, instead of ending the series expansion at the first divergent term, but rather summing over all such divergent terms, a convergent result is obtained. In this manner they obtained the following rigorous result for the ground-state energy per electron:

$$\frac{E_0}{N} = \left[\frac{2.21}{(r_s/a_0)^2} - \frac{0.916}{(r_s/a_0)} + 0.062 \ln (r_s/a_0) - 0.096 + O(r_s/a_0) \right] Ry \quad . \qquad \textbf{(2.26)}$$

Here the first two terms are precisely the expression given in equation **(2.19)** as a result of the Hartree-Fock approximation. The remaining terms are hence an exact expression for the correlation energy per electron in this high density limit. Since for metals the value of r_s/a_0 ranges between 2 and 6, this result is not of particular relevance. It does, however, indicate a breakthrough in the ability to accurately take into account the effects of the electron-electron interactions.

2.4.4 The local density approximation (LDA)

In this approximation, the exchange-correlation energy of an electronic system is constructed by assuming that the exchange-correlation energy per electron at some point ***r*** is equal to that for a homogeneous electron gas which has the same density as the system under consideration.

The form for the exchange-correlation energy is thus taken as:

$$E_{xc}^{LDA}[n(\boldsymbol{r})] = \int \varepsilon_{xc}(n(\boldsymbol{r}))\, n(\boldsymbol{r})\, d\boldsymbol{r} \quad , \tag{2.27}$$

where $\varepsilon_{xc}(n(\boldsymbol{r}))$ is the exchange-correlation energy per electron of the homogeneous system with density n at point $\boldsymbol{r}$.

Hence

$$V_{xc}(\boldsymbol{r}) = \frac{\delta[n(\boldsymbol{r})\, \varepsilon_{xc}(n(\boldsymbol{r}))]}{\delta n(\boldsymbol{r})} \quad , \tag{2.28}$$

with

$$\varepsilon_{xc}(n(\boldsymbol{r})) = \varepsilon_{xc}^{hom}(n(\boldsymbol{r})) \quad . \tag{2.29}$$

Our work makes use of the Perdew and Zunger[17] parametrizations for $\varepsilon_{xc}^{hom}(n(\boldsymbol{r}))$. This parametrization is based on the quantum Monte Carlo calculations of Ceperley and Alder[18] on homogeneous electron gases at various densities. The parametrization uses interpolation formulas to link these exact results for the exchange and correlation energy at many different densities. This is discussed further in Appendix B on page 148.

2.4.4.1 Reasons for the success of the LDA

Although the local density approximation relies on an assumption that the electron density varies slowly, even in the case of rapid variation, the expression has been shown to be highly accurate[19]. One of the reasons for its accuracy is the fact that it gives the correct sum-rule for the exchange-correlation hole. In other words, there is an electronic charge equivalent to that of one electron excluded from the neighbourhood of the electron at point $\boldsymbol{r}$.

Various attempts have been made to improve on the LDA by taking inhomogeneities into account, for instance gradient expansion methods. However, only those attempts that take this sum-rule into account show notable improvements over the LDA [20,21].

A second reason for the LDA's accuracy is the cancellation of the errors in the approximation of the exchange and correlation energy. For instance, since the correlation energy is approximately one tenth the magnitude of the exchange energy, the 10% error in the exchange energy in atoms is partially compensated for by the 100% to 200% error in the correlation energy[22].

Alternative approaches to that of the LDA have been developed. A few of these are discussed in Appendix C on page 152.

2.4.5 Gradient corrections

As a consequence of the limitations of the LDA, corrections have been attempted which involve the introduction of a dependence of the exchange-correlation energy on the gradient of the density.

2.4.5.1 The gradient expansion approximation (GEA)

In the original Hohenberg-Kohn and Kohn-Sham papers, a gradient expansion, based on the polarizability of the homogeneous electron gas, was introduced. It was suggested for application in slowly varying systems. It has subsequently been shown to fail, due to the non-convergence of the gradient expansion for strongly inhomogeneous systems. Also, the GEA exchange hole, which should be negative, turns out to be positive, and does not

integrate to a value of -1, as it ought to[23]. This approximation has hence not been used in calculations.

2.4.5.2 The generalised gradient approximation (GGA)

The *generalised gradient approximation* (GGA) was defined in the eighties[24,21]. Here, the next term in the derivative expansion of the charge density is included in the approximation to the exchange-correlation energy:

$$E_{xc}^{GGA}[n(\boldsymbol{r})] = \int \varepsilon_{xc}^{GGA}(n(\boldsymbol{r}), \nabla n(\boldsymbol{r}))\, n(\boldsymbol{r})\, d\boldsymbol{r} \quad . \tag{2.30}$$

Early forms of the GGA gave good improvements over the LDA where the LDA had failed, particularly for the binding energy of molecules. The two most widely used forms of the GGA are the PW91 and the PBE functional, which we will discuss briefly below.

The PW91 was developed by Perdew and Wang[25], and was constructed by introducing a real-space cut-off of the long-range component of the density-gradient expansion for the exchange-correlation hole. Although this approximation has been applied successfully in many instances[26], it has recently been discovered that there are some unphysical wiggles in the PW91 potential. It also relies on a large number of parameters, making it rather unwieldy.

Perdew, Burke and Ernzerhof[27] developed a simplified version of the GGA functional, namely the PBE functional, which improves markedly over the PW91[26] , particularly for linear response of the uniform electron gas. The results for the structural properties of solids are similar for the PW91 and PBE functionals, but there are no wiggles in pseudopotentials constructed using the PBE functional. The PBE approximation offers more accurate results than does the LDA for atomic total energy calculations and first

ionisation energy values but, at times, overcompensates for the high binding energy values in clusters computed using the LDA. The PBE offers no vast improvement over the LDA when applied to solids. Since the LDA is less complex, and hence computationally less demanding, it is the functional of choice in the present work.

2.5 Density functional theory

2.5.1 Introduction

The breakthrough which revolutionised the field came in 1964 when Hohenberg and Kohn[8] suggested that, rather than using the many-electron wavefunction as the fundamental variable of the system, the electron density be used instead. They showed that the ground state density $n(\boldsymbol{r})$ of a many-electron system uniquely determines the external potential $V(\boldsymbol{r})$. All of the ground state expectation values therefore depend uniquely on $n(\boldsymbol{r})$. This reduces the basic variable of the system from being 3N-dimensional, in the case of the many-electron wavefunction Ψ, to being 3-dimensional.

2.5.2 Basic density functional theory

2.5.2.1 Density as a basic variable

For an interacting N-electron system in an external potential $V(\boldsymbol{r})$, knowledge of the ground state density $n(\boldsymbol{r})$ uniquely determines $V(\boldsymbol{r})$:

Proof:

Consider the external potential $V(\boldsymbol{r})$ of a system with associated ground state density $n(\boldsymbol{r})$, total number of particles $N=\int n(\boldsymbol{r})d\boldsymbol{r}$, Hamiltonian H, ground state wavefunction Φ and energy E,

$$n(\boldsymbol{r}) \rightarrow V(\boldsymbol{r}) \quad . \tag{2.31}$$

Here the total ground-state energy E of the system is defined in the following way:

$$E = \langle \Phi | H | \Phi \rangle \quad . \tag{2.32}$$

Hence:

$$E = \langle \Phi | V | \Phi \rangle + \langle \Phi | (T+U) | \Phi \rangle \quad , \tag{2.33}$$

where the first term in equation **(2.33)** is the expectation value of the external potential operator, and the second term is the expectation value of the kinetic and interaction energy operators. We can write the first term as:

$$\langle \Phi | V | \Phi \rangle = \int V(\boldsymbol{r})\, n(\boldsymbol{r})\, d\boldsymbol{r} \quad , \tag{2.34}$$

and the second term can be written as:

$$F[n(\boldsymbol{r})] = \langle \Phi | (T+U) | \Phi \rangle \quad . \tag{2.35}$$

Hence we can write the energy functional $E[n(\boldsymbol{r})]$as

$$E[n(\boldsymbol{r})] = \int V(\boldsymbol{r})\, n(\boldsymbol{r})\, d\boldsymbol{r} + F[n(\boldsymbol{r})] \quad . \tag{2.36}$$

Consider a second system of N particles with $V'(\boldsymbol{r}) \neq V(\boldsymbol{r}) + C$, and therefore $\Phi' \neq \Phi$, and energy functional written as

$$E'[n'(\boldsymbol{r})] = \int V'(\boldsymbol{r})\, n'(\boldsymbol{r})\, d\boldsymbol{r} + F'[n'(\boldsymbol{r})] \quad . \tag{2.37}$$

By the Rayleigh-Ritz variational principle we have

$$\begin{aligned} E[n(\boldsymbol{r})] &= \int V(\boldsymbol{r})\, n(\boldsymbol{r})\, d\boldsymbol{r} + F[n(\boldsymbol{r})] \\ &< \int V(\boldsymbol{r})\, n'(\boldsymbol{r})\, d\boldsymbol{r} + F[n'(\boldsymbol{r})] \\ &= \int V(\boldsymbol{r})\, n'(\boldsymbol{r})\, d\boldsymbol{r} - \int V'(\boldsymbol{r})\, n'(\boldsymbol{r})\, d\boldsymbol{r} + \int V'(\boldsymbol{r})\, n'(\boldsymbol{r})\, d\boldsymbol{r} + F[n'(\boldsymbol{r})] \quad . \end{aligned} \tag{2.38}$$

Hence

$$E[n(\boldsymbol{r})] < E'[n'(\boldsymbol{r})] + \int \left(V(\boldsymbol{r}) - V'(\boldsymbol{r})\right) n'(\boldsymbol{r})\, d\boldsymbol{r} \quad . \tag{2.39}$$

Similarly,

$$E'[n'(\boldsymbol{r})] < E[n(\boldsymbol{r})] + \int \left(V'(\boldsymbol{r}) - V(\boldsymbol{r})\right) n(\boldsymbol{r})\, d\boldsymbol{r} \quad . \tag{2.40}$$

Adding equations **(2.39)** and **(2.40)** we get

$$(E + E') < (E + E') + \int \left(V(\boldsymbol{r}) - V'(\boldsymbol{r})\right) \left(n'(\boldsymbol{r}) - n(\boldsymbol{r})\right) d\boldsymbol{r} \quad . \tag{2.41}$$

It is clear here that $n'(\boldsymbol{r}) \neq n(\boldsymbol{r})$, otherwise equation **(2.41)** would imply that $(E+E') < (E+E')$. There is therefore a distinct ground state density $n(\boldsymbol{r})$ associated with each potential $V(\boldsymbol{r})$.

2.5.2.2 The energy variational principle

We can express the function $F[n]$, which represents the kinetic and interaction energies of the electrons, as

$$F[n] = T_s[n] + \frac{1}{2}\int \frac{n(\mathbf{r})n(\mathbf{r}')}{|\mathbf{r}-\mathbf{r}'|}d\mathbf{r}d\mathbf{r}' + E_{xc}[n] \quad , \tag{2.42}$$

where the first term is the kinetic energy of non-interacting electrons with density $n(\mathbf{r})$, and the second term is the classical electron-electron interaction energy (the Hartree energy). $E_{xc}[n]$ is the energy of exchange and correlation of the electrons. Equation **(2.42)** is not a unique separation of terms but, for non highly correlated electronic systems, such an expression relegates $E_{xc}[n]$ to a relatively small contribution. Furthermore, based on prior experience, for example the Slater X_α method, such a separation of terms has been found to have practical relevance. The energy functional given by equation **(2.36)** can be shown to be a minimum for the correct ground state density $n(\mathbf{r})$, using the Rayleigh Ritz principle.

Numerous adaptations to DFT have been made in recent years. Some of these are discussed in Appendix A on page 144.

2.5.3 The Kohn-Sham equations

The minimum of the Hohenberg-Kohn energy functional

$$E[n(\boldsymbol{r})] = \int T_s[n] + V_{ion}(\boldsymbol{r})\, n(\boldsymbol{r})\, d\boldsymbol{r} + \frac{1}{2}\int \frac{n(\boldsymbol{r})n(\boldsymbol{r}')}{|\boldsymbol{r}-\boldsymbol{r}'|} d\boldsymbol{r}d\boldsymbol{r}' + E_{xc}[n] \qquad (2.43)$$

gives the exact ground-state energy of the many-body electron system. This functional is stationary with respect to variations in the ground state density:

$$\int \delta n(\boldsymbol{r}) \left\{ \frac{\delta T_s[n]}{\delta n(\boldsymbol{r})} + V_{ion}(\boldsymbol{r}) + \int \frac{n(\boldsymbol{r}')}{|\boldsymbol{r}-\boldsymbol{r}'|} d\boldsymbol{r}' + V_{xc}(\boldsymbol{r}) \right\} = 0 \quad , \qquad (2.44)$$

where $V_{xc}(\boldsymbol{r})$ is the functional derivative

$$V_{xc}(\boldsymbol{r}) = \frac{\partial E_{xc}[n(\boldsymbol{r})]}{\partial n(\boldsymbol{r})} \quad . \qquad (2.45)$$

The number of particles in the system is given by:

$$N = \int n(\boldsymbol{r})\, d\boldsymbol{r} \quad . \qquad (2.46)$$

Minimising the energy functional, subject to the condition that variation in the charge density should leave the number of particles unchanged:

$$\int \delta\, n(\boldsymbol{r})\, d\boldsymbol{r} = 0 \quad , \qquad (2.47)$$

leads to the Euler condition:

$$\frac{\delta T_s[n]}{\delta n(\boldsymbol{r})} + V_{ion}(\boldsymbol{r}) + \int \frac{n(\boldsymbol{r}')}{|\boldsymbol{r}-\boldsymbol{r}'|} d\boldsymbol{r}' + V_{xc}(\boldsymbol{r}) - \mu = 0 \quad , \qquad (2.48)$$

where μ is the Lagrange multiplier associated with the requirement given by equation **(2.47)**. Comparing this with the equivalent equation for a non-interacting set of electrons moving in an effective potential $V_{eff}(\boldsymbol{r})$ leads to the equation:

$$\frac{\delta T_s[n]}{\delta n(\boldsymbol{r})} + V_{eff}(\boldsymbol{r}) - \mu = 0 \quad . \tag{2.49}$$

These two equations are equivalent if

$$V_{eff}(\boldsymbol{r}) = V_{ion}(\boldsymbol{r}) + \int \frac{n(\boldsymbol{r}')}{|\boldsymbol{r} - \boldsymbol{r}'|} d\boldsymbol{r}' + V_{xc}(\boldsymbol{r}) \quad . \tag{2.50}$$

In other words, we are simply required to solve self-consistently the single-particle equations:

$$\left[-\frac{\hbar^2}{2m}\nabla^2 + V_{eff}(\boldsymbol{r}) \right] \psi_j(\boldsymbol{r}) = \varepsilon_j \psi_j(\boldsymbol{r}) \quad , \tag{2.51}$$

with

$$n(\boldsymbol{r}) = \sum_{i=1}^{N} |\psi_i(\boldsymbol{r})|^2 \quad . \tag{2.52}$$

The sum in the above equation is over the N lowest occupied eigenstates. The set of single-particle equations given in equation **(2.51)** are called the Kohn-Sham equations[28]. The ground state energy and electronic charge density of the system can be obtained from self-consistent solution of these equations in the following way: beginning with an estimate of the charge density $n(\boldsymbol{r})$, $V_{xc}(\boldsymbol{r})$ and hence $V_{eff}(\boldsymbol{r})$ are constructed, and a new charge density is obtained from equation **(2.51)** and **(2.52)**.

In equation **(2.51)**, ψ_j and ε_j are, respectively, the Kohn-Sham single-particle wavefunction, and Kohn-Sham eigenvalue of the electronic state j. A common misconception is that the ε_j are the single-particle energies. As yet there is no consensus about their physical interpretation, if they have one. In the self-consistency procedure, they act as Langrange multipliers to ensure orthogonality of the single-particle wavefunctions. Since

$$\sum_{j=1}^{N} \varepsilon_j = \sum_{j=1}^{N} \left(\psi_j , \left[-\frac{\hbar^2}{2m}\nabla^2 + V_{eff}(\boldsymbol{r}) \right] \psi_j \right) = T_s[n] + \int V_{eff}(\boldsymbol{r})\, n[(\boldsymbol{r})] d\boldsymbol{r} \quad , \qquad \textbf{(2.53)}$$

we can obtain the expression for the total ground-state energy of the system:

$$E = \sum_{j=1}^{N} \varepsilon_j - \frac{1}{2}\int \frac{n(\boldsymbol{r})n(\boldsymbol{r}')}{|\boldsymbol{r}-\boldsymbol{r}'|} - \int V_{xc}(\boldsymbol{r})\, n(\boldsymbol{r})\, d(\boldsymbol{r}) + E_{xc}[n(\boldsymbol{r})] \quad . \qquad \textbf{(2.54)}$$

If the exchange-correlation functional $E_{xc}[n(\boldsymbol{r})]$ was known, the exact solution for the ground-state energy and density of the many-body system could be found using numerical techniques. The original interacting system of electrons with exactly known Hamiltonian and intractable solution for the many-body wavefunction has been mapped onto a non-interacting system of electrons whose Hamiltonian is not exactly known in practice, but for which arbitrarily accurate solutions for the electronic orbitals may be found numerically.

2.5.4 Plane wave formulation of the Kohn-Sham equations

A crystalline solid consists of an extremely large number of electrons ($\sim 10^{23}$) moving in a field generated by a similarly large number of ions. Bloch's theorem uses the periodicity of the crystal to reduce this enormous number of one-electron wavefunctions to as few as half the number of electrons in the unit cell of the crystal.

2.5.4.1 Bloch's theorem

At a temperature of 0K, the ions in an ideal crystal are arranged in a periodic formation - the ions are not static, but vibrate about their equilibrium positions. The external potential experienced by the electrons is therefore also periodic with the periodicity of the unit cell.

Bloch showed that a single electron wavefunction in a periodic potential can have the form of a plane wave multiplied by a cell periodic term:

$$\psi_i(\boldsymbol{r}) = e^{i\boldsymbol{k}\cdot\boldsymbol{r}} u_i(\boldsymbol{r}) \quad . \tag{2.55}$$

Here the Bloch periodic term can be expressed in a Fourier series as an expansion of plane waves whose wave vectors are reciprocal lattice vectors of the crystal:

$$u_i(\boldsymbol{r}) = \sum_{\boldsymbol{G}} c_{i,\boldsymbol{G}} \, e^{i\boldsymbol{G}\cdot\boldsymbol{r}} \quad . \tag{2.56}$$

The reciprocal lattice vectors $\boldsymbol{G}$ are defined by

$$\boldsymbol{G}\cdot\boldsymbol{R} = 2\pi n \quad , \qquad n = 1,2,3,\ldots \tag{2.57}$$

for all lattice vectors $\boldsymbol{R}$ of the crystal. Each electronic wavefunction may therefore be written as a sum of plane waves:

$$\psi_i(\boldsymbol{r}) = \sum_{\boldsymbol{G}} c_{i,\boldsymbol{k}+\boldsymbol{G}} \, e^{i(\boldsymbol{k}+\boldsymbol{G})\cdot\boldsymbol{r}} \quad . \tag{2.58}$$

Each electronic wavefunction can hence be expressed in terms of a basis of plane waves at each $\boldsymbol{k}$-point within the first Brillouin zone.

2.5.4.2 The Kohn-Sham equations in reciprocal space

The expansion of the electronic wavefunctions in terms of a plane wave basis allows the Kohn-Sham equations to be expressed in a reciprocal space representation. Substituting equation **(2.58)** into the Kohn-Sham equations **(2.51)** yields:

$$\sum_{G'} \left\{ \frac{\hbar^2}{2m} |\boldsymbol{k}+\boldsymbol{G}|^2 \delta_{GG'} + V_{ion}(\boldsymbol{G}-\boldsymbol{G}') + V_H(\boldsymbol{G}-\boldsymbol{G}') + V_{xc}(\boldsymbol{G}-\boldsymbol{G}') \right\} c_{i,\boldsymbol{k}+\boldsymbol{G}'} = \varepsilon_i c_{i,\boldsymbol{k}+\boldsymbol{G}'} \qquad (2.59)$$

The plane waves with coefficients $c_{i,\boldsymbol{k}+\boldsymbol{G}}$ each have kinetic energy $\frac{\hbar^2}{2m} | \boldsymbol{k} + \boldsymbol{G} |^2$.

In this formulation, the kinetic term energy is diagonal, and the potentials are expressed in terms of their Fourier components. The ionic potential is assumed to be local at this stage. The non-local pseudopotential formulation will be looked at in the following chapter. For smooth potentials, the higher Fourier components decay rapidly to zero, hence one may introduce a plane wave energy cut-off E_{cut}, which reduces the basis set to one with a finite size.

The size of the Hamiltonian matrix given in curly brackets in equation **(2.59)** is determined by the energy cut-off

$$E_{cut} = \frac{\hbar^2}{2m} | \boldsymbol{k} + \boldsymbol{G}_{cut} |^2 \quad . \qquad (2.60)$$

2.5.4.3 Advantages of plane waves

By representing each electronic wave function as an expansion of plane waves, one can obtain systematic convergence with regard to a single parameter, namely the energy cut-off E_{cut}. An example of this is shown in Figure 2.1, where the total energy for iridium has been plotted against the energy cut-off. The plane waves are not localised functions since they cover all space equally. As a result, one does not incur a basis-set bias or superposition error. Calculation of forces is less complex, as one is not required to include the Pulay correction term. (This is discussed further in Chapter 4). The plane wave representation is numerically efficient, with the use of Fast Fourier Transforms to translate between real and reciprocal space.

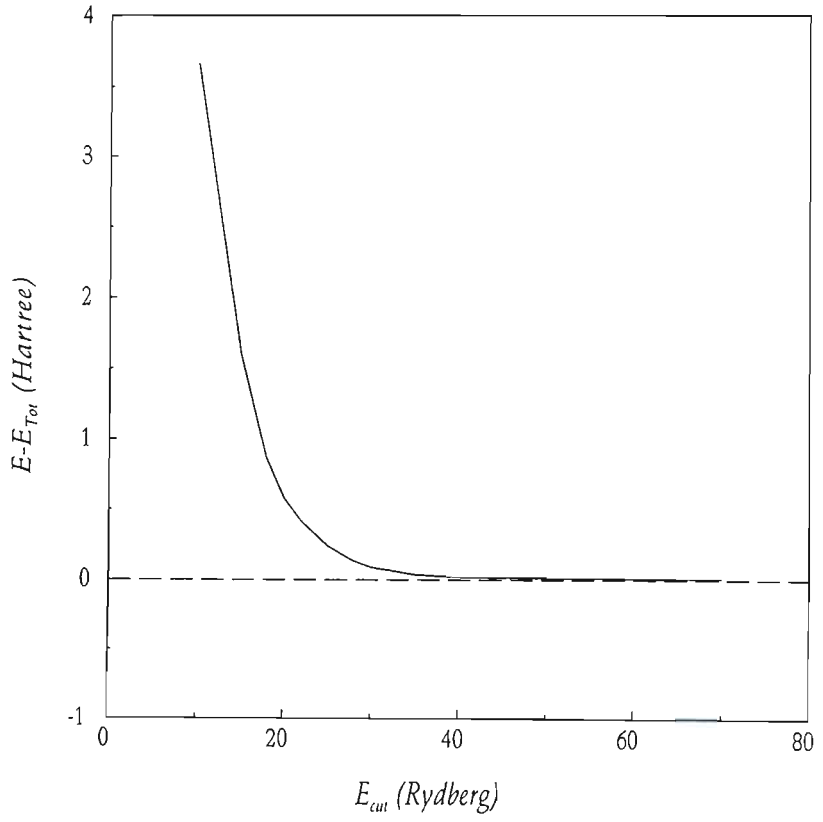

Figure 2.1 Convergence of relative energy with respect to cut-off energy E_{cut}

Chapter 3

The Pseudopotential Approximation

3.1 Introduction

As was shown in the previous chapter, use of Bloch's theorem enables one to express each electronic wavefunction in a periodic solid as a sum of plane waves. However, when using a plane wave basis set, if all of the electrons in the system are to be included in a calculation, the number of plane waves required to expand the tightly bound core orbitals would be very large, incurring a vast computational cost. This is due to the rapid oscillations of the wavefunctions near the nucleus, as the potential in this region is very deep. An example of this can be seen in Figure 3.1, where the iridium 6s valence wavefunction is shown. The rapid oscillations of the valence wavefunctions in the core region ensure orthogonality between the core and valence electrons, as is required by the Pauli exclusion principle.

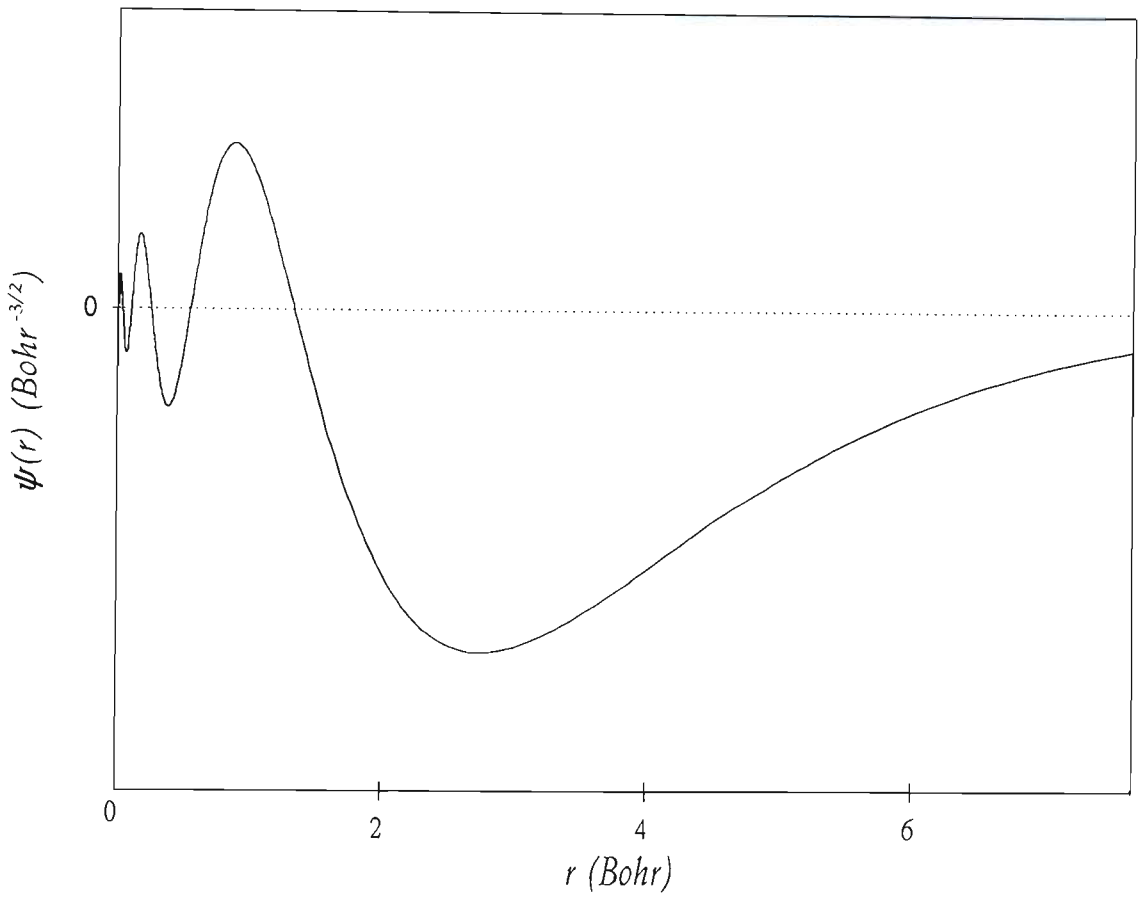

Figure 3.1 Valence wavefunction for Iridium 6s electrons

Since most physical properties of solids are largely dependent on the valence electrons, the core electrons may be considered to be inert. The pseudopotential approximation makes use of this fact by replacing the core electrons and the strong nuclear potential with a much weaker ionic pseudopotential. This pseudopotential is designed in such a way that it reproduces the effects of the core electrons on the valence wavefunctions. The pseudo wavefunctions corresponding to this pseudopotential oscillate less rapidly than the original wavefunctions. Consequently a greatly reduced number of plane waves is required for the expansion of the pseudo wavefunctions.

3.2 Historical account

In the late 1930's two methods were devised[29,30] in an attempt to overcome the demand for a large number of plane waves in the expansion of the electronic wavefunctions. Both of these methods involved a modification of the plane waves at small r.

3.2.1 Augmented plane waves

An *augmented plane wave* (APW)[31] is constructed such that it is identical to the original plane wave outside of a sphere of radius R (sometimes referred to as the APW sphere). Hence the APW $\phi_{\mathbf{k},,\varepsilon}$ can be defined as

$$\phi_{\boldsymbol{k},\varepsilon} = e^{i\boldsymbol{k}\cdot\boldsymbol{r}} \quad \text{for } r > R \quad . \tag{3.1}$$

Within the sphere of radius R, the potential $V(\boldsymbol{r})$ is assumed to have spherical symmetry so that an APW can be constructed in such a way as to satisfy the Schrödinger equation exactly within the sphere, and to join with the original plane wave on the surface of the sphere at radius R, (i.e. continuity of the wavefunction at $r=R$).

The portion of the APW outside of the sphere does not satisfy the Schrödinger equation. In addition, the two parts of the APW, namely that within and that outside of the sphere, do not join smoothly, (i.e. discontinuity of the gradient of the wavefunction at $r=R$).

An approximation to the correct solution to the crystal Schrödinger equation is obtained from a superposition of APW's. The expansion of $\psi_{\boldsymbol{k}}(\mathrm{r})$ will then have the form

$$\psi_k(r) = \sum_G c_G \phi_{k+G}(r) \quad , \tag{3.2}$$

with the sum over all reciprocal lattice vectors $\boldsymbol{G}$. A secular equation of about 20×20 is required for convergence of the energy eigenvalues.

3.2.2 Orthogonalised plane waves

An *orthogonalised plane wave* (OPW)[32] is constructed by adding to a plane wave contributions from core states of lower energy, so that the original wavefunction is resembled as closely as possible. Hence the OPW can be defined as:

$$\phi_k = e^{i\boldsymbol{k}\cdot r} + \sum_c b_c \psi_k^c(r) \quad , \tag{3.3}$$

with the sum over all core levels with wave vector $\boldsymbol{k}$. The constants b_c are determined through the requirement that ϕ_k be orthogonal to each core level:

$$b_c = -\int \psi_k^{c^*} \phi_k \, e^{i\boldsymbol{k}\cdot r} \, dr \quad . \tag{3.4}$$

This construction, based on lower energy core orbitals, ensures orthogonality of the OPW with the core states. The desired wavefunction can then be expressed as a series of OPWs. Only a few terms are required for a sufficiently good representation of the wavefunction which yields rapid convergence of the energy eigenvalues.

The OPW method yields energy values which are not as accurate as those from the APW method. This is due to the fairly approximate nature of the construction of the OPWs.

In order to eliminate the error due to this approximation one requires a secular equation of order $10^6 \times 10^6$.

For both the APW and OPW methods a suitable operator V^{Ps} can be generated, yielding a pseudo wave equation

$$(T + V^{Ps})\,\psi^{Ps} = E\,\psi^{Ps} \quad , \tag{3.5}$$

where ψ^{Ps} is the wavefunction generated in the described way (either APW or OPW). This equation is a mathematical transformation of the Schrödinger equation

$$(T + V)\,\psi^{AE} = E\,\psi^{AE} \quad , \tag{3.6}$$

where the eigenfunction is altered, but the energy eigenvalues remain the same. This operator, V^{Ps}, was the earliest form of the pseudopotential. It was not known as such for the first 20 years of its use, but when it was first expressed in the form shown in equation **(3.5)** in 1959 [33,34], a search for other forms for the pseudopotential began[29].

The earliest pseudopotentials which were constructed in the 1960's were empirically based. In other words, parameters for the construction of pseudopotentials were obtained by fitting pseudopotentials to experimental data, such as electronic band structures as measured by photoemission spectroscopy.

Modern pseudopotential generation procedures have moved beyond empirical fitting of potentials, to the development of *ab initio* methods in which the potentials are parameter-free. The general outline for the construction of such potentials is described in the following section.

3.3 Construction of norm-conserving non-local pseudopotentials

3.3.1 Requirements for pseudopotential construction

There are a number of requirements which should be met in the *ab initio* construction of a pseudopotential if one wishes it to most accurately represent the behaviour of the ion in various chemical environments:

1. The pseudopotential should be constructed in such a way that the pseudo wavefunction contains no radial nodes in the core region. This ensures a smooth shape for the pseudo wavefunction, which is essential if one wishes to represent the pseudo wavefunction with a sufficiently small plane wave basis set.

2. The pseudo wavefunction and the pseudopotential must identically match the original wavefunction and potential outside of a chosen cut-off radius r_c.

3. Pseudo-electron eigenvalues should be the same as the valence eigenvalues obtained from the atomic wavefunctions.

4. The core charge produced by the pseudo wavefunction must be the same as that produced by the atomic wavefunctions, a property that is known as *norm conservation*. The pseudopotential should hence satisfy

$$\int_0^{r_c} \psi^{AE\,*}(\boldsymbol{r})\ \psi^{AE}(\boldsymbol{r})\ d\boldsymbol{r} \;=\; \int_0^{r_c} \psi^{Ps\,*}(\boldsymbol{r})\ \psi^{Ps}(\boldsymbol{r})\ d\boldsymbol{r} \quad . \tag{3.7}$$

This condition ensures that the scattering properties of the pseudo wavefunction are identical to those of the ion and core electrons for the valence wavefunctions. It also guarantees accuracy of the exchange-correlation energy.

5. The first and second derivatives of the pseudo wavefunction should be matched to the real values at the cut-off radius r_c to ensure smoothness of the shape of the pseudo wavefunction.

To ensure an accurate description of scattering due to the ion in various atomic environments, we require a transferrable pseudopotential. A value for r_c close to the core radius increases the transferability of the potential. Also, subtracting the screening potential, namely the Coulomb and exchange-correlation contributions, from the pseudopotential yields the bare ion core potentials, which are transferrable to any atomic environment.

3.3.2 The general procedure for pseudopotential generation

The first step in generating a pseudopotential is to find the valence electron eigenvalues and wavefunctions for an all-electron atom with a chosen electronic configuration (generally the ground state configuration). Here a spherically symmetric form for the Hamiltonian is assumed, and a suitable choice is made for the form of the exchange-correlation functional. This choice of functional should be consistent throughout the generation procedure, and should be the same as that used in later calculations. The ionic pseudopotential is then generated iteratively using some procedure, such as the Troullier-Martins[35], or the Bachelet-Hamann-Schlüter[36] construction, so that the conditions listed in Section 3.3.1 are met. This ionic pseudopotential is then used to determine the electronic density in any new environment of the atom.

The value for r_c is chosen to range from one to two times the value of the radius of the outermost filled shell, and depends on the context in which the pseudopotential is to be used. For instance, a lower choice of value for r_c will ensure transferability of the pseudopotential to different chemical environments. A higher value for r_c , however, ensures a softer pseudopotential, in other words one which requires a smaller plane wave basis set for expansion of the pseudo wavefunctions. The choice of cut-off radius is refined after testing the pseudopotential for accuracy and transferability.

The flowchart in Figure 3.2 below outlines this procedure.

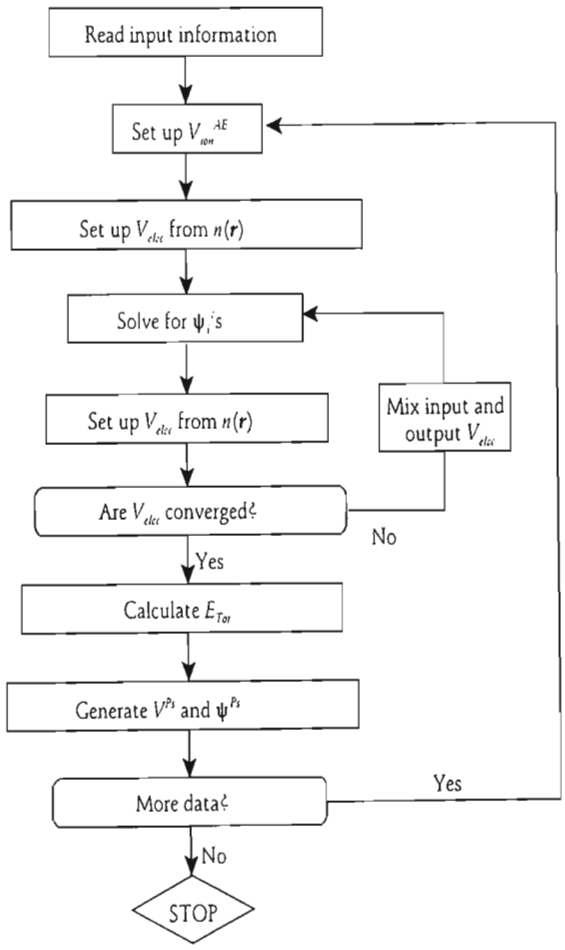

Figure 3.2 Flowchart describing pseudopotential generation procedure

3.3.3 The Martins-Troullier pseudopotential

It is desirable for the pseudopotential to be as "smooth" as possible. In other words we require a rapid convergence in the calculated total energy, and thus in the system's properties, with respect to an increase in the number of plane waves in the basis set. Smoothness can most easily be achieved by increasing the cut-off radius r_c. However, this process compromises the transferability of the pseudopotential, since there is a larger range in r for which the pseudopotential differs from the real potential. Troullier and Martins[35] developed the following procedure for generating smooth pseudopotentials:

An electronic wavefunction may be expressed in radial form in the following way:

$$\psi(\mathbf{r}) = \left(\frac{R_{nl}(r)}{r}\right) Y_{lm}(\hat{\mathbf{r}}) \quad , \tag{3.8}$$

where the Y_{lm} are the spherical harmonics. The radial Kohn-Sham equation becomes:

$$\left[-\frac{\hbar^2}{2m}\frac{d^2}{dr^2} + \frac{\hbar^2}{2m}\frac{l(l+1)}{r^2} + V(r) \right] r R_{nl}(r) = \varepsilon_{nl}\, r R_{nl}(r) \quad . \tag{3.9}$$

Here we are assuming a non-relativistic formulation of the theory, although in our actual calculations, a scalar-relativistic (that is, a first-order relativistic) version of the Dirac equation is used.

The radial pseudo wavefunction is defined in a similar way to that developed by Kerker[37]:

$$R_{nl}^{Ps}(r) = \begin{cases} R_{nl}^{AE}(r) & \text{if } r \geq r_c \quad , \\ r^{l+1} e^{p(r)} & \text{if } r \leq r_c \quad , \end{cases} \tag{3.10}$$

where $p(\boldsymbol{r})$ is a polynomial of order six in r^2:

$$p(r) = c_0 + c_2 r^2 + c_4 r^4 + c_6 r^6 + c_8 r^8 + c_{10} r^{10} + c_{12} r^{12} \quad . \tag{3.11}$$

To ensure norm conservation of the charge within the core radius, the following condition is applied:

$$2c_0 + ln\left[\int_0^{r_{cl}} r^{2(l+1)} e^{[2p(r) - 2c_0]} dr \right] = ln\left[\int_0^{r_{cl}} |R_{nl}^{AE}(r)|^2 r^2 dr \right] \quad . \tag{3.12}$$

This condition is used, together with the requirement that there be continuity of the pseudo wavefunction and its first four derivatives at r_c, and that there be zero curvature of the screened pseudopotential at the origin, to determine the coefficients in equation **(3.11)**. The expressions for these conditions are:

$$p(r_c) = ln\left[\frac{P(r_c)}{r_c^{l+1}} \right] \quad , \tag{3.13}$$

$$p'(r_c) = \frac{P'(r_c)}{P(r_c)} - \frac{l+1}{r_c} \quad , \tag{3.14}$$

$$p''(r_c) = 2V^{AE}(r_c) - 2\varepsilon_l - \frac{2(l+1)}{r_c} p'(r_c) - [p'(r_c)]^2 \quad , \tag{3.15}$$

$$p'''(r_c) = 2\left(V^{AE}\right)'(r_c) + \frac{2(l+1)}{r_c^2}p'(r_c) - \frac{2(l+1)}{r_c}p''(r_c) - 2p'(r_c)p''(r_c) \quad , \tag{3.16}$$

$$\begin{aligned} p''''(r_c) = {} & 2\left(V^{AE}\right)''(r_c) - \frac{4(l+1)}{r_c^3}p'(r_c) + \frac{4(l+1)}{r_c^2}p''(r_c) \\ & - \frac{2(l+1)}{r_c}p'''(r_c) - 2[p''(r_c)]^2 - 2p'(r_c)p'''(r_c) \quad . \end{aligned} \tag{3.17}$$

To ensure a smooth shape for the pseudopotentials, the condition that $V''(0)=0$ is imposed, bringing in an additional constraint:

$$c_2^2 + c_4(2l+5) = 0 \quad . \tag{3.18}$$

In these equations, $V^{AE}(\boldsymbol{r})$ is the all-electron atomic screened potential, and

$$P(r) = rR_{nl}^{AE}(r) \quad . \tag{3.19}$$

Once the c_i have been solved for, the screened pseudopotential is obtained by inverting the Schrödinger equation. The unscreened (bare ion) potentials are then obtained by subtracting contributions from both the Hartree and the exchange-correlation potentials:

$$V^{Ps}(\boldsymbol{r}) = V^{Ps}_{\text{screened}}(\boldsymbol{r}) - V_H[n_{ps}(\boldsymbol{r})] - V_{xc}[n_{ps}(\boldsymbol{r})] \quad . \tag{3.20}$$

3.3.4 The non-linear core correction

The assumption made in the generation of the pseudopotential is that the exchange-correlation functional is linear in terms of the core and valence electron densities:

$$E_{xc}(n_c + n_v) = E_{xc}(n_c) + E_{xc}(n_v) \quad . \tag{3.21}$$

In other words, it is assumed that the core and valence electron orbits do not overlap with one another. Where the exchange-correlation potential cannot be assumed to be linear in the charge density, an error will be incurred at the step where the screening potential, which is generated by the valence charge only, is removed.

This error can be corrected by means of the *non-linear core correction*, where the core electron density is added to the valence density at the unscreening step. In addition, this core density is carried into the solid state calculation, where it is added to the iteratively evolving valence electron density before the exchange-correlation potential and energy are calculated at each point $\boldsymbol{r}$ in space.

3.3.5 The Kleinman-Bylander construction

The general form for the pseudopotential is

$$V_{ion}^{Ps}(r) = \sum_{l} |Y_{lm}\rangle\, V_l^{Ps}(r)\, \langle Y_{lm}| \quad , \tag{3.22}$$

where the Y_{lm} are spherical harmonics, as before, and V_l is the lth angular momentum component of the pseudopotential acting on the wavefunction. Implementation of this

form for the pseudopotential requires a complete projection of the angular momentum components of the wavefunction. Kleinman and Bylander coined the term "semi-local" to describe the nature of this potential. They pointed out that separating this potential into local and non-local parts greatly reduces computational effort, as manipulation of these in reciprocal space is much more efficient.

This separation is done by assuming that all potentials with angular momentum l greater than some value l_{max} are equal to some arbitrarily chosen local potential. Hence

$$\begin{aligned} V^{Ps}(r) &= \sum_{l=0}^{l_{max}} |Y_{lm}\rangle V_l^{Ps}(r) \langle Y_{lm}| + \sum_{l=l_{max}+1}^{\infty} |Y_{lm}\rangle V_{loc}^{Ps}(r) \langle Y_{lm}| \\ &= \sum_{l=0}^{l_{max}} |Y_{lm}\rangle \left(V_l^{Ps}(r) - V_{loc}^{Ps}(r) \right) \langle Y_{lm}| + \sum_{l=0}^{\infty} |Y_{lm}\rangle V_{loc}^{Ps}(r) \langle Y_{lm}| \\ &= \sum_{l=0}^{l_{max}} |Y_{lm}\rangle \left(V_l^{Ps}(r) - V_{loc}^{Ps}(r) \right) \langle Y_{lm}| + V_{loc}^{Ps}(r) \quad . \end{aligned} \tag{3.23}$$

The Kleinman-Bylander separated form for the pseudopotential requires a single basis state for each of the angular momentum components of the wavefunction. This pseudopotential hence has the form:

$$V^{Ps}(r) = V_{loc}^{Ps}(r) + \sum_{l=0}^{l_{max}} \frac{|\psi^{Ps}{}_l \Delta V_l^{Ps}(r)\rangle \langle \Delta V_l^{Ps}(r) \psi^{Ps}{}_l|}{\langle \psi^{Ps}{}_l | \Delta V_l^{Ps}(r) | \psi^{Ps}{}_l \rangle} \quad , \tag{3.24}$$

where the local part of the pseudopotential is $V^{Ps}{}_{loc}(r)$, and $\Delta V^{Ps}{}_l(r)$ is the non-local part.

Use of this separable non-local potential will result in a substantial saving in computational time and storage. The process of taking matrix elements of the semi-local form for the pseudopotential on an N-dimensional plane wave basis set is an $O(N^2)$

process, whereas the separable form requires only O(N) operations. There is, however, a problem in the Kleinman-Bylander approach. The calculated chemical binding energy of molecules and solids is sometimes incorrectly described. In addition, self-consistent calculations can become unstable. This is because the Kleinman-Bylander Hamiltonian does not obey the Wronskian theorem, which states that atomic eigenfunctions are energetically ordered so that the energies increase with the number of nodes. In other words, the nodeless wavefunction is no longer guaranteed to be the solution with the lowest energy. Neglect of this theorem gives rise to "ghost states". These are single-node states below the zero-node reference state which do not appear in the all-electron case. Gonze *et al*[38] have proposed a rigorous means by which these ghost states may be identified. This problem can be addressed through slight modification of the pseudopotential, without altering its scattering properties. Careful choice of the local part of the pseudopotential will most likely eliminate these unwanted states.

3.3.6 Pseudopotentials for iridium

In the present work, the improved Troullier-Martins procedure was used, together with the Kleinman-Bylander construction, to generate pseudopotentials for iridium. The ground state valence electron configuration for iridium is [Xe] $4f^{14}$ $6s^2$ $6p^0$ $5d^7$. The 4f electrons, since they constitute a filled f-shell, are treated as belonging to the core. For each of the 6s, 6p and 5d valence orbitals the cut-off radius r_c was chosen to be a distance of 80% between the last node and the outermost extremum. Choice of these values for the core radii gave the most accurate values for the bulk properties when compared with experimental values. The consequent pseudo wavefunctions are shown, together with the all-electron wavefunctions, in Figures 3.3 to 3.5.

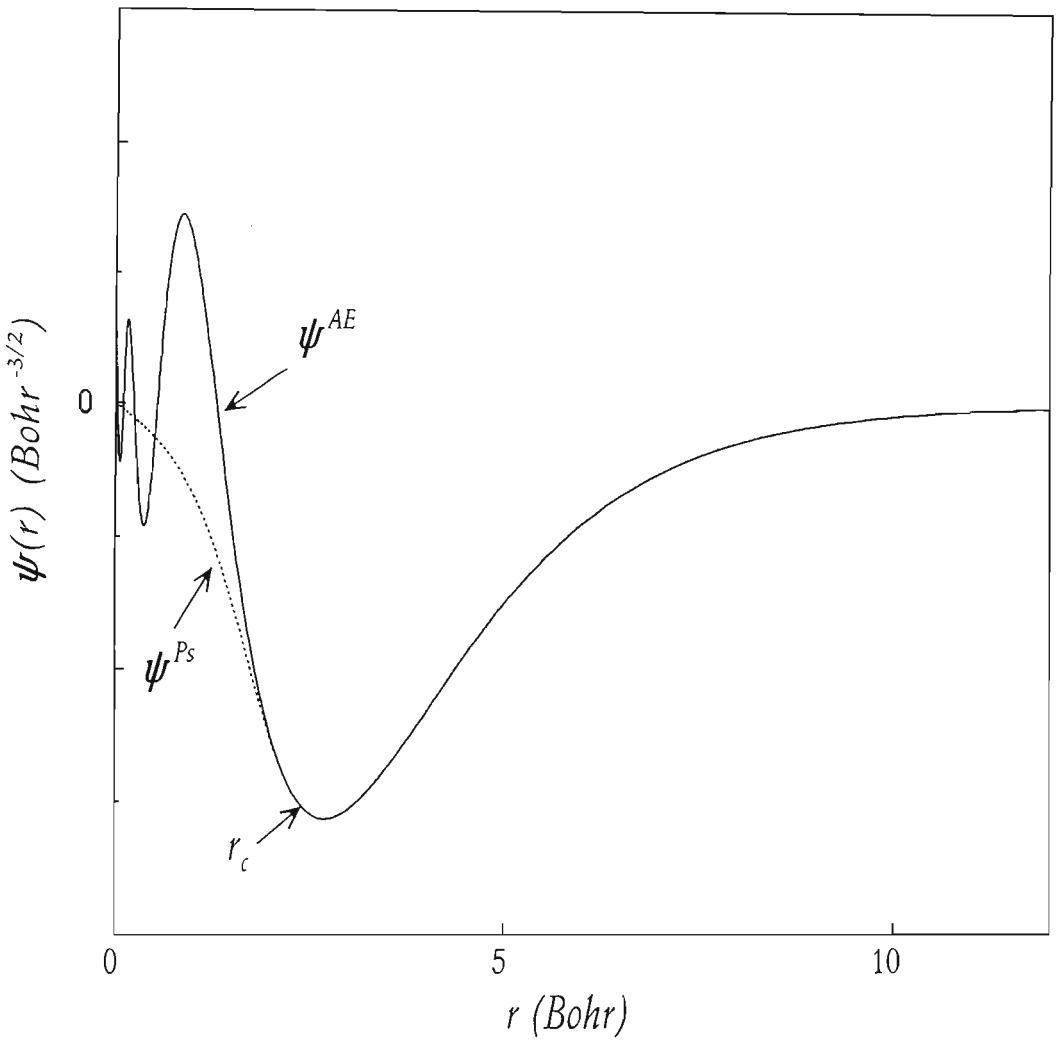

Figure 3.3 All-electron and pseudo wavefunctions for Iridium 6s valence electrons. (r_c = 2.41 Bohr)

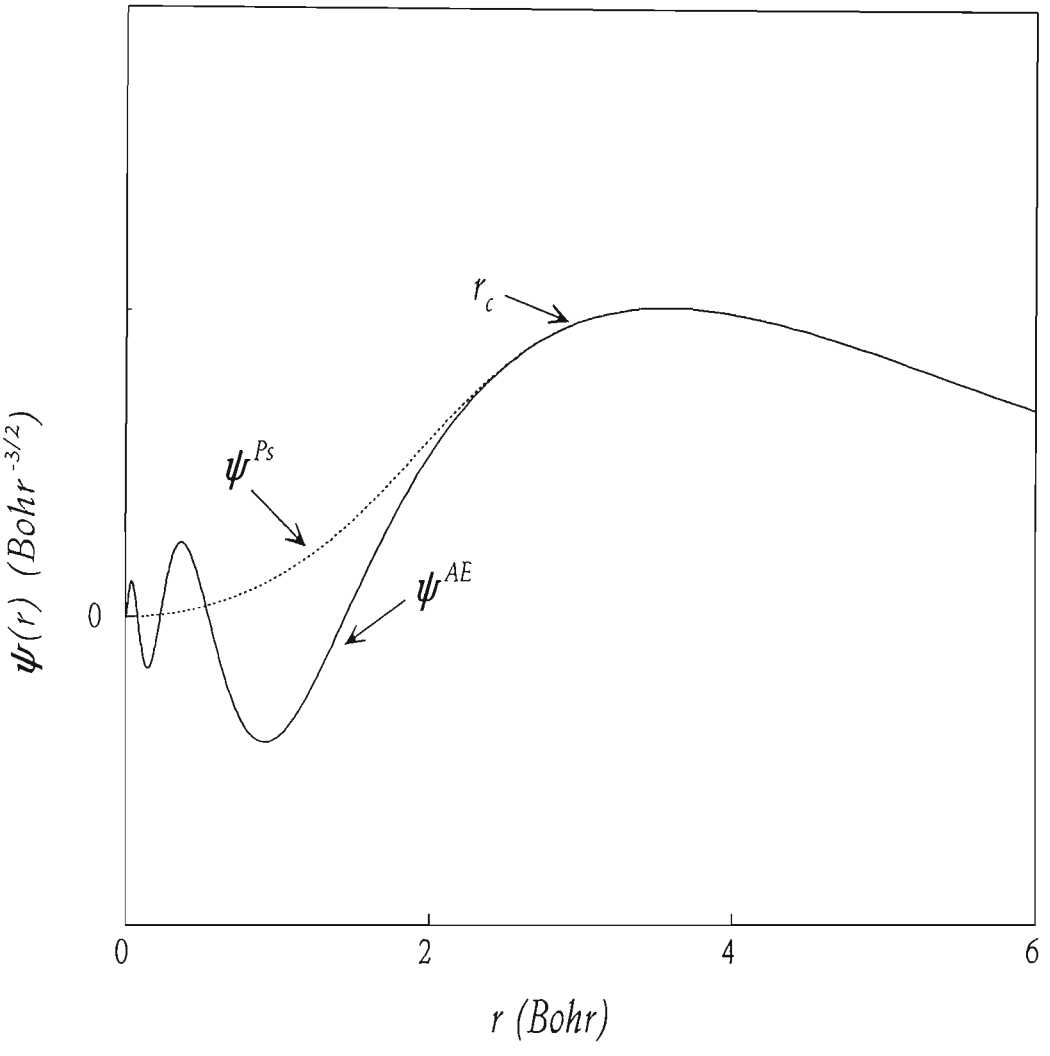

Figure 3.4 All-electron and pseudo wavefunctions for Iridium 6p valence electrons (r_c = 3.14 Bohr)

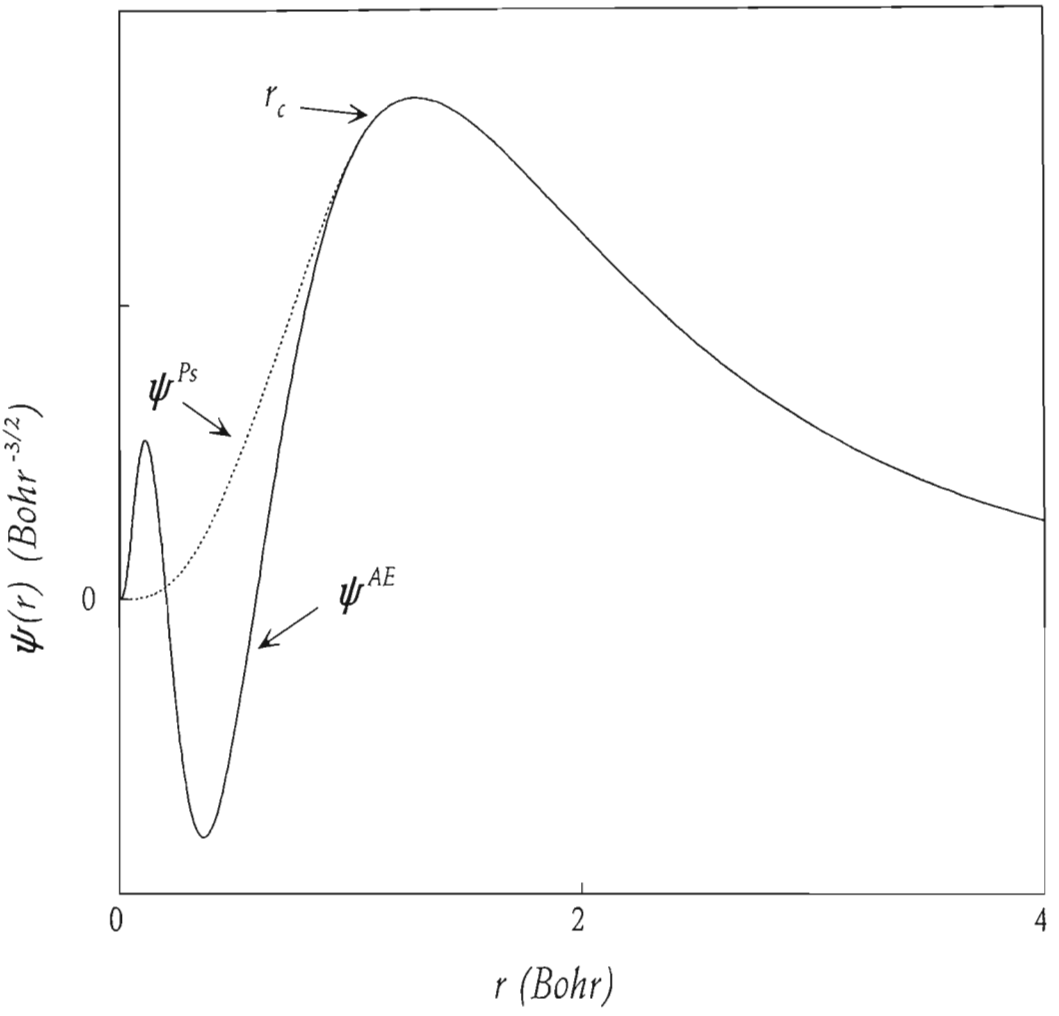

Figure 3.5 All-electron and pseudo wavefunctions for Iridium 5d valence electrons. (r_c = 1.15 Bohr)

The pseudopotentials for the valence states of iridium, together with the all-electron potential, are shown in Figure 3.6.

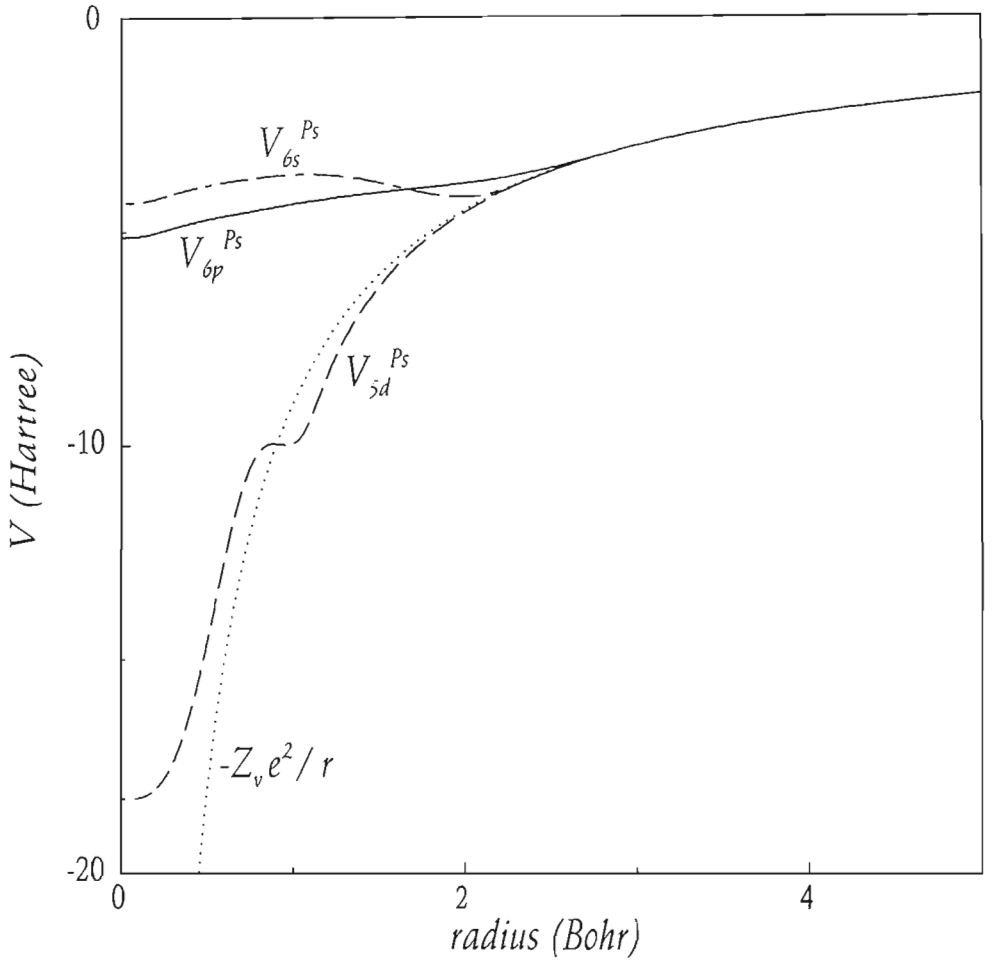

Figure 3.6 The 6s, 6p and 5d pseudopotentials for iridium shown together with the atomic all-electron potential.

The initial choice for the local part of the pseudopotential was $l=1$. This choice gave rise to ghost states in the system, and resulted in numerical instabilities in the self-consistency calculations. These states vanished with the choice of $l=0$ as the local part.

3.4 Constructing the total ionic potential

The total ionic potential is constructed by placing the pseudopotentials which have been generated for the single ions at the positions of each of the ions in the solid, for the various species of ion. Information of these ionic positions is obtained from the structure factor, which at wave-vector $\boldsymbol{G}$ is given by:

$$S_\alpha(\boldsymbol{G}) = \sum_I e^{i\boldsymbol{G}\cdot\boldsymbol{R}_I} \quad , \tag{3.25}$$

where I indicates the ions of species α in the unit cell. The local part of the total ionic potential is hence obtained by summation of the product of the Fourier transform of the pseudopotential and the structure factor over all species of ions in the system:

$$V_{ion}(\boldsymbol{G}) = \sum_\alpha S_\alpha(\boldsymbol{G})\, v_\alpha^{Ps}(\boldsymbol{G}) \quad . \tag{3.26}$$

As can be seen in Figure 3.6, the pseudopotential behaves in the same way as the Coulomb potential for large distances. In other words, it has the form $-Ze^2/r$ for large r, where Z is the valence of the atom. The Fourier transform of the pseudopotential therefore diverges as Z/G^2 for small G. The ionic potential hence becomes infinite at $\boldsymbol{G}=0$. This means that the electron-ion energy is infinite at $\boldsymbol{G}=0$. However, the electron-

electron interaction energies, as well as the ion-ion interaction energies, diverge similarly for $\boldsymbol{G}=0$. The contributions to the total energy by all three of these interactions cancel one another exactly.

However, since the pseudopotential is not purely Coulombic, it is not exactly proportional to Z/G^2 for small G, but has a constant contribution to the energy for each ionic species α:

$$V_{\alpha,core} = \int [\, Z/r - v_{\alpha}^{loc}(r)] 4\pi r^2 dr \quad . \tag{3.27}$$

Here v^{loc}_{α} is the local component of the pseudopotential. The integral given in equation **(3.27)** is non-zero within the core region, and zero otherwise, as the pure Coulomb potential and the pseudopotential are identical outside of this region, and hence their difference is zero.

The non-Coulomb part of the pseudopotential at $\boldsymbol{G}=0$ contributes to the total energy by an amount given by:

$$N_{el}\, \Omega^{-1} \sum_{\alpha} N_{\alpha}\, v_{\alpha,core} \quad . \tag{3.28}$$

Here N_{α} is the number of ions of species α, N_{el} is the number of electrons in the system, and Ω is the unit cell volume.

3.5 Advantages of the pseudopotential approach

Use of the pseudopotential approximation greatly reduces the number of plane waves which are required for expanding the electronic wavefunctions. The computational complexity of the calculation is therefore greatly reduced. Also, since the core electrons have been removed, fewer electronic wavefunctions are required in the system. The total energy of the valence system is typically one-thousand times smaller than that of the all-electron system. Therefore, since energy differences, rather than total energy values, are of primary importance, these may be obtained with greater accuracy within a pseudopotential calculation than in an all-electron calculation.

Chapter 4

Algorithms

4.1 Brillouin zone integrations

One can map out the first Brillouin zone in reciprocal space by a continuous set of $\boldsymbol{k}$-points:

$$\boldsymbol{k} = (k_x, k_y, k_z) \quad , \tag{4.1}$$

where the occupied states at each $\boldsymbol{k}$-point contribute to the electronic potential of the solid. There is an infinite number of $\boldsymbol{k}$-points in the Brillouin zone at which the wavefunctions are to be calculated. The required basis set would hence be infinite.

A consequence of Bloch's theorem is that the electronic structure problem of computing an infinite number of wavefunctions for an infinitely extended periodic system is reduced

to a problem of calculating a finite number of wavefunctions at this infinite number of $\boldsymbol{k}$-points within the Brillouin zone. Some form of integration over these $\boldsymbol{k}$-points is required. Many such methods have been developed over recent years. Some of these methods are briefly discussed below.

4.1.1 Brief overview of Brillouin zone integration methods

4.1.1.1 The Gaussian broadening method

This simple approach involves the even distribution of $\boldsymbol{k}$-points throughout the Brillouin zone. This method is primarily used when one requires only a rough idea of where the electronic states lie. It is less accurate than most other methods that are in use, but does converge relatively quickly[39].

4.1.1.2 The linear tetrahedron method

The linear tetrahedron method, developed by Lehmann and Taut[40], and later improved by Blöchl *et al*[41], is the standard method generally used when evaluating integrals over the Brillouin zone. This method consists of dividing the irreducible part of the Brillouin zone in reciprocal space into tetrahedra of equal volumes. Energy eigenvalues and matrix elements are evaluated at each apex. The values within the tetrahedra are found by linear interpolation and analytical integration.

Although this is the most simple and therefore attractive method for performing Brillouin zone integrations, Pickard and Payne[42] have reported problems with the linear tetrahedron method which are associated with band crossing and poor representations of van Hove

singularities. These problems arise due to the lack of second-order band information. In addition, a high density of $\boldsymbol{k}$-points is required for convergence.

4.1.1.3 The quadratic tetrahedron method

This method involves the piecewise quadratic representation of the Brillouin zone, and converges more rapidly than both the Gaussian and the linear tetrahedron method[43]. The van Hove singularities are treated more accurately than in either of these methods. However, due to the need for a high $\boldsymbol{k}$-point sampling density, this method has not been used very much.

4.1.1.4 The linear extrapolative method

Tetrahedra are once again made use of in this scheme, but in this case a single point within each tetrahedron is chosen, from which energies at unknown points in the Brillouin zone are extrapolated[44]. Convergence is achieved quickly with a relatively small set of tetrahedra.

4.1.1.5 The quadratic extrapolative method

This method, recently developed by Pickard and Payne[42], efficiently divides the Brillouin zone into subcells, making full use of the symmetry of the system. A single $\boldsymbol{k}$-point is selected within each cell, and the information regarding the wavefunctions and energy eigenvalues of neighbouring $\boldsymbol{k}$-points are found by means of extrapolation, using a second-order perturbation scheme, the so-celled $\boldsymbol{k}\cdot\boldsymbol{p}$ perturbation method. It has been shown to be highly efficient, requiring a low $\boldsymbol{k}$-point sampling density. However, this method is not highly suited to a plane-wave approach, as the perturbation scheme requires a perturbation sum over matrix elements between all of the states.

4.1.2 The special k-point technique

A method which is well suited to a plane-wave representation, and which is the method of choice in the current work, is the special $\boldsymbol{k}$-point technique. In this method, a discrete set of $\boldsymbol{k}$-points within the irreducible part of the Brillouin zone at which the electronic states are to be calculated are selected. The potential can therefore be calculated at a finite number of $\boldsymbol{k}$-points. Consequent errors may be rendered negligible by choice of a sufficiently dense set of $\boldsymbol{k}$-points.

The reciprocal space charge density for each $\boldsymbol{k}$-point in the set is given by

$$n_{\boldsymbol{k}}(\mathbf{r}) = \sum_i \psi_{\boldsymbol{k},i}^{*}(\mathbf{r})\ \psi_{\boldsymbol{k},i}(\mathbf{r}) \quad . \tag{4.2}$$

Here the i label indicates the occupied states, and $\boldsymbol{k}$ is an element of the Brillouin zone. The total charge density then becomes

$$n(\mathbf{r}) = \frac{V}{(2\pi)^3} \int_{BZ} n_{\boldsymbol{k}}(\mathbf{r})\, d\boldsymbol{k} \quad , \tag{4.3}$$

where V is the volume of the unit cell. As an approximation, the charge density is computed at a carefully selected set of $\boldsymbol{k}$-points. This set of $\boldsymbol{k}$-points should characterise the shape of the reciprocal space unit cell. Since the space group symmetry operations of a crystal map some of the $\boldsymbol{k}$-points onto others, the charge density at these points is related, and hence needs only one calculation for all such related points.

This fact is made use of by Monkhorst and Pack[45], who have designed a method for generating a special set of $\boldsymbol{k}$-points for the sampling of the Brillouin zone. This method is outlined in Appendix D on page 155.

4.2 Calculating the interaction energy between ions

Due to the long-range nature of the Coulomb interactions, the calculation of the Coulomb energy of the ionic system is difficult using real-space summation, due to the slow convergence of the series. The logarithmic divergence in real-space, together with that for the electron-electron interaction, is cancelled by the negative electron-ion divergence, yielding a finite contribution. A rapidly converging method, known as the Ewald summation[46], has been developed for performing these summations for periodic lattices. Ewald recast the slowly converging potential energy as the sum of two rapidly converging series plus a constant term:

$$E_{Ewald} = E_r + E_m + E_0 \quad , \tag{4.4}$$

where E_r is the real space sum:

$$E_r = \frac{1}{2} \sum_{I,J} \sum_{l} Z_I Z_J e^2 \frac{erfc(\eta |\boldsymbol{R}_1 + l - \boldsymbol{R}_2|)}{|\boldsymbol{R}_1 + l - \boldsymbol{R}_2|} \quad , \tag{4.5}$$

with l indicating the real space lattice vectors, and Z_I and Z_J the valences of ions I and J. The function *erfc* is the complementary error function. The l in the summation indicates that the $l=0$ term must be omitted when $I=J$. The Coulomb interaction here is between an ion positioned at $\mathbf{R}_2$ and an array of ions positioned at $\mathbf{R}_1+l$.

The term E_m indicates the reciprocal sum:

$$E_m = \frac{1}{2} \sum_{I,J} Z_I Z_J e^2 \left\{ \frac{4\pi}{\Omega} \sum_{G \neq 0} \frac{1}{|\boldsymbol{G}|^2} e^{-|\boldsymbol{G}|^2 / 4\eta^2} \cos\left[(\boldsymbol{R}_1 - \boldsymbol{R}_2) \cdot \boldsymbol{G}\right] \right\} \quad , \tag{4.6}$$

where the $\boldsymbol{G}$ are reciprocal-space lattice vectors, and Ω is the unit cell volume.

The constant term, E_0, is given by:

$$E_0 = \frac{1}{2}\sum_{I,J} Z_I Z_J e^2 \left\{ -\frac{2\eta}{\sqrt{n}}\delta_{IJ} - \frac{\pi}{\eta^2 \Omega} \right\} \quad . \tag{4.7}$$

Appropriate choice of a value for η will ensure rapid convergence of the real- and reciprocal-space summations. (It should be noted that

$$\frac{\partial E_{Ewald}}{\partial \eta} = 0 \tag{4.8}$$

for all values of η, as can be checked very easily. The actual value of η is hence chosen for computational efficiency. In our calculations, we choose a value of η that minimises E_0, and hence minimises E_r+E_m which is subject to errors due to the finite approximations to the summations.)

4.3 Overview of various electronic structure methods

4.3.1 Linear muffin tin orbital (LMTO) method

This method involves the construction of a sphere of radius S_{MT} around each atom. This is called the *muffin-tin sphere* (MT). The potential is hence divided into two separate regions:

$$V_{MT}(\boldsymbol{r}) = \begin{cases} V(r) & , r < S_{MT} \\ V_{MTZ} & , r \geq S_{MT} \end{cases} \quad . \tag{4.9}$$

The potential is spherically symmetric within the sphere, and constant, with a value of V_{MTZ} outside of the sphere. The basis functions can therefore be constructed as Bloch sums of *muffin-tin orbitals*:

$$\chi_{lm} = i^l Y_l^m(\mathbf{r}) \begin{cases} \psi_l(E,r) + P_l(E) \frac{(r/S_{MT})^l}{2(2l+1)} & , r < S_{MT} \\ (r/S_{MT})^{-l-1} & , r \geq S_{MT} \end{cases} . \qquad \textbf{(4.10)}$$

Here $\psi_l(E,r)$ is the solution of the radial Schrödinger equation inside the muffin-tin sphere as a function of energy E. The potential function $P_l(E)$ arises due to the requirement that the orbitals be differentiable and continuous at the sphere boundary. The kinetic energy, κ^2, of the part that is outside of the sphere is chosen to be zero. For this reason, the form for the orbital in this region is a very simple Neumann function.

In the *atomic sphere approximation* the muffin-tin spheres overlap in such a way that their total volume is the same as that for the unit cell. Inside each muffin-tin sphere the potential is assumed to be spherically symmetric. The wavefunction $\psi_l(E,r)$ is expanded around some energy E_v. This yields a set of linear muffin-tin orbitals. Use of this approximation leads to simplifications which allow large system sizes to be considered. These systems should, however, be fairly densely packed. Allowance is made for so-called "empty spheres" for less densely packed systems such as diamond.

The *full-potential method* (FP-LMTO) describes the potentials and charge densities in the crystal without necessarily regarding them as spherical. The unit cell is divided into non-overlapping muffin-tin spheres around the atom, and an interstitial region. Within the spheres the potentials and electron densities are expanded in a way that does not require spherical symmetry. In the interstitial region the charge density and the potential are expanded in a Fourier series, due to their periodic nature. Use of the full potential does

not require the system under consideration to be densely packed. Forces are more accurately calculated in this scheme.

4.3.2 Tight-binding method

In this method, the ground state total energy of the system, E_{Tot}, is approximated by the sum of two terms: the band-structure energy E_{BS}, and the repulsive potential U_{rep}. The band-structure energy E_{BS} is the sum of occupied electronic eigenvalues ε_n of the Hamiltonian. These eigenvalues may have a complex dependence on the atomic coordinates $\boldsymbol{R}_I$. In order to find the eigenvalues, the Hamiltonian should be constructed and diagonalised. Since the true eigenfunctions ψ_n of the Hamiltonian are unknown, they are approximated by a basis of known functions. This is done by means of a *linear combination of atomic orbitals* (LCAO):

$$| \psi_n \rangle = \sum_{I,\alpha} C_n^{I\alpha} | \phi_{I\alpha} \rangle \quad , \tag{4.11}$$

where the index I spans all of the atoms of the system, and the index α spans all of the basis orbitals positioned on a particular atom. These basis functions may be considered orthogonal to one other, in which case they would fall into the orthogonal tight-binding (OTB) category, or not, constituting the nonorthogonal tight-binding (NTB) category.

The repulsive potential U_{rep} consists of two terms: the repulsive energy between nuclear charges Z_I, and the term which corrects for the double counting of the electron-electron energy in the band-structure term E_{BS}. It is assumed that the repulsive potential has a simple dependence on the atomic geometry, and can hence be represented as a sum of short-ranged two-body potentials, each of which depend purely on the distance between

the associated atomic pairs. This gives rise to a semi-empirically based tight-binding scheme. The atomic forces are calculated by means of the Hellmann-Feynman theorem.

Earlier tight-binding methods were used successfully in applications with semiconductors and transition metals, but were generally shown to be less accurate than self-consistent methods[47]. More recent developments to this method have, however, yielded more accurate results[48].

4.3.3 Full potential linearised augmented plane wave method

Otherwise known as the FLAPW method, this all-electron method treats the electrons in a scalar-relativistic form. All of the electrons are included in a self-consistent approach, using a full potential for the valence electrons which has no shape approximation. The method makes use of the periodicity of the system, and operates within the local density approximation for the exchange-correlation energy. The basis set is made up of linearised augmented plane waves (LAPW's), which are modified from the augmented plane waves discussed in Section 3.2.1. The LAPW's are constructed in such a way that the basis functions as well as their derivatives are continuous at the boundary edge of the APW sphere. This ensures greater flexibility of the LAPW basis, enabling the potential generated in this way to be used as a general crystal potential.

Although this method is efficient and accurate for densely packed systems[49], it is computationally demanding for fairly open structures. It is therefore most appropriate for precise calculations that do not involve dynamical processes or large supercell geometries.

4.4 The iterative method

4.4.1 General procedure

The general procedure which is followed for a solution of the Kohn-Sham equations is outlined below:

- An estimate is made for the initial charge density $n(\boldsymbol{r})$.
- From this value for $n(\boldsymbol{r})$ the Hartree potential $V_H(\boldsymbol{r})$ and the exchange correlation potential $V_{xc}(\boldsymbol{r})$ are calculated.
- A choice of basis functions is made, eg. plane waves.
- The Hamiltonian matrix is constructed for each $\boldsymbol{k}$-point which is an element of the Brillouin zone.
- The Hamiltonian matrix is then diagonalised, which yields the Kohn-Sham eigenvectors and eigenvalues. This step may be performed "conventionally" or "iteratively".
- The Fermi level is found through fractional occupation of the states by means of the Fermi distribution function.
- The charge density is computed, and mixed with the input density.
- A new Hamiltonian is constructed.

This process is repeated until self-consistency is reached.

In the Fermi distribution function

$$f_{\boldsymbol{k}n} = \left[\exp\left\{ \frac{(\varepsilon_{\boldsymbol{k}n} - \varepsilon_f)}{k_B T} \right\} + 1 \right]^{-1} , \qquad \textbf{(4.12)}$$

the Fermi level ε_f is adjusted to accommodate the fixed number of electrons. Although the temperature of the electronic sub-system is 0, a choice of T close to room temperature is made for computational convenience. (This removes the discontinuity in the Fermi distribution function). This assumption is of no consequence, since $k_B T \ll \varepsilon_f$.

Conventional matrix diagonalisation techniques are not well suited to the solution of plane-wave pseudopotential calculations, as the number of operations required for matrix diagonalisation is proportional to N_{pw}^3, where N_{pw} refers to the number of plane wave basis states, which are typically of the order of 100 for each atom in a system. (The efficiency of one such matrix diagonalisation technique is discussed in Appendix E.) In addition, conventional diagonalisation methods require storage of the entire Hamiltonian, which is of the order of N_{pw}^2. Alternative methods, which scale more favourably with the size of the system and require less memory storage space, are thus required.

4.4.2 The Car-Parrinello method

One such method is the Car-Parrinello method[9], for which a Lagrangian is formulated for the Kohn-Sham eigenstates. Here the electronic wavefunctions are treated as dynamical variables.

The form for this Lagrangian is:

$$L = \mu \sum_i \langle \psi_i | \psi_i \rangle - E[n(\boldsymbol{r})] \quad , \tag{4.13}$$

where μ is a fictitious mass associated with the wavefunctions, and $E[n(\boldsymbol{r})]$ is the Kohn-Sham energy surface. This Lagrangian describes the fictitious dynamics of trial wavefunctions, which are successively updated until they eventually converge to the true Kohn-Sham eigenstates. To ensure that not all of these eigenfunctions converge to the lowest energy eigenstate, a condition of mutual orthogonality must be imposed on them:

$$\langle \psi_i | \psi_j \rangle = \delta_{i,j} \quad . \tag{4.14}$$

In the Lagrangian molecular dynamics approach, these orthogonality constraints are taken into account by means of the method of Lagrange multipliers. The Lagrangian then takes the form:

$$L = \mu \sum_i \langle \psi_i | \psi_i \rangle - E[n(\boldsymbol{r})] + \sum_{i,j} \Lambda_{ij} \left[\left\{ \int \psi_i^*(\boldsymbol{r}) \psi_j(\boldsymbol{r}) d^3(\boldsymbol{r}) \right\} - \delta_{ij} \right] \quad , \tag{4.15}$$

where the Lagrange multipliers Λ_{ij} ensure the orthonormality of the wavefunctions.

Using the Euler-Lagrange equations:

$$\frac{d}{dt} \left(\frac{\delta L}{\delta \dot{\psi}_i^*} \right) = \frac{\delta L}{\delta \psi_i^*} \quad , \tag{4.16}$$

we obtain the following equations of motion for the eigenstates:

$$\mu \ddot{\psi}_i = -H\psi_i + \sum_j \Lambda_{ij}\psi_j \quad , \tag{4.17}$$

where H is the Kohn-Sham Hamiltonian. The term ($-H\psi_i$) acts as a force which propagates the electronic wavefunctions along their molecular-dynamics trajectories.

However, the evolution of these equations of motion requires the values of the Lagrange multipliers to vary continuously with time. They would hence need to be evaluated at infinitely small time intervals.

To avoid this problem, the Lagrange multipliers are approximated by a constant value during each time step. This means that the wavefunctions will not remain orthonormal at the end of the iterative step, and a separate orthonormalisation step is required for each iteration. As a first approximation, we neglect all Lagrange multipliers Λ_{ij} except for Λ_{ii} which is assumed to be constant. The equation of motion hence takes the form:

$$\mu \ddot{\psi}_i = -[H - \lambda_i]\psi_i \quad , \tag{4.18}$$

where λ_i is the approximation for the Lagrange multiplier Λ_{ii}, and is found by computing the expectation value of the energies of the states:

$$\lambda_i = \langle \psi_i | H | \psi_i \rangle \quad . \tag{4.19}$$

The integration of the equations of motion is done by means of the Verlet algorithm. The value of the ith electronic state at the time step $(t+1)$ is given by:

$$\psi_i(t+1) = 2\psi_i(t) - \psi_i(t-1) + \Delta t^2 \ddot{\psi}_i(t) \quad . \tag{4.20}$$

Substituting equation **(4.18)** into this yields

$$\psi_i(t+1) = 2\psi_i(t) - \psi_i(t-1) - \frac{\Delta t^2}{\mu}[H - \lambda_i]\psi_i(t) \quad . \tag{4.21}$$

In the Car-Parrinello formulation, once a time step in the integration of the equations of motion has been completed, orthogonalisation of the wavefunctions is done iteratively, with repeated application of the following algorithm:

$$\psi_i' = \psi_i - \frac{1}{2}\sum_{j \neq i} \langle \psi_j | \psi_i \rangle \psi_j \quad , \tag{4.22}$$

which generates a new set of wavefunctions $\{\psi_i'\}$ from a set of normalised wavefunctions $\{\psi_i\}$. The wavefunctions are then to be normalised after each iteration of the algorithm. The number of steps required in this algorithm increases with the number of wavefunctions, and the extent of the non-orthonormality of these functions.

If the wavefunctions are not orthogonalised, they all cascade down to the lowest energy eigenfunction. The orthogonalisation procedure ensures that the eigenfunctions ultimately converge to a set of mutually orthogonal states that span the ground state. One of the downfalls of the Car-Parrinello method is that the true energy eigenstates are not computed. This method is therefore applicable to band-gap materials (which have a constant occupation number for each state), and not for metals.

4.4.3 The conjugate gradients method

The conjugate gradients method[50] is an effective and straight-forward method for finding the minimum of a function, with a fairly rapid rate of convergence[51]. The initial direction in which to move in order to locate the minimum of a function $f(\boldsymbol{x})$ from the starting point $\boldsymbol{x}$ is in the direction of steepest descent of that function, $\nabla f(\boldsymbol{x})$. Subsequent directions are taken to be a linear combination of previous directions and the new gradient. The procedure is outlined below:

The gradient $\boldsymbol{g}_0$ of the function $f(\boldsymbol{x})$ at the starting point $\boldsymbol{x}_0$ is given by:

$$\boldsymbol{g}_0 = \left.\frac{\delta f(\boldsymbol{x})}{\delta \boldsymbol{x}}\right|_{\boldsymbol{x}=\boldsymbol{x}_0} . \tag{4.23}$$

The initial minimisation step is hence given by:

$$\boldsymbol{d}_0 = -\left.\frac{\delta f(\boldsymbol{x})}{\delta \boldsymbol{x}}\right|_{\boldsymbol{x}=\boldsymbol{x}_0} = -\boldsymbol{g}_0 . \tag{4.24}$$

The subsequent mutually conjugate directions are chosen so that

$$\boldsymbol{d}_{k+1} = -\boldsymbol{g}_{k+1} + \beta_k \boldsymbol{d}_k \quad , \quad k=0,1,\ldots . \tag{4.25}$$

The coefficients β_k may be given by, for example, the Fletcher-Reeves formula:

$$\beta_k = \frac{\boldsymbol{g}_{k+1}^{\mathrm{T}} \cdot \boldsymbol{g}_{k+1}}{\boldsymbol{g}_k^{\mathrm{T}} \cdot \boldsymbol{g}_k} , \tag{4.26}$$

where $\boldsymbol{g}^{\mathrm{T}}_k$ is the transpose of the gradient vector $\boldsymbol{g}_k$.

The step length along each direction is calculated by:

$$\lambda_k = \frac{\boldsymbol{d}_k^T \cdot \boldsymbol{g}_k}{\boldsymbol{d}_k^T \cdot (\boldsymbol{Q} \cdot \boldsymbol{d}_k)} \quad , \tag{4.27}$$

where $\boldsymbol{Q}$ is a positive definite symmetric matrix, and $\boldsymbol{d}^T_k$ is the transpose of the direction vector $\boldsymbol{d}_k$.

For an n-dimensional subspace, the minimum of the function $f(\boldsymbol{x})$ may be located in n steps or less using the conjugate gradients method. This is because $\boldsymbol{g}_k$ is constructed in such a way as to be perpendicular to all previous search directions, so that each point $\boldsymbol{x}_{k+1}$ is a minimum with respect to the entire subspace that is spanned by the vectors $\{\boldsymbol{d}_0, \boldsymbol{d}_1, \ldots \boldsymbol{d}_k\}$. In other words, each step may be considered as removing one dimension of the space from the problem.

When applying the conjugate gradients method to total energy calculations, one replaces the function f in the above procedure with the Kohn-Sham energy functional E. The wavefunctions $\{\psi_i\}$ take the place of the vector $\boldsymbol{x}$, and the Kohn-Sham Hamiltonian H replaces the matrix $\boldsymbol{Q}$.

4.4.4 The preconditioned steepest descent method

The iterative scheme which is used in the BEST code is a variant of the preconditioned steepest descent algorithm (PSD)[6]. In this algorithm it is not necessary for the entire Hamiltonian to be stored in memory, as is done in the Car-Parrinello scheme. Instead, a subspace of occupied states is selected, since only the lowest occupied states of the system are of interest. This yields the lowest-energy eigenstates of the system. The number of

selected states in this procedure, n_s, is larger than the number of occupied states, and is typically of the order of 1% of the total number of plane waves (which determines the size of the Hamiltonian). Where the conjugate gradients method requires storage of all past information for the respective search directions which requires a large amount of storage space, the steepest descent method requires storage of only the information pertaining to the current search direction. Hence, although this method is generally less efficient in finding the minimum of the function $f(\boldsymbol{x})$, it requires less storage space, making it more practical for calculations of complex systems. A further point in favour of the PSD method is that the conjugate gradients method, in using information from previous iterations, may force the states in the wrong direction. This is because the space which is spanned by the trial states is altered between steps due to the orthogonalisation procedure, as well as the implementation of the equation of motion. Hence, the information pertaining to previous steps is given in reference to a rotated space. If this rotation is large, it will lead to errors in the propagation of the states. By contrast, the PSD method, in only using information from the current iteration, will not incur this problem. Chetty *et al*[6] pointed out that the PSD method, combined with the subspace diagonalisation, does not suffer from the well-documented "long valley" problem faced by the general steepest descent algorithm, and is a stable and efficient method for finding converged minimum energy results.

4.4.4.1 The steepest descent algorithm

In order to minimise the energy, this algorithm considers a step in the direction of steepest descent of the energy:

$$\boldsymbol{d}_i = -\frac{\delta f(\boldsymbol{x})}{\delta \boldsymbol{x}}\bigg|_{\boldsymbol{x}=\boldsymbol{x}_i} . \qquad (4.28)$$

The minimum along a certain direction is located when the direction along which one is searching becomes perpendicular to the gradient. Consecutive search directions are hence always perpendicular to one another in this method, in contrast with the conjugate gradients method, in which the current search direction is perpendicular to all previous directions. The iterative procedure for this method is:

$$\boldsymbol{x}_{k+1} = \boldsymbol{x}_k - \lambda_k \nabla f(\boldsymbol{x}_k) = \boldsymbol{x}_k - \lambda_k \boldsymbol{g}_k \quad , \tag{4.29}$$

where $\boldsymbol{g}_k$ is the gradient of the function $f(\boldsymbol{x})$ at the point $\boldsymbol{x}_k$. There are various ways of choosing the value of the step λ_k. Some examples of these methods are the linear search method, the optimal gradient method, and the preconditioned steepest descent method, which will be looked at in more detail shortly.

Within total energy calculations, the equation of motion of the wavefunctions in the steepest descent method becomes:

$$\frac{\partial}{\partial t} | \psi_i \rangle = - (H - \lambda_i) | \psi_i \rangle \quad . \tag{4.30}$$

The stationary solution of equation **(4.30)** yields the eigenstates of the Hamiltonian. The expectation value for the energy in state $|\psi_i\rangle$ is given by:

$$\lambda_i = \frac{\langle \psi_i | H | \psi_i \rangle}{\langle \psi_i | \psi_i \rangle} \quad . \tag{4.31}$$

A finite difference approximation for equation **(4.30)** is used for small times Δt for the propagation of the states:

$$|\psi_i^{t+1}\rangle = |\psi_i^{t}\rangle + \Delta t\,(\lambda_i^{t} - H)\,|\psi_i^{t}\rangle \quad , \tag{4.32}$$

these steps being repeated until the states become stationary.

4.4.4.2 Preconditioning

In the PSD algorithm, the magnitude of the step in the direction of steepest descent is inversely proportional to the kinetic energy of the state. With the wavefunctions expressed as a plane wave basis set expansion:

$$\psi_i(\boldsymbol{r}) = \sum_{\boldsymbol{G}} c_{i,\boldsymbol{k}+\boldsymbol{G}}\; e^{i(\boldsymbol{k}+\boldsymbol{G})\cdot\boldsymbol{r}} \quad , \tag{4.33}$$

the Hamiltonian matrix has the form:

$$\begin{aligned} H_{\boldsymbol{k}+\boldsymbol{G},\boldsymbol{k}+\boldsymbol{G}'} = \frac{\hbar^2}{2m}|\boldsymbol{k}+\boldsymbol{G}|^2\,\delta_{\boldsymbol{G}\boldsymbol{G}'} + V_H(\boldsymbol{G}-\boldsymbol{G}') + V_{xc}(\boldsymbol{G}-\boldsymbol{G}') \\ + V_{loc}^{Ps}(\boldsymbol{G}-\boldsymbol{G}') + V_{NL}^{Ps}(\boldsymbol{k}+\boldsymbol{G},\boldsymbol{k}+\boldsymbol{G}') \quad . \end{aligned} \tag{4.34}$$

Equation **(4.32)** then becomes:

$$c_{i,\boldsymbol{k}+\boldsymbol{G}}^{t+1} = c_{i,\boldsymbol{k}+\boldsymbol{G}}^{t} + \Delta t \sum_{\boldsymbol{G}'} (\lambda_{i,\boldsymbol{k}+\boldsymbol{G}}\,\delta_{\boldsymbol{G}\boldsymbol{G}'} - H_{\boldsymbol{G}\boldsymbol{G}'})\,c_{i,\boldsymbol{k}+\boldsymbol{G}}^{t} \quad . \tag{4.35}$$

Due to the increasingly dominant role played by the kinetic energy for the high-energy components, a preconditioning matrix is used to scale these high-energy components,

allowing a variable time step for each Fourier component of the wavefunction. The preconditioning matrix may assume the form of:

$$B_{gg'} = \left\{ \tfrac{1}{2}|\mathbf{G}|^2 + S \right\}^{-1} \delta_{gg'} \quad , \tag{4.36}$$

where S is a constant shift, whose value is chosen appropriately. Equation **(4.35)** can therefore be written in the form:

$$C^{t+1}_{\mathbf{G},n} = C^{t}_{\mathbf{G},n} + \frac{\sum_{g'} (\lambda_{kn} - H_{\mathbf{G},\mathbf{G}'}) C^{t}_{\mathbf{G},n}}{\tfrac{1}{2}|\mathbf{G}|^2 + S} \quad . \tag{4.37}$$

The effect of the preconditioning matrix is to transform the Kohn-Sham Hamiltonian H into a matrix which is diagonally dominant, requiring a smaller spectrum of eigenvalues than in the original H. This causes the minimisation problem to converge more rapidly than in the unpreconditioned case. As in the Car-Parrinello scheme, the wavefunctions are required to be orthogonalised after each propagation step.

4.4.5 The Gram-Schmidt orthogonalisation scheme

The Gram-Schmidt scheme is one of the schemes which may be used for orthogonalising the wavefunctions at the end of each iteration in the propagation of the wavefunctions. In this scheme the orthogonalisation is done in a particular order. Each higher-energy wavefunction is forced to be orthogonal to the wavefunctions which have lower energy. Each state is hence converged to its lowest energy state subject to the condition of it being orthogonal to all states below it in energy. The set of lowest energy levels under these constraints are the Kohn-Sham eigenstates.

The Gram-Schmidt scheme comprises the following algorithm:

$$\psi_i'' = \psi_i - \sum_{j<i} \langle \psi_j' | \psi_i \rangle \, \psi_j' \quad , \tag{4.38}$$

where

$$\psi_i' = \frac{\psi_i''}{|\psi_i''|} \quad , \tag{4.39}$$

yielding a set of orthonormal wavefunctions $\{\psi_i'\}$ from a set of linearly independent wavefunctions $\{\psi_i\}$.

4.4.6 The subspace diagonalisation scheme

The subspace diagonalisation scheme, developed by Chetty *et al*[6], is an alternative orthogonalisation method to the Gram-Schmidt scheme. In this scheme, once the set of trial wavefunctions have been propagated according to equation **(4.37)**, these nonorthogonal trial states are diagonalised with respect to the Hamiltonian

$$\sum_{m=1}^{n_s} \langle \psi_{kn} | H | \psi_{km} \rangle \, D_{kmn} = \varepsilon_{kn} \sum_{m=1}^{n_s} \langle \psi_{kn} | \psi_{km} \rangle \quad . \tag{4.40}$$

The exact eigenfunctions, with eigenvalues ε_{kn}, are determined from the coefficients D_{kmn}, for the subspace spanned by the states $|\psi_{kn}\rangle$:

$$|\psi_{kn}\rangle = \sum_{m=1}^{n_s} D_{kmn} |\psi_{km}\rangle \quad . \tag{4.41}$$

This subspace diagonalisation serves to orthogonalise the states, and to determine the next approximation for the Kohn-Sham eigenvalues. It is the only iterative diagonalisation method that ensures that the system converges to the actual eigenstates of the ground state, and not a linear combination of these (which is what equations **(4.38)** and **(4.22)** effectively do).

4.5 Atomic relaxations

We have not as yet considered the atoms in any coordination other than in fixed positions. A consequence of the Car-Parrinello method is that electronic and atomic relaxations can take place simultaneously. In order to do this we need to compute the forces acting on the atoms in order to be able to update the atomic positions. These forces are found by means of the Hellmann-Feynman theorem[52,53].

4.5.1 The Hellmann-Feynman theorem

This theorem states that when the wavefunctions ψ_i are eigenstates of the Hamiltonian H, then

$$\frac{\partial}{\partial \boldsymbol{R}_I} \langle \psi_i | H | \psi_i \rangle = \langle \psi_i | \frac{\partial H}{\partial \boldsymbol{R}_I} | \psi_i \rangle \quad , \tag{4.42}$$

for the positions of the atoms $\boldsymbol{R}_I$. Hence, since the force on the atoms is given by

$$\boldsymbol{F}_I = -\frac{\partial E_{Tot}}{\partial \boldsymbol{R}_I} = -\left\{ \frac{\partial}{\partial \boldsymbol{R}_I} \langle \psi_i | H | \psi_i \rangle + \frac{\partial E_{ion}}{\partial \boldsymbol{R}_I} \right\} , \qquad \textbf{(4.43)}$$

this force can be efficiently calculated in the following way:

$$\boldsymbol{F}_I = -\left\{ \langle \psi_i | \frac{\partial H}{\partial \boldsymbol{R}_I} | \psi_i \rangle + \frac{\partial E_{ion}}{\partial \boldsymbol{R}_I} \right\} . \qquad \textbf{(4.44)}$$

In other words, when each ψ_i is an eigenstate of H, the partial derivative of the Kohn-Sham energy with respect to the atomic positions yields the force on the atoms. However, to avoid incurring errors which arise from using unconverged wavefunctions, the Hellmann-Feynman theorem should only be implemented once the wavefunctions are close to self-consistency, since the force (unlike the energy) is not a variational quantity.

An additional term which should arise in equation **(4.43)**is the partial derivative of the basis set with respect to the atomic positions. This contribution to the force is called the *Pulay* force. However, with the use of a plane-wave basis, this derivative becomes zero, and the Pulay force vanishes. This is one of the advantages of using a plane-wave basis (which goes hand-in-hand with the pseudopotential method), as compared with the numerous other localized basis set methods.

4.5.2 The BFGS algorithm

Once the Hellmann-Feynman forces have been computed, the atoms are moved in the direction of these forces by an amount determined through application of a modified Broyden-Fletcher-Goldfarb-Shanno (BFGS) update scheme[54]. The basic idea behind the BFGS method is that the energy surface around a minimum is quadratic in small displacements, and hence may be totally determined by a Hessian matrix, which is the matrix of second derivatives of the energy. If this matrix was known, one could move from any point to the minimum in one step. However, this matrix is not known, and hence an approximation to it is built up by progressive improvement of a trial matrix as the atoms are moved using the BFGS algorithm. (This is also known as a *quasi-Newton* or *variable metric* method.)

The atomic positions are updated according to the relation:

$$\boldsymbol{R}_{i+1} = \boldsymbol{R}_i + \lambda \Delta \boldsymbol{R}_i \quad , \tag{4.45}$$

where

$$\Delta \boldsymbol{R}_i = \boldsymbol{H}_i \boldsymbol{F}_i \quad . \tag{4.46}$$

Here $\boldsymbol{H}_i$ is the Hessian matrix, and $\boldsymbol{F}_i$ indicates the forces on the atoms. A modification to this method is made by applying the Oren-Spedicato scaling[55] in the second step in order for the process to be self-scaling. In the BEST implementation it is assumed that the forces experienced by each atom are comparable to the forces due to phonon vibrations. The distance in which the atoms are moved along the direction of the force is hence related to the force, the mass, and a characteristic phonon frequency. Here the Debye temperature is used. This leads to a rapidly convergent minimisation of the total energy with respect to atomic positions. No more than 5 atomic steps should be required for full convergence of the forces to be attained, to within 10^{-4} Hartree/Bohr.

4.5.3 Computational implementation

The computational procedure for relaxation of the atoms has the following sequence:

- The initial wavefunctions are generated randomly, and the charge density is calculated from these.

- The Kohn-Sham Hamiltonian is then constructed, from which the total energy is calculated.

- This energy is reduced to self-consistency by the method of preconditioned steepest descents.

- Once a self-consistent result for the energy is obtained for this set of atomic positions, the forces on the atoms are computed.

- The atoms are moved in the direction of these forces by integration of the equations of motion using the BFGS method.

- The wavefunctions from the previous atomic iteration will no longer be eigenstates for the new structure of the atoms, but are a good starting point for the new self-consistency procedure. The entire procedure is therefore repeated for this new set of atomic positions, until the atomic forces are sufficiently small.

- Once convergence in the forces is reached, the atoms will have completely relaxed into their lowest-energy positions, and the total energy will be the correct ground state energy for this atomic structure.

This computational procedure is outlined in the flow diagram shown in Figure 4.1 below.

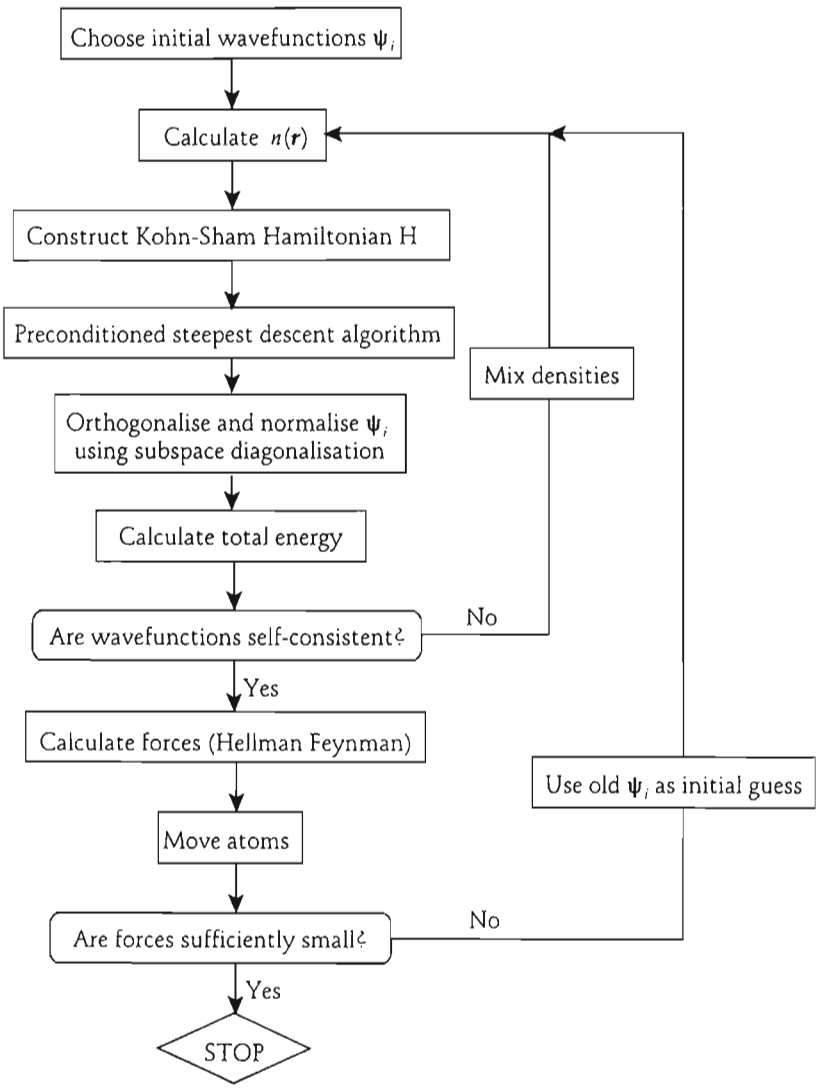

Figure 4.1 Flow diagram illustrating procedure for iterative minimum energy calculation including atomic relaxations

4.6 Additional computational considerations

4.6.1 Fast Fourier transforms

Since the charge density is given by the square of the magnitude of the wavefunction,

$$n(\boldsymbol{r}) = \sum_{i=1}^{N} |\psi_i(\boldsymbol{r})|^2 \quad , \tag{4.47}$$

it is most efficiently computed in real space. The charge density is also needed in real space in order to compute the exchange-correlation energy and potential (on a point-by-point basis in real space). This requires the wavefunctions to be Fourier transformed into real space, from their reciprocal space representation. This is done in the BEST codes by means of fast Fourier transformation (FFT). The efficiency of the FFT is discussed in Appendix E on page 158.

4.6.2 Periodic supercells

Thus far we have considered systems with periodic symmetry, where we have made the assumption that a unit cell may be repeated through all of space to represent the macroscopic solid under consideration. Figure 4.2 on the following page is a schematic representation of the basic unit cell which is replicated throughout space.

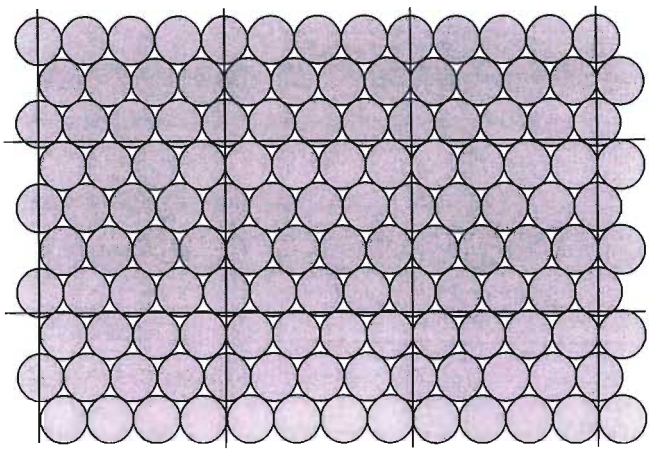

Figure 4.2 Schematic representation of a periodic unit cell repeated through all of space

Surfaces, defects, and interfaces are non-periodic in nature. Within the current periodic model, then, a method of modelling these is required. In the case of a defect, the periodic unit cell is extended so that it is large enough to isolate the defects from one another. This larger unit cell is called a *supercell*. Figure 4.3 below represents a defect in a periodic supercell.

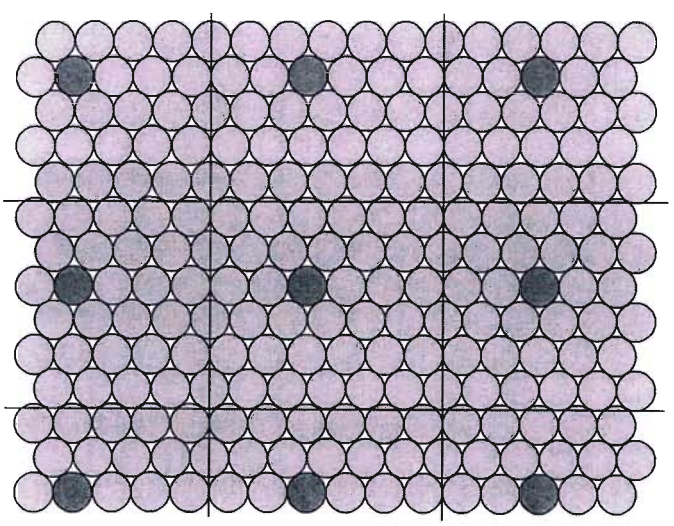

Figure 4.3 Schematic representation of a supercell containing a single, "isolated" defect atom.

In a similar way surfaces may be modelled within the supercell, allowing enough vacuum layers to prevent the two surfaces created as a result of periodic boundary conditions from interacting with one another.

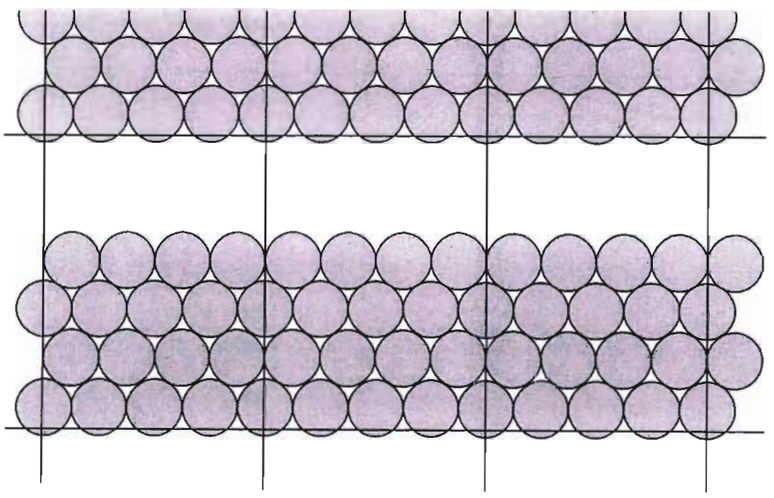

Figure 4.4 Schematic representation of a surface supercell with 2 vacuum layers and 4 slab layers.

Chapter 5

Investigations of Mixing Schemes

5.1 Introduction

Once the charge density has been determined in a particular iteration, it is used to determine the input charge density for the subsequent iteration. However, if this charge density alone is used as the input density, the charge has a tendency to oscillate in subsequent iterations, causing numerical instabilities. These oscillations are particularly severe for large supercells for which the long wavelength (ie small $\boldsymbol{G}$) changes to the charge density are amplified by the Coulomb potential, which is proportional to $\frac{n(\boldsymbol{G})}{G^2}$.

These oscillations should be damped in order to prevent divergence. This damping is done by a variety of possible mixing schemes, in which various combinations of charge densities are taken as the input charge density in subsequent iterations.

Complex systems with a large number of atoms in the unit cell require an efficient means of obtaining convergence. One of the ways in which one can accelerate the convergence of a calculation is to use an appropriate mixing scheme for the system under consideration. This chapter explores three such mixing schemes, and compares their convergence for various system sizes.

5.2 Linear mixing

The mixing scheme originally used in the BEST codes is the linear mixing scheme, which is the simplest of the possible mixing schemes. Here, the input charge density for the following iteration is a linear combination of the input and output densities from the current iteration:

$$n_{in}^{(m+1)} = (1 - \alpha)\, n_{in}^{(m)} + \alpha\, n_{out}^{(m)} \quad . \tag{5.1}$$

The superscript m in this equation indicates the iteration index. The value for α is chosen empirically, and should to be in the range [0,1]. With a suitable choice of α, convergence is usually achievable. Larger values of α ensure a rapid rate of convergence of the total energy. However, if this value of α is too large, numerical instability is likely to occur, as the charge density is not being sufficiently damped for subsequent iterations. On the other hand, a small α value, although ensuring numerical stability, will require a greater number of iterations for self-consistency in the results. In Figure 5.1 below, the number of self-consistent iterations required for convergence of the total energy for a 3-iridium-atom unit cell is plotted against the mixing parameter α.

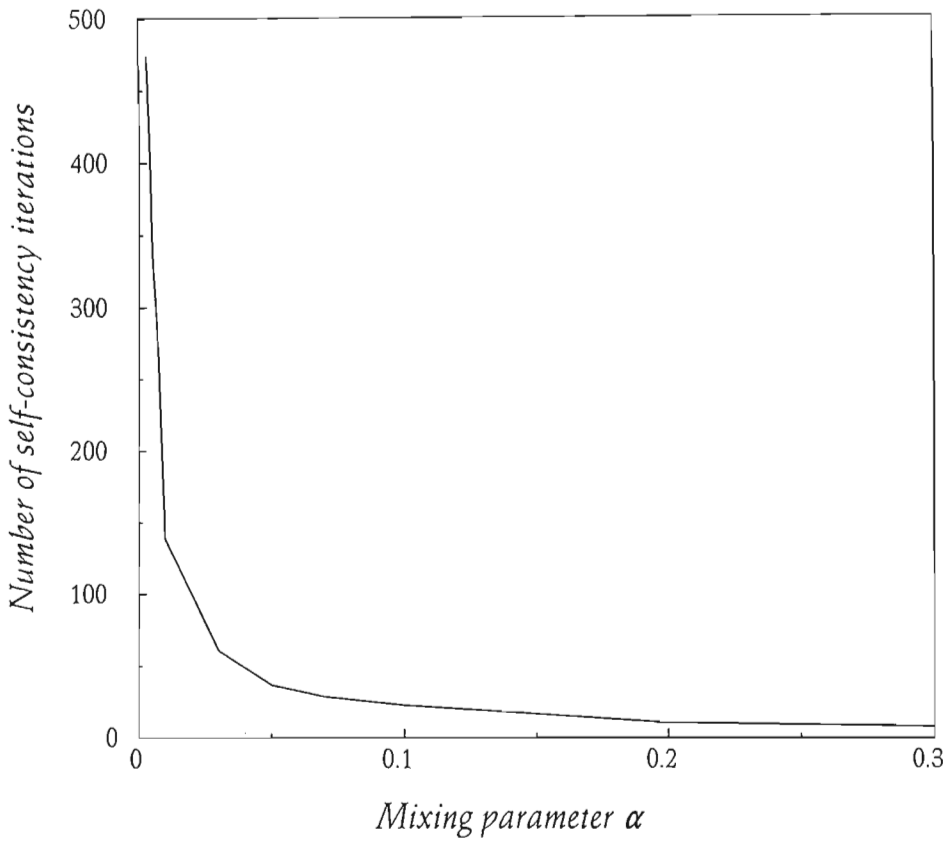

Figure 5.1 Graph of number of self-consistency iterations required for converged total energy result versus linear mixing parameter α

With the linear mixing scheme, convergence can be extremely slow at times. For example, in the case of the iridium 12-atom unit cell, α can not be greater than 0.005 (which is a 99.5% mixing of input density with 0.5% output density) if a converged result is to be achieved. This requires an undesirably large number of iterations, in excess of 500. An improved means of mixing the charge densities is thus required.

5.3 Anderson's mixing

Anderson[56] developed a method which was later suggested as a means of mixing the charge densities in electronic structure calculations by Hamann[57]. This mixing method is an extension of the linear mixing scheme. Here, the input and output densities which are to be mixed are constructed as linear combinations of the true input and output densities from the current and previous iterations:

$$\bar{n}_{in}^{(m)} = (1 - \beta)\, n_{in}^{(m)} + \beta\, n_{in}^{(m-1)} \quad , \tag{5.2}$$

and

$$\bar{n}_{out}^{(m)} = (1 - \beta)\, n_{out}^{(m)} + \beta\, n_{out}^{(m-1)} \quad . \tag{5.3}$$

We define a vector $\boldsymbol{F}$ to be the distance between the input and output densities:

$$F^{(m)}(n) = n_{out}^{(m)} - n_{in}^{(m)} \quad . \tag{5.4}$$

To determine the best value for β to be used in equations **(5.2)** and **(5.3)**, the distance between the two average densities $\bar{n}_{in}^{(m)}$ and $\bar{n}_{out}^{(m)}$ is minimized. This is done by setting

$$\frac{\partial D\,[\,\bar{n}_{in}, \bar{n}_{out}\,]}{\partial \beta} = 0 \quad , \tag{5.5}$$

where D is the norm of the vector $\boldsymbol{F}$.

One hence obtains a value for β by solving the following equation:

$$\beta = \frac{F^{(m)} \cdot (F^{(m)} - F^{(m-1)})}{D^2 [F^{(m)}, F^{(m-1)}]} \quad . \tag{5.6}$$

The new estimate for the input charge density is then found by mixing the average input and output densities:

$$n_{in}^{(m+1)} = (1 - \alpha)\, \bar{n}_{in}^{(m)} + \alpha\, \bar{n}_{out}^{(m)} \quad , \tag{5.7}$$

where α is again chosen empirically. Figure 5.2 illustrates the relationship of the number of self-consistent iterations required for convergence of the total energy for a 3-iridium-atom unit cell with the mixing parameter α.

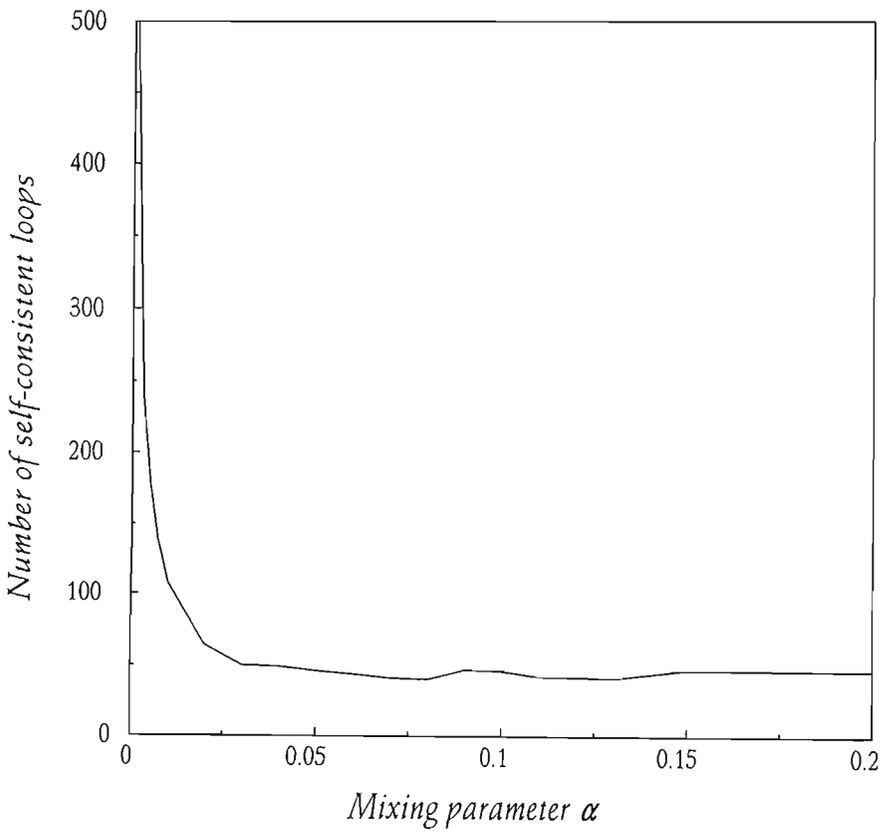

Figure 5.2 Graph of number of self-consistency iterations for converged total energy result versus Anderson mixing parameter α

In the case of the iridium 12-atom unit cell calculation, α is required to be less than 0.3 in order for convergence to be achieved. Approximately 200 iterations are consequently required for convergence of the total energy. Although this is an improvement over the linear mixing scheme, it remains undesirably high, indicating that an even more efficient scheme is sought after.

5.4 The modified Broyden's mixing scheme

In 1965 Broyden[58] developed an iterative mixing procedure, based on the quasi-Newton-Raphson method, which ensured extremely fast convergence rates. For large system sizes, however, this method is undesirable as it requires the storage and inversion of very large (N×N) matrices. Srivastava[59] suggested a modification to this method in which only the storage of m vectors of length N is required, where m is the number of iterations.

In a similar way to the Anderson method, a vector $\boldsymbol{F}$ is defined to be the distance between the input and output densities:

$$F^{(m)}(n) = n_{out}^{(m)} - n_{in}^{(m)} \quad , \tag{5.8}$$

in which, by the variational principle, one requires convergence to $\boldsymbol{F}=0$.

The vector equation for updating the charge density at each step is:

$$n_{in}^{(m+1)} = n_{in}^{(m)} + \xi^{(m)} \quad , \tag{5.9}$$

where

$$\xi^{(m)} = \beta F^{(m)} - \sum_{i=2}^{m} c_{mi} u^{(i)} \quad . \tag{5.10}$$

In this equation

$$u^{(i)} = \beta (F^{(i)} - F^{(i-1)}) + (n^{(i)} - n^{(i-1)}) - \sum_{j=2}^{i-1} a_{ij} u^{(j)} \quad , \tag{5.11}$$

$$a_{ij} = v^{T(j)} (F^{(i)} - F^{(i-1)}) \quad , \tag{5.12}$$

$$c_{mi} = v^{T(i)} F^{(m)} \quad , \tag{5.13}$$

and

$$v^{T(i)} = \frac{(F^{(i)} - F^{(i-1)})^T}{(F^{(i)} - F^{(i-1)})^T (F^{(i)} - F^{(i-1)})} \quad . \tag{5.14}$$

It should be noted that in equation **(5.11)**, the sign preceding the last term is incorrect in the original paper, where it appears as a positive sign. This sign should be negative.

Since the Hartree potential is proportional to $\frac{n(G)}{G^2}$, errors in the density are amplified in the long-wavelength limit. This may result in "charge sloshing", and hence give rise to numerical instabilities in the total energy. This is particularly the case with the modified Broyden scheme, and leads to severe instabilities in large supercell calculations. The problem may be overcome by dividing the charge density by $\boldsymbol{G}^2$ at the start of each mixing subroutine, effectively meaning that one mixes the potentials, rather than the densities. At the end of the mixing subroutine, one multiplies again by $\boldsymbol{G}^2$, before returning to the main program.

5.5 Comparison of mixing schemes

For a simple system, the choice of mixing scheme does not make a vast difference in the rate of convergence of the total energy. Figure 5.1 shows the convergence results of the linear, Anderson and modified Broyden mixing schemes applied to a single atom iridium calculation in the FCC structure. In this instance the Anderson mixing scheme is the most efficient, with convergence being obtained in 6 iterations.

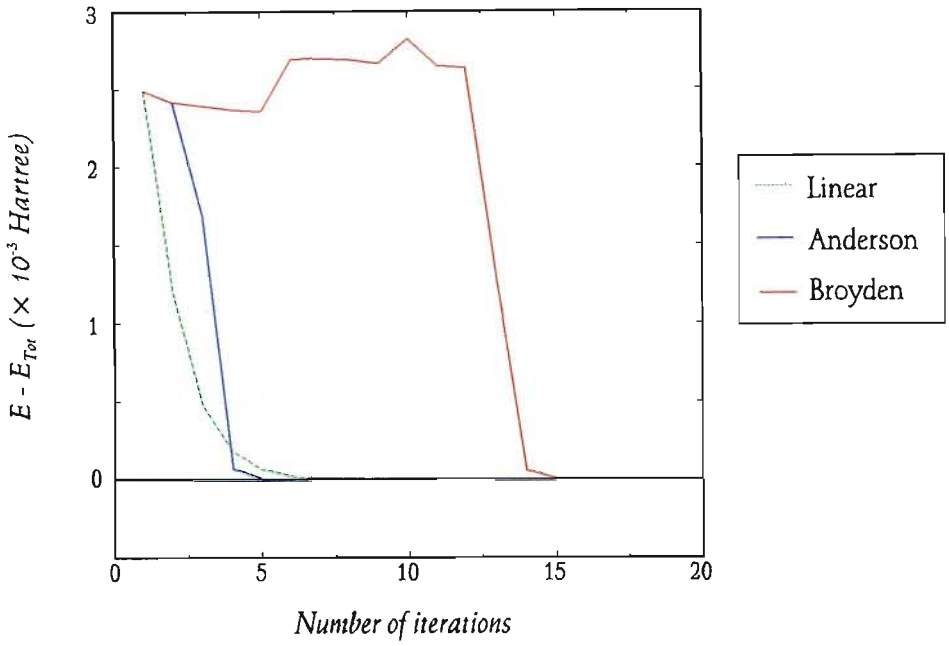

Figure 5.1 Convergence of calculated total energy for linear, Anderson, and modified Broyden mixing schemes for Ir 1-atom unit cell

For a larger system, however, the choice of mixing scheme makes a distinct difference in the convergence of the total energy. Calculations on a 12-atom FCC Iridium unit cell have been performed by way of illustration. Figure 5.2 indicates that the convergence with the modified Broyden scheme is substantially quicker than that with the Anderson and linear mixing schemes. The linear mixing scheme requires in excess of 500 iterations for self-consistency to be reached, and the Anderson scheme requires approximately 200 iterations. The modified Broyden scheme requires only ~40 steps, and hence reduces the computational time by at least a factor of 10 over the linear scheme.

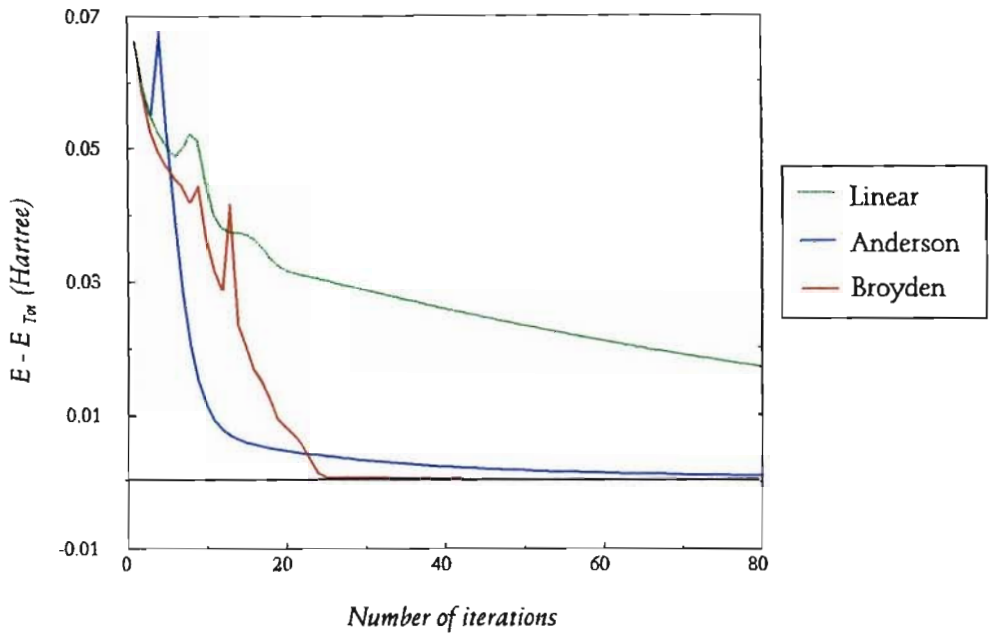

Figure 5.2 Convergence of calculated total energy for linear, Anderson and modified Broyden mixing schemes applied to Ir 12-atom unit cell.

As a consequence of these convergence studies with various mixing schemes, the calculations on large Iridium unit cells all make use of the modified Broyden mixing scheme.

5.6 Optimisation of the modified Broyden mixing scheme

5.6.1 Storage of past information

When using the modified Broyden mixing scheme, in order to ensure the most rapidly converged result for the total energy calculation, various input parameters should be optimised. As was indicated in Section 5.4, information about the charge density from previous iterations is stored, and used in subsequent computations when determining the

new input charge density. Using all previous values for the charge density is not, however, optimally efficient, as the convergence is slow for large systems, and memory is used unnecessarily. A parameter, n_{store} , is built into the mixing scheme which indicates the number of iterations for which charge density information from previous iterations is used.

When n_{store} is varied, the number of iterations required for self-consistency differ substantially. Convergence tests of the number of iterations required for self-consistency versus n_{store} using a 6-atom iridium supercell are shown in Figure 5.3 on the following page.

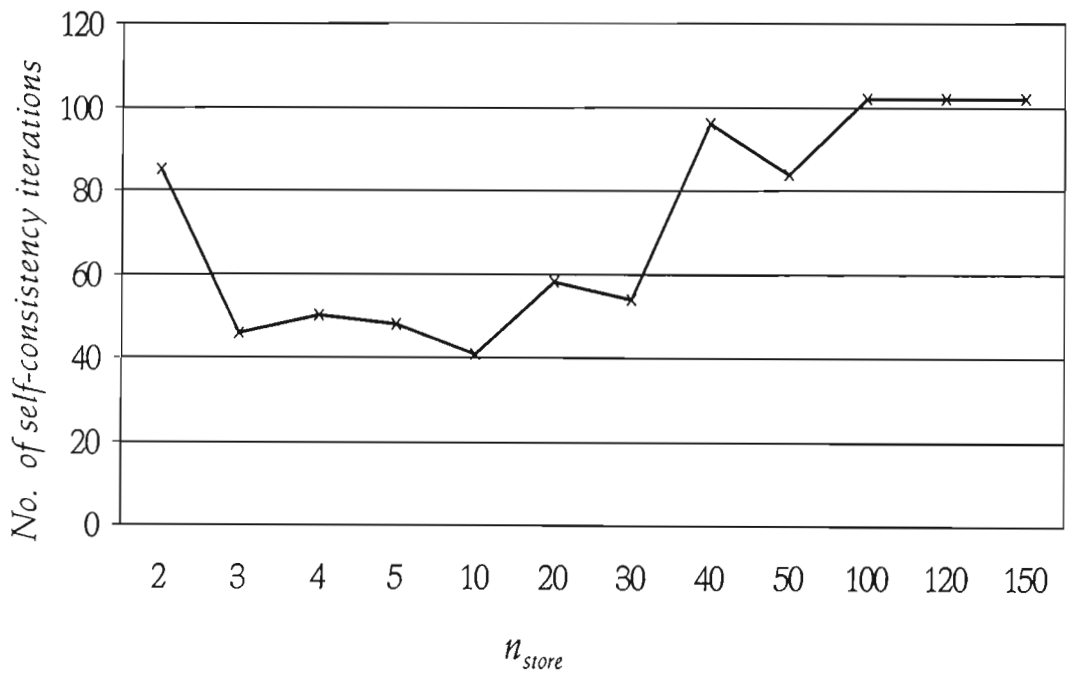

Figure 5.3 Graph of number of self-consistency iterations required for converged total energy result versus n_{storer}

This graph indicates that the optimal number of steps for this particular calculation for which previous information about the charge densities should be stored is 10. If n_{store} is set to infinity, in other words, if all previous information about the charge densities is stored, the number of steps required for self-consistency is more than double that with $n_{store}=10$.

5.6.2 The mixing parameter

In the modified Broyden scheme, the value for the mixing parameter, β, is fairly arbitrary for a simple system, such as a 1-atom calculation. For more complex systems the calculation becomes unstable with high values of β. Convergence tests of the required number of iterations with respect to mixing parameter β for a 6-atom iridium supercell are shown in Figure 5.4.

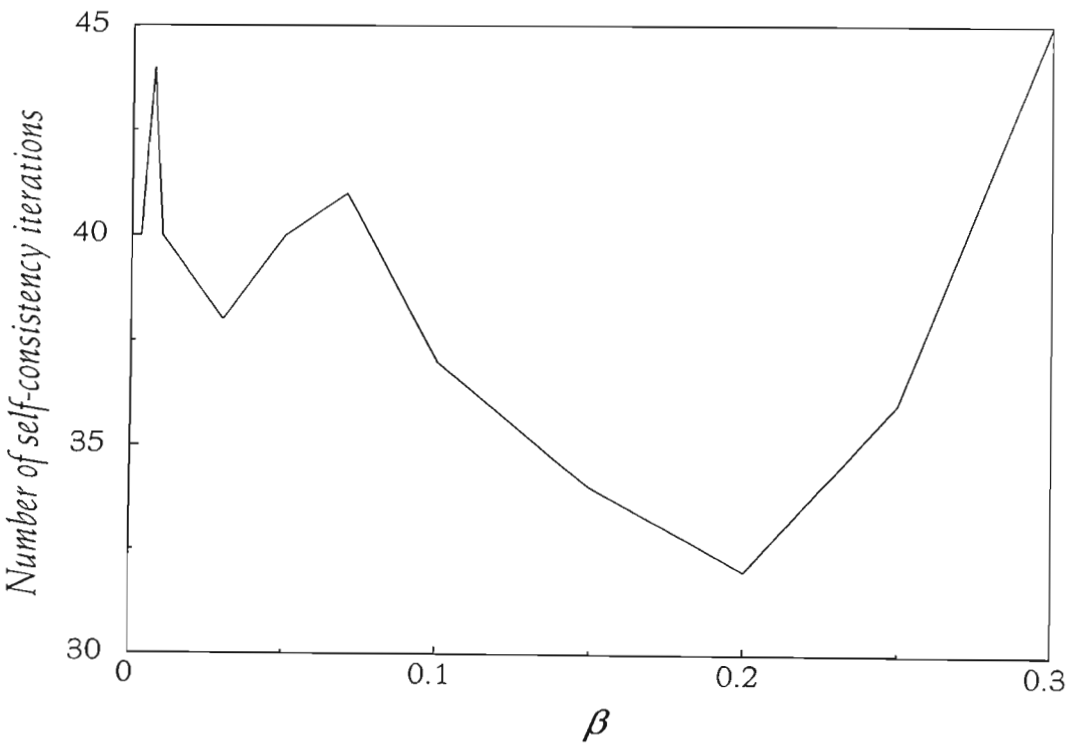

Figure 5.4 Graph of number of self-consistency iterations required for converged total energy result versus Broyden mixing parameter β

For this system, setting β>0.3 leads to a numerically unstable result. Zero mixing, in other words β=0, also leads to numerical instabilities. Values between these lead to varying numbers of iterative steps required for convergence. An optimal value of β=0.2 is found for this system.

A similar convergence test on a 12-atom iridium supercell indicates a numerically unstable result with β=0.2, and the lowest number of iterations required for self-consistency is found at β=0.1. A similar optimal value is found for a 9-atom iridium supercell calculation.

It appears, then, that although the optimal value for the mixing parameter may vary slightly between systems, fairly rapid and stable convergence may be guaranteed with a value of β=0.1.

Chapter 6

Applications with Iridium I: Iridium under pressure

6.1 Introduction

Iridium was discovered in 1803 by Smithson Tennant when the process of dissolving crude platinum by aqua regia, a mixture of nitric and hydrochloric acids, left a small amount of black residue. This residue was named iridium, derived from the Greek word "iris" (meaning rainbow), due to the range of colours of its salts. It is a metal of the platinum family.

Iridium is the most corrosion resistant of all the metals. For this reason it was used, in a 10% iridium - 90% platinum alloy, in making the metre-bar in Paris. This property of corrosion resistance makes it an ideal material for a number of "clean" applications, such

as resistive heating experiments. Iridium is resistant to the effects of acids, as well as to aqua regia, a mixture which can dissolve such metals as gold and platinum.

Iridium is an extremely hard and brittle metal, being unmalleable at temperatures below 1200°C. Its melting point is approximately 2440°C. It therefore has a high degree of thermal and structural stability, and is therefore the metal of choice for encapsulating the power systems of unmanned spacecraft, providing a mechanically very secure shield. It is also used for making crucibles and other apparatus which need to withstand high temperatures, like thermocouples and electrical contacts.

It is uncertain whether iridium or osmium is the densest of the known elements. Their densities having been calculated as 22.65 and 22.61 g/cm^3 respectively, while specific gravity measurements indicate a higher value for osmium[60]. Iridium crystallizes in the FCC structure. It has a relatively high bulk modulus, a value of 355GPa having been measured[61]. This high bulk modulus makes it an ideal material for use as a high-pressure gasket, for instance in a diamond anvil cell. The stability of the FCC phase of this material, especially under pressure, is therefore of interest.

6.2 Bulk properties of iridium

6.2.1 Review of past studies

A limited number of studies have been made of the bulk properties of iridium. Ivanov *et al*[62] studied the elastic properties, phonon spectra, vacancies, interstitials, dislocations, and stacking defects, using an empirical pseudopotential which they constructed on the basis of the work of Greenberg *et al*[63]. Heid *et al*[64] used a first principles pseudopotential mixed-basis method to compute elastic constants and phonon dispersions for iridium, and obtained good agreement with experimental results. To date there do not appear to have been many further attempts at performing first principles calculations on the bulk properties of iridium.

6.2.2 Bulk properties

In the present work, the core radii chosen for the construction of the pseudopotential were r_s=2.41 Bohr, r_p=3.14 Bohr, and r_d=1.15 Bohr, for the valence s, p and d orbitals respectively. The local component of the pseudopotential was chosen to be the ℓ=0 component. For the FCC structure consisting of 1 atom per unit cell 110 special $\boldsymbol{k}$-points were considered. This corresponds to a sampling of 4000 points in the entire zone.

The results of the calculations are presented in Table 6.1, together with other known experimental and theoretical results.

Table 6.1 Reference, lattice constant a_0 in Å, cohesive energy E_{coh} in eV, and the bulk modulus B in GPa.

Reference	**a_0(Å)**	**E_{coh} (eV)**	**B (GPa)**
Present work at 50Ryd†	3.85	9.35	402
Present work at 70Ryd	3.85	9.58	399
Present work at 100Ryd	3.85	10.23	385
Plane-wave pseudopotential method, Filippetti *et al*[65]	3.86	-	420
Full-potential LMTO method, Boisvert *et al*[66]	3.81	10.31	-
Experimental, Cerenius *et al*[67]	3.84	-	306
Experimental, Touloukian *et al*[68]	3.83	-	-
Kittel[61]	-	6.94	355

† Energy cut-off for plane wave expansion of wavefunctions

The equilibrium lattice constant was found, in the present work, to be 3.85Å for all three choices of E_{cut}. The value for the bulk modulus was closer to the expected value at the higher cut-off energy, but the cohesive energy was found, fortuitously, to be closer to experimental values at the lower cut-off of 50 Rydberg. The cohesive energy values are far from the expected values, which is not surprising, as the LDA is known for its overestimation of the cohesive energy, with errors being mostly due to an overestimate of the free atomic energy - total energies of the solid are reasonably well computed in the LDA.

It was decided, for computational efficiency, to use a value of 50 Rydberg for E_{cut} for further calculations with iridium, as it appears that results are sufficiently converged with this value.

6.3 High pressure studies of iridium

6.3.1 Review of past studies

Cerenius *et al*[67] recently performed high pressure experiments on iridium, using a diamond-anvil cell, and found a transition to a 14-layer supercell structure at pressures in excess of 60GPa. This structure was reversible under reduction of the pressure, and was observed on a second X-ray diffraction machine.

Using X-ray diffraction spectra, they found a substantial increase in the (111) peak, together with a clear saw-tooth pattern at these high pressures. They could not explain these patterns by the formation of stacking fault defects, but instead claimed that this could be indicative of a distortion of the FCC lattice consistent with a 14-layer supercell structure.

6.3.2 High pressure phases of iridium

The transition metals tend to exhibit phase changes between the FCC, HCP, and BCC phases. Iridium was hence studied in these phases in the present work, in order to explore whether a phase transition could occur under pressure from the FCC structure to either one of these crystallographic structures. For FCC and BCC, 1 atom per unit cell was used, and 2 atoms per cell for HCP. A comparable $\boldsymbol{k}$-point sampling of the Brillouin zone was chosen for all three systems. The equilibrium lattice parameters for HCP were found by varying both a and c independently. The nearest neighbour distance, a, was found to be 2.74Å, and c was found to be 4.42Å, with a c/a ratio of 1.62. (The ideal value for the c/a ratio is 1.63.) The equilibrium volume per atom was found to be 14.37Å^3 for the HCP

structure, which is higher than that for FCC, which is 14.27Å^3. Figure 6.1 below shows graphs of the energy per atom versus volume per atom for the three structures.

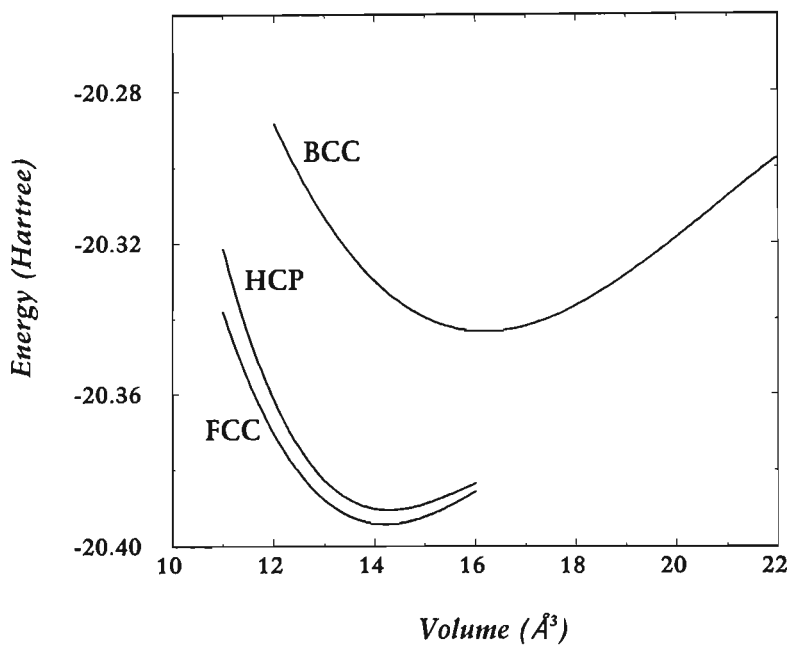

Figure 6.1 Energy versus volume for the FCC, HCP and BCC phases of Iridium

It is clear from this graph that the BCC structure is inaccessible under pressure, due to its much higher energy values than those for the FCC structure. In addition, the common tangent line for these two curves indicates that a negative pressure would be required for a phase change from FCC to BCC, which is unphysical. The energy versus volume curves for the HCP and FCC structures do not intersect at high pressures. Our calculations therefore predict that there is no phase transition from FCC to HCP for iridium for pressures up to 60GPa.

6.3.3 Modelling planar defects

6.3.3.1 Introduction

The stacking faults in the (111) direction for both the HCP and FCC structures can be described by means of a sequence of planes labelled A, B, or C, which correspond to the three possible positions of the atoms in a [111] plane. No two neighbouring planes may have the same label, as this corresponds to an unstable, high energy stacking structure which is not ordinarily reasonable. The ideal FCC structure would hence be represented by the sequence:

$$\text{FCC}: \quad \ldots A\,B\,C\,A\,B\,C \ldots \quad ,$$

and the HCP structure by the sequence

$$\text{HCP}: \quad \ldots A\,B\,A\,B\,A\,B \ldots \quad .$$

For an N-layer supercell structure with periodic boundary conditions, there are approximately 2^N distinct stacking configurations, including the so called extrinsic (E), intrinsic (I), and twin (T) faults. The extrinsic fault, in which an additional plane is inserted in the FCC stacking sequence, is represented by:

$$\text{E}: \quad \ldots A\,B\,\dot{C}\,B\,\dot{A}\,B\,C \ldots \quad .$$

Here the dot indicates a plane which has a local HCP-like environment.

In a similar way, a stacking sequence containing an intrinsic stacking fault (I) in the FCC structure, in which the lattice is sheared by the displacement of an entire plane, can be represented by the sequence:

$$\text{I:}\quad \ldots A\,B\,\dot{C}\,\dot{B}\,C\,A\,B\,C\ldots\quad .$$

The twin stacking fault (T), which contains mirror symmetry around the faulted plane, can be represented by the sequence of planes:

$$\text{T:}\quad \ldots A\,B\,\dot{C}\,B\,A\,C\ldots\quad .$$

Since it is not possible to study all $\sim 2^N$ possible stacking sequences from first principles, a finite number of systems was considered. These were used together with a model, called the "bond-orientation model", to calculate the energies of all possible defects in the 14-layer supercell. This model is outlined below.

6.3.3.2 The bond-orientation model

The bond-orientation model, developed by Chetty and Weinert[7], consists of a representation of the energy of each atom in a stacking sequence within its local environment to two planes above and two planes beneath it. This leads to six distinct geometries with which one can model the energetics of any sequence of stacking planes. These six geometries are depicted in Figure 6.2. The ε_i indicate the associated single-atom energy parameters. These parameters are functions of the nearest neighbour distance a.

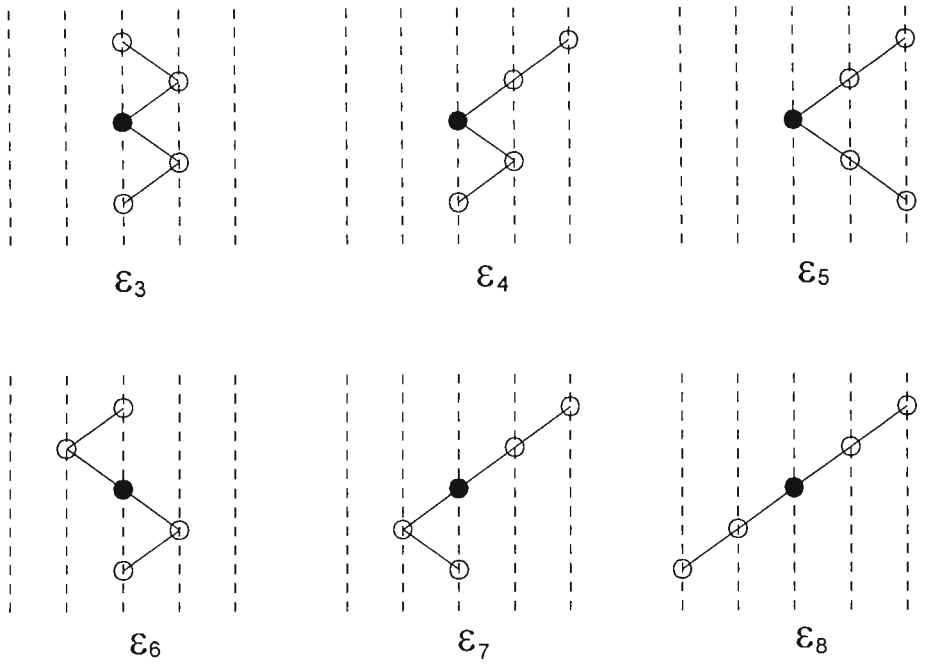

Figure 6.2 Local geometry configurations for stacking in (111) direction together with associated energy parameters.

In order to obtain values for these $\varepsilon_i(a)$, energies for a number of 6- and 7-atom unit cells were calculated as a function of nearest-neighbour distance a. The energy for these unit cells can be expressed as a linear combination of the relevant energy parameters, $\varepsilon_i(a)$, associated with the local environment of each of the atoms in the stacking sequence of the unit cell. For instance, the FCC unit cell represented by the stacking sequence ... *A B C A B C* ... consists of six atoms, each in a locally ε_8 environment. One may therefore represent the energy of this unit cell as:

$$E_{\mathrm{FCC}}(a) = 6\,\varepsilon_8 \quad . \tag{6.1}$$

Table 6.2 shows the 6- and 7-atom defect structures which were considered. The associated energy as a function of lattice constant, together with the energy expressed in terms of the relevant bond orientation parameters, are also shown in the table.

Table 6.2 Defect structures, bond-orientation parameters, and associated cubic fit parameters, in units of Hartree to energy vs nearest neighbour distance.

Supercell structure	**Bond-orientation parameters**	c_0 ‡	c_1	c_2	c_3
A B C A B C	$6\,\varepsilon_8(a)$	87.6081822	-115.59858	21.1373154	-1.28305287
A B A B A B	$6\,\varepsilon_3(a)$	99.0398503	-122.348853	22.4723882	-1.37133444
A B A B A C	$\varepsilon_3(a)+2\varepsilon_4(a)+\varepsilon_5(a)+2\,\varepsilon_6(a)$	87.9295048	-115.701217	21.1442002	-1.28279103
A B C B A C	$2\varepsilon_5(a)+4\varepsilon_7(a)$	87.6769923	-115.603458	21.1324679	-1.28240307
A B C B A B C	$2\varepsilon_5(a)+\varepsilon_6(a)+2\,\varepsilon_7(a)+2\varepsilon_8(a)$	102.412925	-134.898875	24.6538463	-1.49578876

‡ c_n indicates coefficient of x^n in cubic expression for the first-principles energy as a function of lattice constant a, and has the units of Hartree/(Å)^n

From the cubic fits to the first principles energies of each of the structures shown in Table 6.2, the $\varepsilon_i(a)$ parameters may be extracted by solving simultaneously the equations listed in the above table. All energies are referred to that for the FCC structure. This effectively sets $\varepsilon_8(a)=0$. As a consequence of a hidden symmetry which exists in the system, there is a maximum of 5 linearly independent equations for the parameters. This symmetry is due to the fact that only certain sequences of the $\varepsilon_i(a)$ are possible. For instance, the local geometry $\varepsilon_8(a)$ may only be followed by $\varepsilon_7(a)$, which in turn may only be followed by $\varepsilon_5(a)$ or $\varepsilon_4(a)$.

Once the energy parameters have been determined, one can compute the energy of any possible stacking sequence using an appropriate combination of the $\varepsilon_i(a)$.

6.3.4 Exploring planar defects in the 14-atom supercell using the bond-orientation model

In order to investigate the claims made by Cerenius *et al* that a 14-layer superlattice exists for iridium under pressures in excess of 60 GPa, the bond-orientation model was used to study the planar defects of a 14-atom supercell. The model was extended to include the energy dependence on volume to enable the study of systems under pressure. The 14-atom ideal structures are expressed in terms of the bond-orientation model in the following way:

$$E_{FCC}(a) = 14\,\varepsilon_8(a) \quad , \tag{6.2}$$

and

$$E_{HCP}(a) = 14\,\varepsilon_3(a) \quad . \tag{6.3}$$

By way of example, the twin stacking fault, which has the following structure in the 14-atom supercell:

$$\mathrm{T}: \quad \ldots C\,A\,B\,C\,A\,B\,\dot{C}\,B\,A\,C\,B\,A\,C\,\dot{B}\ldots \quad ,$$

is expanded in terms of the $\varepsilon_i(a)$ in the following way:

$$E_T(a) = 2\,\varepsilon_5(a) + 4\,\varepsilon_7(a) + 8\,\varepsilon_8(a) \quad . \tag{6.4}$$

In a similar way the energies of all $\sim 2^{14}$ possible defect structures may be modelled. Due to the high level of degeneracy in the system, there are only 60 distinct expansions which exist in terms of the bond-orientation parameters. Figure 6.3 contains all 60 curves, which represent all possible defect structures in the 14-atom supercell. The energies are bounded below by the FCC curve, and above by the HCP curve. There is no common tangent

which links the FCC curve with any of the other curves. In addition, there is a relatively large energy jump from the FCC curve to the nearest one above it. Our calculations therefore show that these defect structures are not attainable under pressures up to 60 GPa.

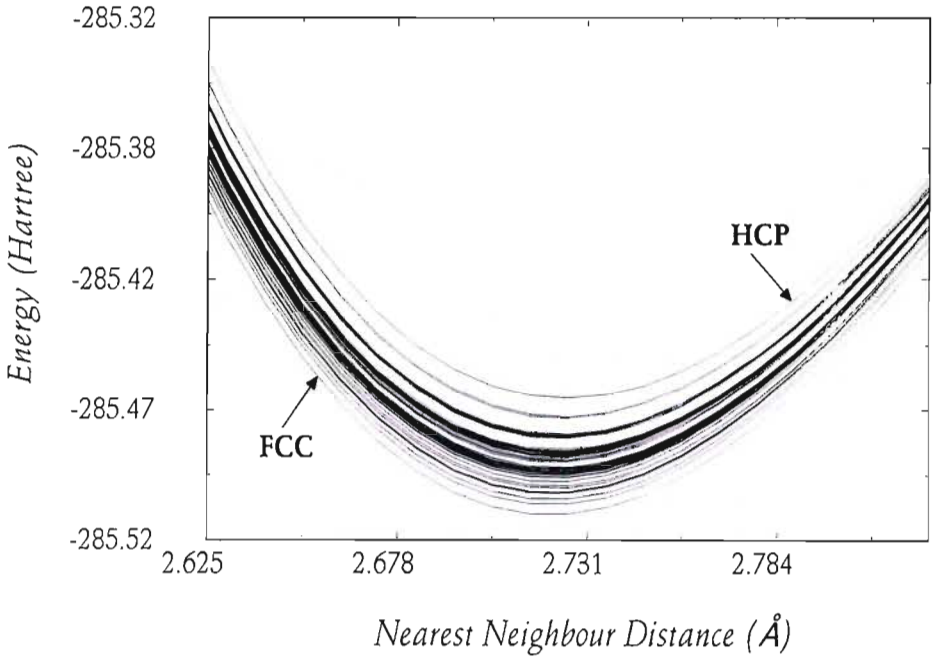

Figure 6.3 Energy versus nearest neighbour distance for all ~2^{14} defect structures in the 14-atom supercell with periodic boundary conditions.

6.4 Stacking fault energies

The plane wave pseudopotential method has been used to study the stacking fault energies of iridium. The FCC structure in a 12-atom supercell oriented in the (111) direction was modelled with the choice of Monkhorst-Pack parameters for the $\boldsymbol{k}$-point sampling of (442). The HCP structure was also considered with the same supercell size and Brillouin zone sampling.

The twin, extrinsic, and intrinsic stacking faults were also considered, with their supercells represented by:

$$\text{T}: \quad \ldots A\,B\,C\,A\,B\,\dot{C}\,B\,A\,C\,B\,A\,\dot{C}\ldots \quad ,$$

$$\text{E}: \quad \ldots A\,B\,C\,A\,B\,\dot{C}\,B\,\dot{A}\,B\,C\,A\,B\,C\ldots \quad ,$$

and

$$\text{I}: \quad \ldots A\,B\,C\,A\,B\,\dot{C}\,\dot{B}\,C\,A\,B\,C\ldots \quad .$$

The T supercell has 12 atoms per unit cell, and its energy therefore may be compared directly with that of the FCC supercell, since their $\boldsymbol{k}$-point sampling is identical. Due to periodic boundary conditions, the T supercell has two faulted planes.

The E supercell has 13 atoms per cell, which is dissimilar to the 12 atoms per cell of the HCP structure. The sampling of the Brillouin zone in the $\boldsymbol{z}$-direction is therefore not identical. The larger number of planes in this direction for the E supercell requires a smaller sampling of the Brillouin zone compared with the FCC structure if we wish the

sampling of the Brillouin zones in this direction to be comparable. The energy of the E supercell with a Monkhorst-Pack ***k***-point mesh of (442) was initially compared with that of the FCC supercell with a (443) mesh to give a best estimate of the formation energy for this stacking fault. The E supercell energy with a (442) mesh was then compared with that for the FCC supercell with a (442) mesh to give a lower bound for the formation energy.

Since the I supercell has 11 atoms per cell, a best estimate for the energy was found by comparing its energy using a (443) mesh with that of the FCC cell using a (442) mesh. The lower bound was found using a (442) mesh for both.

The consequent formation energies, together with their lower bounds, where relevant, are shown in Table 6.3.

Table 6.3 Supercell structure, best estimate of formation energy, and lower bound for the formation energy, in meV.

Supercell	**Formation energy (meV)**	**Lower bound for formation energy (meV)**
HCP	80	-
T	54	-
E	128	122
I	137	137

6.5 Conclusion

Our calculations lead to the conclusion that no exotic phase or superlattice structure exists for iridium under pressure. It should be noted that in these calculations we have assumed conditions of hydrostatic pressure, thus not taking into account the possibility of uniaxial stresses, inhomogeneous strains etc., which may have arisen during the experimental process. Further experimental measurements are required in order to ascertain the nature of the apparent 14-layer superlattice structure observed by Cerenius *et al*[67].

The bond-orientation model, which in this instance has been extended to include a description of systems under pressure, is a convenient and accurate means of computing the energies of planar defect structures. In addition, the stacking fault energies of iridium have been calculated from first principles.

Chapter 7

Applications with Iridium II: Study of Clean and Relaxed Surfaces

7.1 Introduction

There have been a number of theoretical studies of the three low-index surfaces of iridium, namely the (100), (110) and (111) surfaces, for instance by Filippetti *et al*[65], Fiorentini *et al*[69], Tyson *et al*[70], and van Beurden *et al*[71]. The work of Fiorentini *et al* takes complete atomic relaxations into account, allowing for relaxations of all of the atomic layers. Fiorentini *et al* and van Beurden *et al* only allow for relaxations of the top layer, making the crude assumption that all other layers remain fixed. Tyson *et al* make no allowance for relaxations in their calculations.

Since no studies to date have considered convergence of the surface formation energy with regard to ***k***-point sampling, and with regard to the number of atomic layers considered in the unit cell, the present work explores this, allowing for full atomic relaxations, for each of the low-index surfaces of iridium.

7.2 The Ir(111) surface

Figure 7.1 below shows the (111) surface for an FCC crystal.

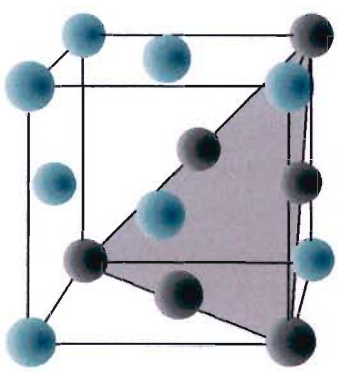

Figure 7.1 FCC structure with shaded plane indicating (111) surface

If this shaded plane is represented in the plane of the paper, the hexagonal symmetry becomes evident, as is shown in the Figure 7.2.

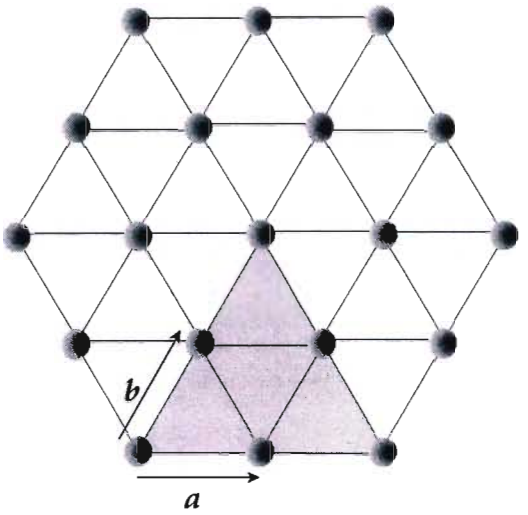

Figure 7.2 Diagrammatic representation of [111] surface showing hexagonal symmetry and ***a*** and ***b*** spanning vectors (in the plane of the paper) for the unit cell

The smallest unit cell is a rhombus in the x-y plane with the following spanning vectors:

$$\boldsymbol{a} = (a_n, 0, 0) \quad , \tag{7.1}$$

$$\boldsymbol{b} = (\frac{1}{2} a_n, \frac{\sqrt{3}}{2} a_n, 0) \quad , \tag{7.2}$$

$$\boldsymbol{c} = (0, 0, \sqrt{6} a_n) \quad , \tag{7.3}$$

where a_n is the nearest-neighbour distance.

To generate the ABC stacking sequence, the required basis vectors are:

$$\tau_1 = (0,0,0) \quad , \tag{7.4}$$

$$\tau_2 = \left(\frac{1}{2}a_n, \frac{1}{2\sqrt{3}}a_n, \frac{\sqrt{2}}{\sqrt{3}}a_n\right) \quad ,$$

$$\tau_3 = (0, \frac{1}{\sqrt{3}}a_n, \frac{2\sqrt{2}}{\sqrt{3}}a_n) \quad .$$

In our investigation of the clean (111) surface, we use a supercell with a 1x1 dimension in the ***x-y*** plane, while varying the number of atomic layers in the ***z***-direction in order to investigate convergence with respect to supercell size. For this purpose, we use 6, 9 and 12 atomic layers respectively. We compute the surface formation energies in the following manner:

$$\sigma = \frac{(E_{slab} - NE_{bulk})}{2} \quad ,$$

where N is the number of atoms in the slab, and E_{bulk} is the bulk energy of a single iridium atom. We divide by 2 since there are 2 equivalent surfaces in each supercell.

By varying the parameters of the Monkhorst-Pack ***k***-point mesh, we can also explore convergence of the energy with number of ***k***-points. The parameter sets we use are (221), (442), (662) and (664). We allow for full relaxation of the surfaces, by allowing each atomic layer to relax until the atomic forces are negliglibly small. The results of our calculations are shown in Table 7.1.

Table 7.1 Parameters for Monkhorst-Pack ***k***-point mesh, surface formation energy σ in eV, relaxed surface formation energy σ_{relax} in eV, and surface relaxation energy in meV, for 6, 9 and 12 atomic layers for Ir(111) surface

6 atomic layers (4 bulk layers + 2 vacuum layers)				
***k*-point mesh**	**No. of special *k*-points**	**σ (eV)**	**σ_{relax} (eV)**	**Relaxation energy (meV)**
(221)	4	1.033	0.986	46
(442)	16	1.052	1.048	4
(662)	36	1.094	1.084	10
(664)	72	1.096	1.086	10

9 atomic layers (5 bulk layers + 4 vacuum layers)				
***k*-point mesh**	**No. of special *k*-points**	**σ (eV)**	**σ_{relax} (eV)**	**Relaxation energy (meV)**
(221)	4	1.322	1.250	71
(442)	15	1.047	1.043	4
(662)	31	1.116	1.107	9
(664)	62	1.117	1.108	9

12 atomic layers (6 bulk layers + 6 vacuum layers)				
***k*-point mesh**	**No. of special *k*-points**	**σ (eV)**	**σ_{relax} (eV)**	**Relaxation energy (meV)**
(221)	7	1.291	1.222	70
(442)	29	1.059	1.052	6
(662)	60	1.109	1.098	11
(664)	120	1.109	1.100	9

The graph in Figure 7.3 illustrates the convergence of the energy with respect to supercell size and ***k***-point sampling. The dotted line in each case represents the relaxed energy, which for obvious reasons is always lower than the unrelaxed surface formation energy.

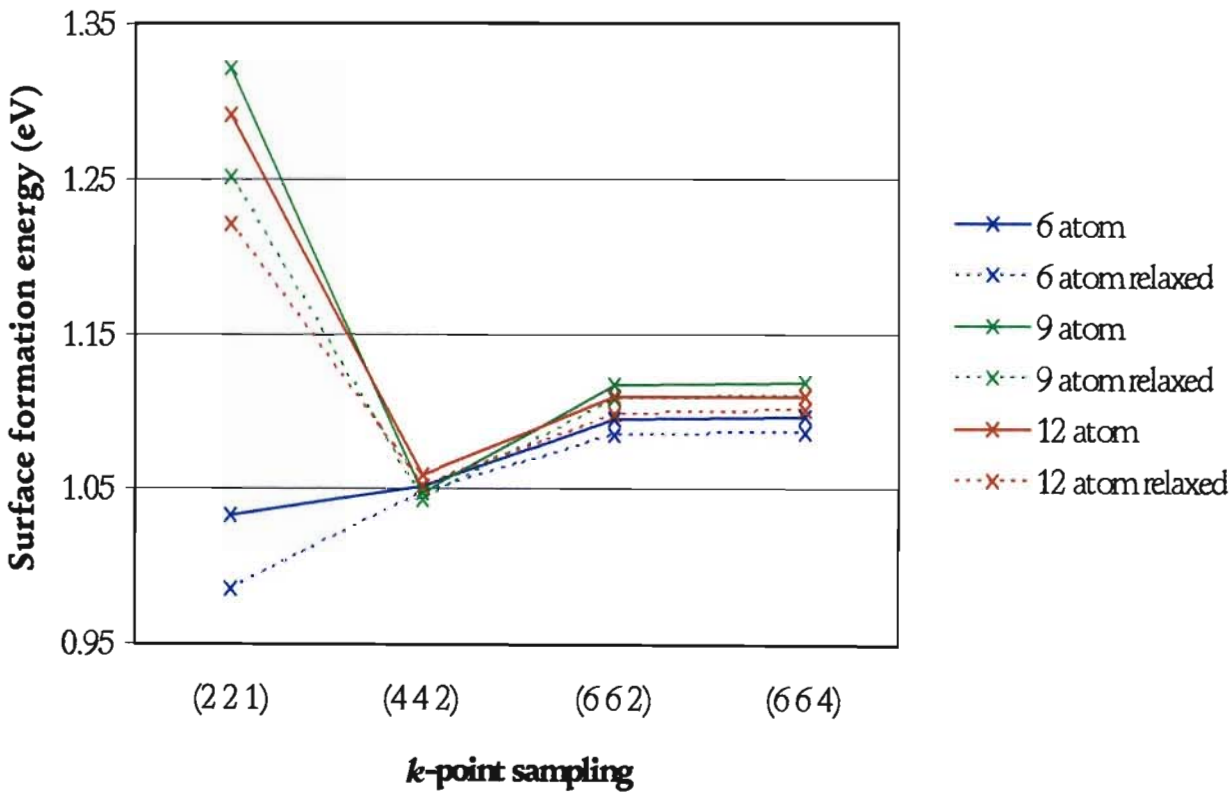

Figure 7.3 Graph of Ir(111) surface formation energies in eV (including fully relaxed energies) for 6, 9 and 12 atomic layer supercells, plotted with respect to ***k***-point sampling.

7.3 The Ir(110) surface

Figure 7.4 shows the (110) surface for a FCC crystal.

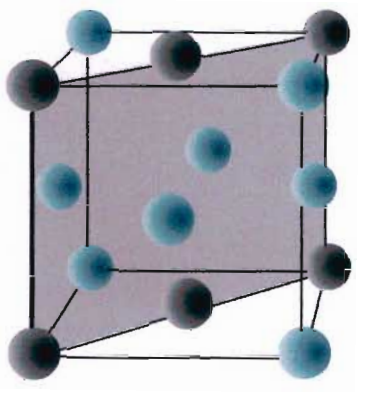

Figure 7.4 FCC structure with shaded plane indicating (110) surface

The smallest unit cell is a rectangle with the spanning vectors:

$$\boldsymbol{a} = (a_n, 0, 0) \quad , \tag{7.8}$$

$$\boldsymbol{b} = (0, \sqrt{2}\, a_n, 0) \quad , \tag{7.9}$$

$$\boldsymbol{c} = (0, 0, a_n) \quad , \tag{7.10}$$

where a_n is the nearest-neighbour distance. The basis vectors for the positions of the atoms in the unit cell are:

$$\tau_1 = (0, 0, 0) \quad , \tag{7.11}$$

$$\tau_2 = \left(\frac{1}{2} a_n, \frac{1}{\sqrt{2}} a_n, \frac{1}{2} a_n\right) \quad . \tag{7.12}$$

In our investigation of the clean (110) surface, we again use a supercell with a 1x1 dimension in the ***x-y*** plane, while using 6, 8, 10 and 12 atomic layers respectively in the ***z***-

direction. As with the (111) surface, we investigate convergence of the energy with respect to ***k***-point sampling, and we allow for full atomic relaxations. The results of our calculations are shown in Table 7.2 below.

Table 7.2 Parameters for Monkhorst-Pack ***k***-point mesh, surface formation energy σ in eV, relaxed surface formation energy σ_{relax} in eV, and surface relaxation energy in meV, for 6, 8, 10 and 12 atomic layers for Ir(110) surface

6 atomic layers (4 bulk layers + 2 vacuum layers)				
***k*-point mesh**	**No. of special *k*-points**	**σ (eV)**	**σ_{relax} (eV)**	**Relaxation energy (meV)**
(221)	1	2.396	2.158	238
(442)	4	2.318	2.254	64
(662)	9	2.344	2.248	99
(664)	18	2.373	2.274	96

8 atomic layers (4 bulk layers + 4 vacuum layers)				
***k*-point mesh**	**No. of special *k*-points**	**σ (eV)**	**σ_{relax} (eV)**	**Relaxation energy (meV)**
(221)	1	2.127	1.884	243
(442)	4	2.440	2.258	182
(662)	9	2.528	2.366	161
(664)	18	2.506	2.344	161

10 atomic layers (5 bulk layers + 5 vacuum layers)				
***k*-point mesh**	**No. of special *k*-points**	**σ (eV)**	**σ_{relax} (eV)**	**Relaxation energy (meV)**
(221)	1	2.524	2.279	245
(442)	4	2.322	2.166	156
(662)	9	2.464	2.293	171
(664)	18	2.451	2.279	171

12 atomic layers (6 bulk layers + 6 vacuum layers)				
***k*-point mesh**	**No. of special *k*-points**	**σ (eV)**	**σ_{relax} (eV)**	**Relaxation energy (meV)**
(221)	1	2.662	2.426	237
(442)	4	2.225	2.071	154
(662)	9	2.411	2.291	120
(664)	18	2.417	2.297	120

The graph in Figure 7.5 illustrates the convergence of the energy with respect to supercell size and ***k***-point sampling.

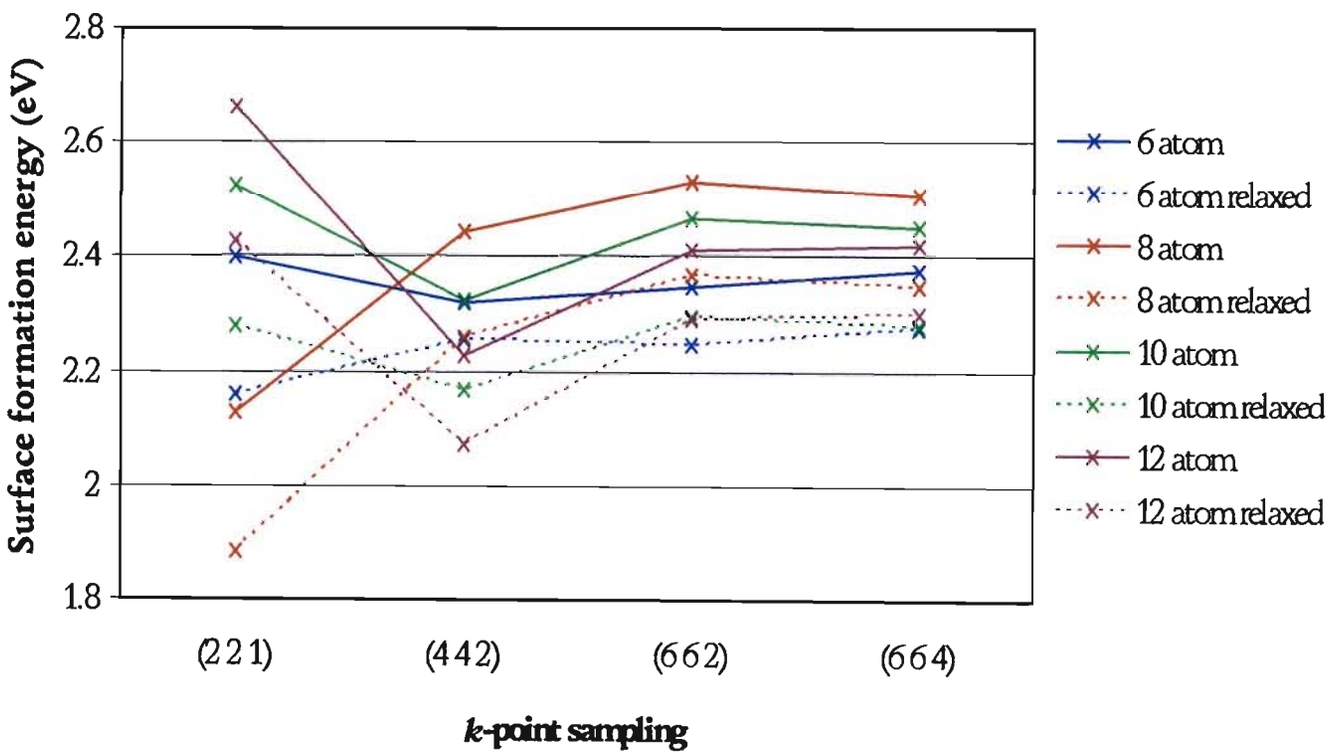

Figure 7.5 Graph of Ir(110) surface formation energies in eV (including fully relaxed energies) for 6, 8, 10 and 12 atomic layer supercells, plotted with respect to ***k***-point sampling

7.4 The Ir(100) surface

Figure 7.6 below shows the (100) surface for a FCC crystal.

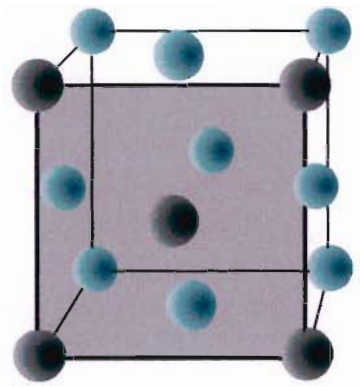

Figure 7.6 FCC structure with shaded plane indicating (100) surface

The smallest unit cell is a square with the spanning vectors:

$$\boldsymbol{a} = \left(\frac{1}{\sqrt{2}}a_n, -\frac{1}{\sqrt{2}}a_n, 0\right) , \tag{7.13}$$

$$\boldsymbol{b} = \left(\frac{1}{\sqrt{2}}a_n, \frac{1}{\sqrt{2}}a_n, 0\right) , \tag{7.14}$$

$$\boldsymbol{c} = (0, 0, a_n) ,$$

where a_n is the nearest-neighbour distance. The basis vectors for the stacking sequence are:

$$\tau_1 = (0, 0, 0) , \tag{7.16}$$

$$\tau_2 = \left(0, \frac{1}{\sqrt{2}}a_n, \frac{1}{\sqrt{2}}a_n\right) . \tag{7.17}$$

Here again, a supercell with a 1x1 dimension in the ***x-y*** plane is used in the calculations, the number of atomic layers in the ***z***-direction varying between 6, 8, 10 and 12. The results of our calculations are shown in Table 7.3 below.

Table 7.3 Parameters for Monkhorst-Pack ***k***-point mesh, surface formation energy σ in eV, relaxed surface formation energy σ_{relax} in eV, and surface relaxation energy in meV, for 6, 8, 10 and 12 atomic layers for Ir(100) surface

6 atomic layers (4 bulk layers + 2 vacuum layers)				
***k*-point mesh**	**No. of special *k*-points**	**σ (eV)**	**σ_{relax} (eV)**	**Relaxation energy (meV)**
(221)	1	1.803	1.192	611
(442)	3	1.534	1.468	66
(662)	6	1.644	1.625	19
(664)	12	1.663	1.644	19

8 atomic layers (4 bulk layers + 4 vacuum layers)				
***k*-point mesh**	**No. of special *k*-points**	**σ (eV)**	**σ_{relax} (eV)**	**Relaxation energy (meV)**
(221)	1	1.967	1.363	604
(442)	3	1.592	1.525	67
(662)	6	1.667	1.647	20
(664)	12	1.663	1.643	20

10 atomic layers (5 bulk layers + 5 vacuum layers)				
***k*-point mesh**	**No. of special *k*-points**	**σ (eV)**	**σ_{relax} (eV)**	**Relaxation energy (meV)**
(221)	1	2.001	1.533	468
(442)	3	1.585	1.496	89
(662)	6	1.654	1.605	48
(664)	12	1.662	1.614	48

12 atomic layers (6 bulk layers + 6 vacuum layers)				
***k*-point mesh**	**No. of special *k*-points**	**σ (eV)**	**σ_{relax} (eV)**	**Relaxation energy (meV)**
(221)	1	1.976	1.260	716
(442)	3	1.582	1.503	79
(662)	6	1.622	1.586	35
(664)	12	1.611	1.576	36

The graph in Figure 7.7 illustrates the convergence of the energy with respect to supercell size and ***k***-point sampling.

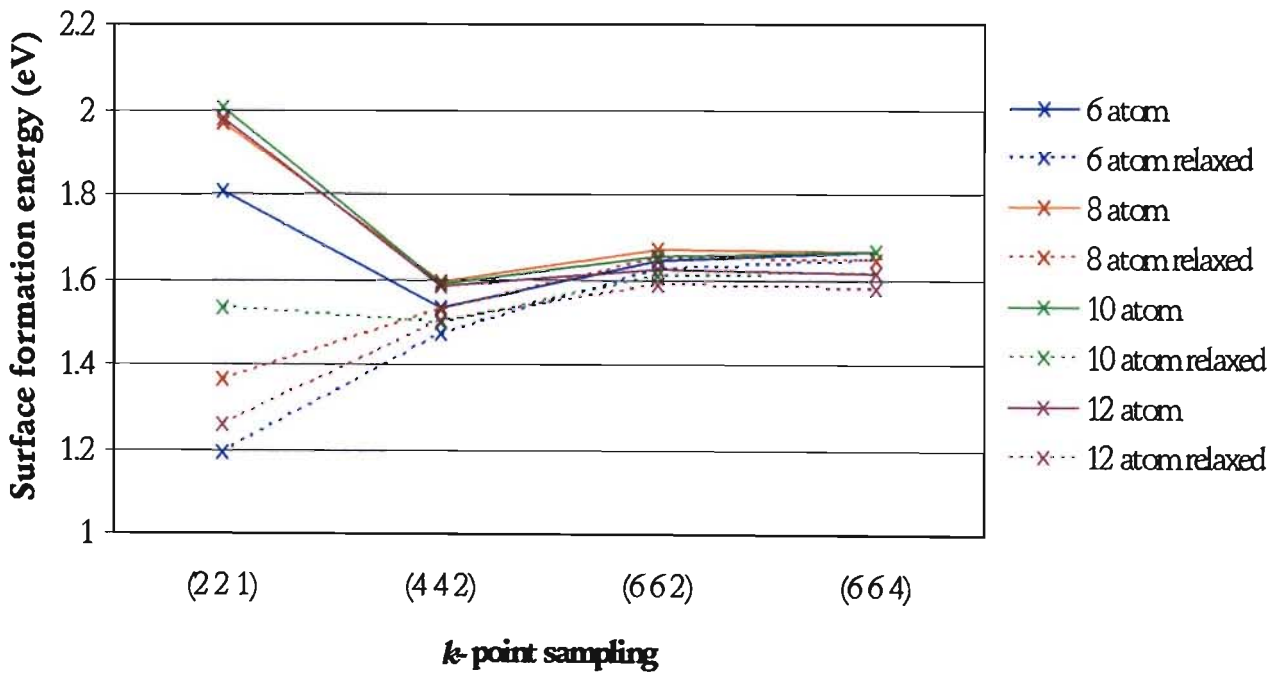

Figure 7.7 Graph of Ir(100) surface formation energies in eV (including fully relaxed energies) for 6, 8, 10 and 12 atomic layer supercells, plotted with respect to ***k***-point sampling.

7.5 Summary of clean and relaxed surface results

The total energy is not variational with respect to the number of ***k***-points. Hence it is not strictly true that a higher number of ***k***-points will ensure a lower energy result. In order to obtain the most plausible result for the surface formation energy from our calculations, we find the mean value for the energy from all results with a Monkhorst-Pack ***k***-point sampling mesh of (662) and (664) for each of the low-index surfaces. The standard deviation from the mean is used as an indication of the error bar in each result. We present these results in Table 7.4 below, together with other experimental and theoretical values for the purposes of comparison.

Table 7.4 Reference and relaxed surface formation energy σ_r in eV for each of the low-index surfaces for iridium

Reference	σ_r **(111)** **(eV)**	σ_r **(110)** **(eV)**	σ_r **(100)** **(eV)**
Present work	1.10±0.01	2.30±0.04	1.62±0.03
Filippetti *et al*[65] (relaxed)	1.31	2.59	1.85
Tyson *et al*[70] (unrelaxed)	1.07	2.83	1.36
Fiorentini *et al*[69] (relaxed)	-	-	1.73

As is evident from the results, the surface formation energy for the Ir(111) surface is lower than that for the other two surfaces. This is because only 3 nearest-neighbour bonds are broken when the surface is formed. The (110) surface requires the highest amount of energy for its formation as 5 bonds between nearest-neighbours are broken in this process. By contrast, the formation of the Ir(100) surface involves the breaking of 4 nearest-neighbour bonds.

Table 7.5 contains the results of our computations for the relaxations of the atomic planes with respect to one another, as a percentage of the ideal bulk spacing. We have included results by other authors for purposes of comparison.

Table 7.5 Reference and surface layer relaxations as percentage of the ideal bulk spacing for the low-index surfaces of iridium. (Negative values indicate inward relaxation)

Ir(111) surface			
Reference	**Δd_{12}**	**Δd_{23}**	**Δd_{34}**
Present work	-1.8	0.1	0.2
DFT (LDA), Filippetti *et al*[65]	-1.3	-0.2	0.0
DFT (GGA), van Beurden *et al*[71]	-2.1	-	-
Experimental, Watson *et al*[72]	-2.6±4.5	-	-

Ir(110) surface			
Reference	**Δd_{12}**	**Δd_{23}**	**Δd_{34}**
Present work	-9.2	2.5	-1.5
DFT (LDA), Filippetti *et al*[65]	-11.6	5.4	-1.3

Ir(100) surface			
Reference	**Δd_{12}**	**Δd_{23}**	**Δd_{34}**
Present work	-2.7	1.3	0.6
DFT (LDA), Fiorentini *et al*[69]	-3.0	-	-
DFT (LDA), Filippetti *et al*[65]	-3.8	1.0	-0.5
DFT (GGA), van Beurden *et al*[71]	-4.8	-	-
Experimental, Watson *et al*[72]	-3.6±0.5	-	-

The low values for the interplanar relaxation for the Ir(111) surface are due to the close-packed nature of this surface. There is relatively little room for the movement of the atomic layers. The inward relaxation in each case is caused by the atoms attempting to regain some of the lost electronic charge density due to the broken bonds with the atomic layer above the surface. Since the formation of the Ir(110) surface requires 5 nearest-neighbour bonds to be broken, this inward relaxation is high, as the atoms lose a high proportion of their charge density. In addition, with just 2 nearest-neighbour atoms in the plane of the surface, there is a great likelihood of buckling at this surface. The (100) surface requires 4 nearest-neighbour bonds to be broken in the formation of the surface and therefore does not have the same extent of inward relaxation as does the (110) surface.

Chapter 8

Applications with Iridium III: Adatom Adsorption Studies

8.1 Introduction

An understanding of the growth of crystals is important to more accurately be able to control the growth process, and to ensure high quality crystals. This has important applications in the area of optoelectronic and semiconductor devices, chemical catalysts, as well as in the refinement of metals, plastics and ceramics. It is hence important that the process of homoepitaxial growth be fully understood, which is the process whereby a crystal is grown by deposition of adatoms of identical nature onto the surface. This subject has therefore received a large amount of attention by both experimentalists and theoreticians.

The process of adsorption of iridium adatoms onto the (111) surface of iridium, and the diffusion of these adatoms across the surface, has received particular interest in the last few decades since a number of interesting phenomena have been observed in this process.

8.2 Review of experimental work

A key instrument used by experimentalists in the study of surface phenomena in transition metals is the field ion microscope (FIM), since it has the ability to image individual atoms on the surface, and is therefore ideally suited for the quantitative study of surface atomic processes. The section to follow offers a brief introduction to this instrument.

8.2.1 The field ion microscope

Although the FIM offers atomic resolution, the principle on which it operates is remarkably simple. An electrically insulated specimen, in the form of a needle tip which is 10 to 100 nm in radius, is positioned 5 cm in front of a phosphor screen, inside a vacuum system. Once the system has been cooled to between 20 and 100 K, a small amount of He or Ne gas is released into the vacuum system. At the same time, a positive voltage is slowly applied to the specimen. Eventually the electric field at the tip of the specimen becomes large enough to remove an electron from one of the gas atoms (which is loosely attached to the surface), leaving a positively charged He^+ or Ne^+ ion on the surface of the tip. As this tip is also positively charged it will cause the ion to be repelled from the tip onto the screen, where the ion will produce a spot of light. The entire picture caused in this way is called *the field ion image*, and represents the positions of the

individual atoms on the surface of the tip. The magnification of this image is of the order of one million times the size of the tip.

8.2.2 The field ion microscope applied to iridium

Although the FIM cannot be used for all metals due to the high electric field that is required for the imaging, it has been used successfully in the study of a number of transition metal surfaces such as platinum, rhodium, nickel, tungsten and iridium.

Wang *et el*[1] used the FIM to observe single Ir adatoms on the Ir(111) surface. Their findings were that in only 63 out of the 455 observations, adatoms were found to occupy FCC sites, the remainder being located at HCP sites. In other words, a single adatom is located at an HCP site in 85% of the cases, and on an FCC site in only 15% of the observations made. The energy difference between the HCP and the FCC sites was measured to be 0.370kcal/mol (16.0meV/atom). They measured the diffusion barrier between these two types of sites, finding the activation energy for atomic migration, E_A, to be 6.2±0.1kcal/mol (0.269±0.004eV/atom). Their observations led them to pose the question of the nature of Ir crystal growth if single adatoms indicate a preference for HCP sites. Subsequent findings by Wang *et al*[2] were that, although single Ir adatoms prefer HCP sites, trimers show no preference for either site, tetramers favour FCC sites 85% of the time, and heptamers are found exclusively on FCC sites. Thus, as the number of Ir atoms in the cluster increases, so does the likelihood of the cluster occupying FCC surface sites.

In other work in which these authors[3] were studying the diffusion of individual adatoms on the Ir(111) surface, it was found that the diffusion process most likely to occur on this surface is the movement of an adatom from an HCP site to a neighbouring FCC site (via the bridge site), and then back to an HCP site, in other words jumps between nearest-

neighbour sites. Diffusion by direct jumps from HCP to HCP sites, or FCC to FCC sites, was found to be less likely. They subsequently[4] measured the diffusion energy barrier for an adatom moving from an HCP to an FCC site to be 6.22±0.7kcal/mol (0.270±0.03eV/atom), and that for an adatom moving from an FCC to an HCP site to be 5.72±0.7kcal/mol (0.248±0.03eV/atom). Chen *et al*[5] performed similar measurements on adatom diffusion on the Ir(111) surface using the FIM and found the diffusion barrier to be 0.022±0.03eV. They did not distinguish the path direction. (It should be noted that there appears to be an error in their reporting of this value, as it contradicts all other experimental findings by a factor of 10).

8.3 Review of theoretical work

The experimental work of Wang *et al* discussed above was soon followed by theoretical work on this system, in an attempt to understand the behaviour of adatoms on the Ir(111) surface from a theoretical perspective. Piveteau *et al*[73] used the tight-binding method to calculate the binding energies at HCP and FCC sites on the (111) surface. They performed their calculations in real space, considering the perturbation of 22 atoms of the substrate within a sphere which is centred on the adatom. In this way they considered only the relaxation of the nearest-neighbour atoms, which is not a complete account of the relaxation process. These authors found the HCP site to be lower in energy by 21.5 meV, (compared with 16.0meV found by Wang *et al*[1].) They also computed the energy barrier to adatom diffusion and found that in moving from an FCC to an HCP site, this barrier is 0.241 eV, while for a move from an HCP to an FCC site the energy barrier is 0.255 eV. It should be noted here that the difference in these respective energies, namely 14 meV, contradicts their finding of a 21.5 meV energy difference between FCC and HCP adatom sites.

Boivert *et al*[74] used the full-potential linear-muffin-tin-orbital technique in the context of Density Functional Theory (in the Local Density Approximation) to determine the energy barriers to adatom diffusion on the Ir(111) surface. Atomic relaxations were not taken into account completely here, as their codes make no allowance for the calculation of forces. They relaxed the outer atomic layer manually by finding the minimum in the total energy as a function of interplanar relaxation. They used 7 special $\boldsymbol{k}$-points (including the Γ-point) for the (2×2) surface supercell, with only 1 point along the $\boldsymbol{k}_z$-direction. They considered a 5-layer slab of bulk material, a single adatom layer, and a 6-layer vacuum region. Their supercell was symmetric so that both surfaces were identical. They computed the energy of an adatom at an FCC site to be 0.02eV lower than that for an HCP site, and claimed that this value is supported by Wang *et al*[4]. However, the paper that they refer to indicates a lower energy at the HCP site (as described in Section 8.2.2 above.) This seems to indicate that their calculations are incorrect, or that their paper includes a misprint. Diffusion may occur by means of a process known as the exchange mechanism, in which a surface atom is promoted above the surface, and hence exchanged with the diffusing atom. These authors did not consider this mechanism, since the perturbations induced by this process are substantial, hence requiring prohibitively large supercells. They therefore only considered diffusion by "jumps" along the surface. They computed the energy barrier for a jump from an FCC to an HCP site (over a bridge site) to be 0.24±0.03eV, and compared this with experimental results of 0.22±0.03eV found by Chen *et al*[5] and 0.270±0.003eV as reported by Wang *et al*[4].

Papadia *et al*[75] used the tight-binding model to compute the energetics of monomer, dimer and trimer adatoms on the Ir(111) surface. They found that monomers and dimers show a preference for HCP sites, while trimers favour neither of the sites, both being of equal energy, in agreement with the findings of Wang *et al*[2]. These authors allowed for constrained relaxations (to a first order approximation), with the neighbouring atoms being displaced laterally to accommodate the adatom, which was displaced perpendicular to the surface. No specific energies were reported in this paper. Instead, the difference in

binding energy as a function of d-band filling was given. Similarly the displacements due to atomic relaxations were not given specifically, but were also computed as a function of d-band filling.

Habar *et al*[76] used a tight-binding scheme, together with a recursion method, to study various adatom cluster configurations on the Ir(111) surface. In their model they only considered the 5d orbitals, and did not take atomic relaxations into account. They studied various island configurations, and extracted effective cluster interaction energies (ECI's), and averaged these out for a number of configurations. These ECI's could then be used to compute the energy of some arbitrary configuration. Finite temperature Monte Carlo simulations were performed, and revealed the formation of compact islands at intermediate temperatures. At low temperatures atomic mobility was too low for large clusters to form, so that only small, compact clusters were found. At high temperatures the islands were also small in size due to the dominant effect of entropy. The difference between these islands and those formed at low temperature was that the former were more irregular in shape with less tendency towards clustering.

Habar *et al*[77] submitted a more complete set of results in their subsequent paper, in which they used an Ising model, in conjunction with ECI's, in order to perform Monte Carlo simulations on the Ir(111) surface at finite temperatures. They investigated the transition from HCP to FCC sites as a function of adlayer concentration, and found that as the concentration increased, so did the preference for FCC sites by the adatoms, as opposed to HCP sites at low concentration.

Hamilton *et al*[78] performed first-principles calculations in the GGA approximation, making use of ultrasoft pseudopotentials with a plane-wave energy cut-off of 191eV, to investigate adatom cluster diffusion over the Ir(111) surface. They computed the energy difference between a pseudomorphic adatom monolayer in the FCC and the HCP sites, and found this difference to be 81 meV. They found the energy of a single adatom at an

FCC site to be 18 meV greater than when situated at an HCP site, in close agreement with the experimental findings outlined earlier[1,4]. The remainder of their paper involves a semi-empirical modelling of the diffusion of large clusters, which is not relevant to the present work, as this is beyond the scope of first-principles calculations at the present time.

8.4 Review of semi-empirical work

A number of semi-empirical models have been applied to the study of the Ir(111) surface. Shiang *et al*[79] used a molecular-dynamics simulation, making use of semi-empirical Rosato-Guillope-Legrand potentials, to explore surface diffusion on the (100), (110), and (111) surfaces of iridium. Since these simulations are based on a classical inter-atomic potential, they are not highly accurate. These authors found the difference in single adatom binding energy between the FCC and HCP sites to be 0.03 eV, which is a factor of 2 more than that reported by Wang *et al*[1,4]. Their finding of the energy barrier across the bridge site of 0.17 eV is in accord with other theoretical and experimental results[4,5,74]. These authors reported that there was no exchange mechanism found on the Ir(111) surface during their simulation, the close-packed nature of this surface being the most likely explanation for this.

Chang *et al*[80] used the Embedded Atom Method (EAM) potential to study adatom, dimer and trimer diffusion on the (100), (110), and (111) surfaces of iridium. They found no evidence of an exchange mechanism for diffusion on the Ir(111) surface, in agreement with the previous authors. They found the cohesive energy of a single adatom on the surface to be 4.95 eV, making no distinction between the FCC or HCP sites, since in their calculations the energy difference between these two sites is negligibly small (≈0.1 meV). They found that for dimers, the nearest-neighbour distance pairs are the most stable,

whereas a dimer consisting of one atom on an HCP site and the other on an FCC site is energetically unfavourable. Their computed value for the energy barrier height for diffusion of a single adatom over a bridge site (0.11 eV) is approximately half the energy barrier values found by experimentalists[81,5].

Trushin *et al*[82] used the modified Lennard-Jones pair potential and the many-body Rosato-Guillope-Legrand potential to study the energy barriers for various diffusion processes over the flat and stepped Ir(111) surface. Of interest to the present work are the values they obtained for energy barriers to surface diffusion from HCP to FCC sites on the flat surface, these values being 0.24 eV using the Rosato-Guillope-Legrand potential, and 0.20 eV with the Lennard-Jones potential. They found the energy difference between an adatom on an FCC site and that on an HCP site to be less than 0.005 eV, (below the value of their error bars). It is unclear in this paper which of these sites is energetically more favourable.

Van Beurden *et al*[83] developed modified embedded-atom-method (MEAM) potentials for iridium, amongst other platinum-group metals, based on density functional theory calculations, and applied these potentials to the study of surface properties of these materials. They computed the adsorption energy for a single adatom to be 5.87eV, and the diffusion energy barrier to be 0.42eV. They found the FCC adatom site to be lower in energy than the HCP site by 0.06eV, which contradicts the experimental results outlined previously.

8.5 Adatom formation energy calculations

Since no theoretical work to date has taken full atomic relaxations into account, it is important that these be investigated fully. The present work explores the energy of a single adatom in both the FCC and HCP sites, and compares the fully relaxed results with those found by experimentalists.

In our investigations, we use a supercell with a 2×2 surface unit cell, while allowing the number of atomic layers within the cell to vary between 6 and 9. Ideally a 3×3 surface unit cell should be used in order to minimise interactions between adatoms in neighbouring supercells. Computational limitations, however, have placed confines on our calculations for the time being. In future work the larger supercell will be investigated. Tables 8.1 and 8.2 below contain the results of our calculations for an adatom incorporated onto an FCC site, and an HCP site respectively.

Table 8.1 Parameters for Monkhorst-Pack ***k***-point mesh, FCC adatom formation energy in eV, relaxed FCC adatom formation energy in eV, and FCC adatom relaxation energy in meV for 6 and 9 atomic layers for the 2×2 Ir(111) surface

6 atomic layers (4 bulk layers + 1 adatom layer + 1 vacuum layer)				
***k*-point mesh**	**No. of special *k*-points**	**FCC adatom energy (eV)**	**Relaxed FCC adatom energy (eV)**	**FCC adatom relaxation energy (meV)**
(221)	3	9.339	8.584	755
(442)	11	9.714	8.992	722

9 atomic layers (4 bulk layers + 1 adatom layer + 4 vacuum layers)				
***k*-point mesh**	**No. of special *k*-points**	**FCC adatom energy (eV)**	**Relaxed FCC adatom energy (eV)**	**FCC adatom relaxation energy (meV)**
(221)	3	9.315	8.458	857
(442)	11	10.002	9.173	829

Table 8.2 Parameters for Monkhorst-Pack ***k***-point mesh, HCP adatom formation energy in eV, relaxed HCP adatom formation energy in eV, and HCP adatom relaxation energy in meV, for 6 and 9 atomic layers for the 2×2 Ir(111) surface

6 atomic layers (4 bulk layers + 1 adatom layer + 1 vacuum layer)				
***k*-point mesh**	**No. of special *k*-points**	**HCP adatom energy (eV)**	**Relaxed HCP adatom energy (eV)**	**HCP adatom relaxation energy (meV)**
(221)	3	9.391	8.514	877
(442)	11	9.759	8.990	770

9 atomic layers (4 bulk layers + 1 adatom layer + 4 vacuum layers)				
***k*-point mesh**	**No. of special *k*-points**	**HCP adatom energy (eV)**	**Relaxed HCP adatom energy (eV)**	**HCP adatom relaxation energy (meV)**
(221)	3	9.384	8.416	968
(442)	11	10.047	9.168	880

The adatom energies are computed in the following manner:

$$E_{adatom} = E_{supercell} - NE_{bulk} - 2\sigma_{111} \quad ,$$

where N is the number of atoms in the supercell, and σ_{111} is the surface formation energy for the fully relaxed Ir(111) surface.

From these results, the difference in energy between the FCC adatom site and the HCP adatom site may be computed. These results are shown in Table 8.3 on the following page.

Table 8.3 Parameters for Monkhorst-Pack ***k***-point mesh, unrelaxed energy difference between HCP and FCC adatom sites, and relaxed energy difference between HCP and FCC adatom sites, both in meV, for 6 and 9 atomic layers for the 2×2 Ir(111) surface. A negative sign for this energy difference indicates that the HCP site is lower in energy than the FCC site.

6 atomic layers (4 bulk layers + 1 adatom layer + 1 vacuum layer)		
***k*-point mesh**	**Unrelaxed E_{HCP} - E_{FCC} (meV)**	**Relaxed E_{HCP} - E_{FCC} (meV)**
(221)	52	-70
(442)	45	-3

9 atomic layers (4 bulk layers + 1 adatom layer + 4 vacuum layer)		
***k*-point mesh**	**Unrelaxed E_{HCP} - E_{FCC} (meV)**	**Relaxed E_{HCP} - E_{FCC} (meV)**
(221)	69	-42
(442)	45	-6

It is interesting to note that, before allowing for relaxations, the energy of the adatom on the HCP site is higher than that on the FCC site. Once the structure is allowed to relax, the HCP adatom site is lower in energy. In Figure 8.1 on the following page the HCP and FCC adatom energies are plotted for the unrelaxed and relaxed structures. For this diagram the energies from the 6 atomic layer supercell with a (221) ***k***-point mesh are used, as these most clearly illustrate the effect of relaxations on the adatom energies.

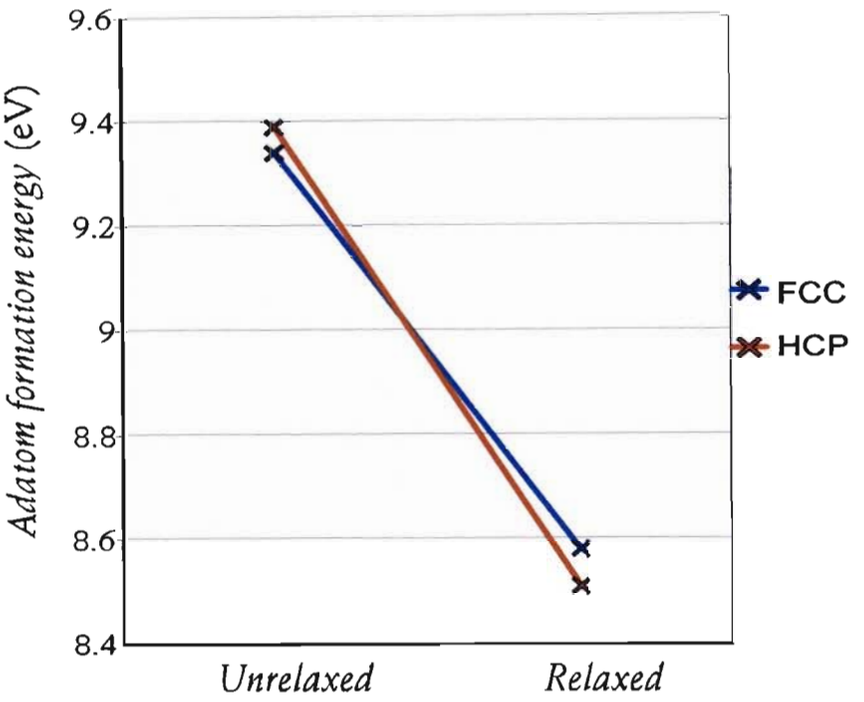

Figure 8.1 Graph of unrelaxed and relaxed single adatom formation energies on FCC and HCP sites.

Our results for the relaxed adatom energies compare favourably with the experimental values of Wang *et al*[1,4] which indicate the HCP adatom site to be lower in energy than the FCC site by 16.0±1.3meV[1] in one set of measurements, and 17.3±1.5meV[4] in another. Our deviations from this result could be due to finite size effects as a result of the limited size of the unit cell. We do not have the computational resources at present to study a more realistic 3×3 surface supercell.

The nature of the atomic relaxations may be investigated by observing the direction in which each atom in the unit cell is displaced. Figure 8.2 shows the displacement directions of the atoms with an adatom placed at the FCC surface site. Although only a (2×2) surface supercell is used in the calculations, the diagram includes a number of atoms from neighbouring surface cells to give a complete picture of the relaxations. All

mirror atoms, in terms of their position in the surface supercell, are indicated with the same number.

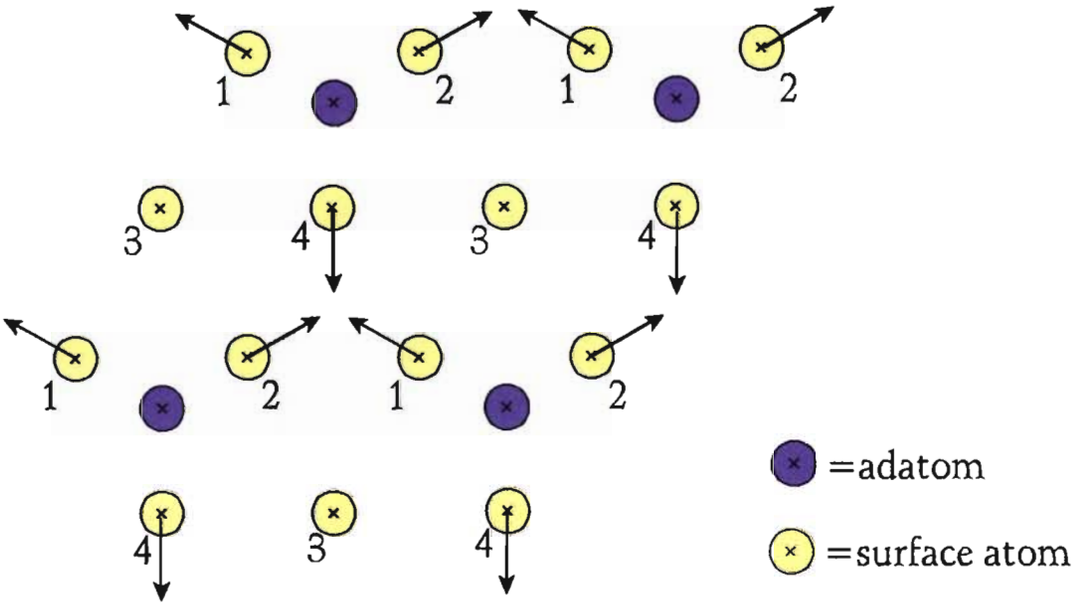

Figure 8.2 Relaxations of atoms due to incorporation of an adatom on an FCC site of the Ir(111) surface

All surface atoms marked with a 3 relax inwards by 0.3% of the nearest-neighbour distance, a_{nn}. The adatoms relax inwards by 2.5% of a_{nn}. The surface atoms denoted by 1, 2 and 4 all relax outwards, and in the direction of the arrow in the x-y plane. The magnitude of their displacement is 0.6% of a_{nn}. Atoms in the layer just beneath the surface all relax inwards by a small amount (0.05% of a_{nn}).

Figure 8.3 shows a similar diagram for an adatom incorporated on an HCP site.

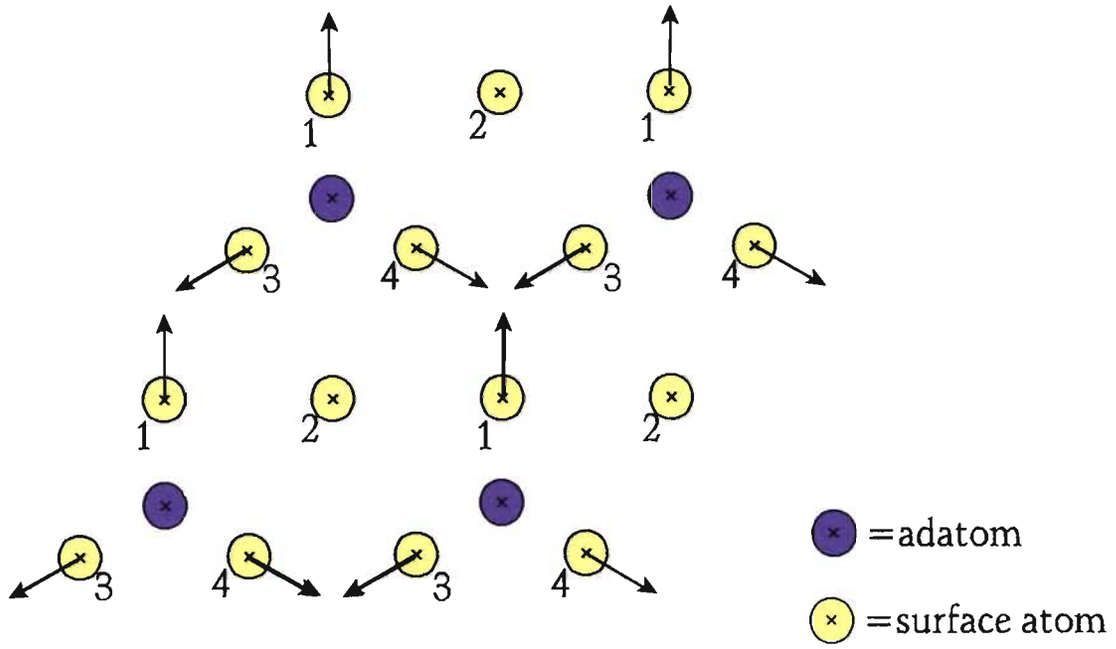

Figure 8.3 Relaxations of atoms due to incorporation of an adatom on an HCP site of the Ir(111) surface.

Each adatom relaxes inwards by a displacement of 2.8% of a_{nn}. The surface atoms marked with a 2 relax inwards by 0.1% of a_{nn}. Surface atoms indicated by 1, 3 and 4 all move in the direction shown by the arrow in the x-y plane, and simultaneously relax outwards. Their overall displacement is 0.7% of a_{nn}. In the plane just below the surface layer, the atom directly beneath the adatom does not move at all, and the remaining three atoms in this 2×2 plane move towards one another, and outwards, by a total displacement of 0.1% of a_{nn}. The atomic relaxations with the adatom on an HCP site are greater than those with the adatom on an FCC site, hence the crossover in the energies before and after relaxation.

8.6 Study of vacancies on the Ir(111) surface

To our knowledge, no investigations have been done to date on the formation of vacancies on the (111) surface of iridium. Table 8.4 below contains the results of our calculations, in which a 2×2 surface supercell was used, the vacancy simply being formed by removing one of these surface atoms. The number of atomic layers was varied between 6 and 9.

Table 8.4 Parameters for Monkhorst-Pack ***k***-point mesh, surface vacancy formation energy in eV, relaxed surface vacancy formation energy in eV, and surface vacancy relaxation energy in meV for 6 and 9 atomic layers for the 2×2 Ir(111) surface

6 atomic layers (3 bulk layers + 1 surface with vacancy layer + 2 vacuum layers)				
***k*-point mesh**	**No. of special *k*-points**	**Surface vacancy energy (eV)**	**Relaxed surface vacancy energy (eV)**	**Relaxation energy (meV)**
(221)	3	8.870	8.589	281
(442)	11	8.991	8.755	236

9 atomic layers (3 bulk layers + 1 surface with vacancy layer + 5 vacuum layers)				
***k*-point mesh**	**No. of special *k*-points**	**Surface vacancy energy (eV)**	**Relaxed surface vacancy energy (eV)**	**Relaxation energy (meV)**
(221)	3	8.620	8.315	305
(442)	11	9.062	8.781	281

The surface vacancy energies are computed in the following manner:

$$E_{vacancy} = E_{supercell} - NE_{bulk} - 2\sigma_{111} \quad ,$$

where N is the number of atoms in the supercell, and σ_{111} is the fully relaxed surface formation energy for the Ir(111) surface.

The relaxations of the individual atoms in the supercell (together with some of the neighbouring supercell atoms) are shown in Figure 8.4.

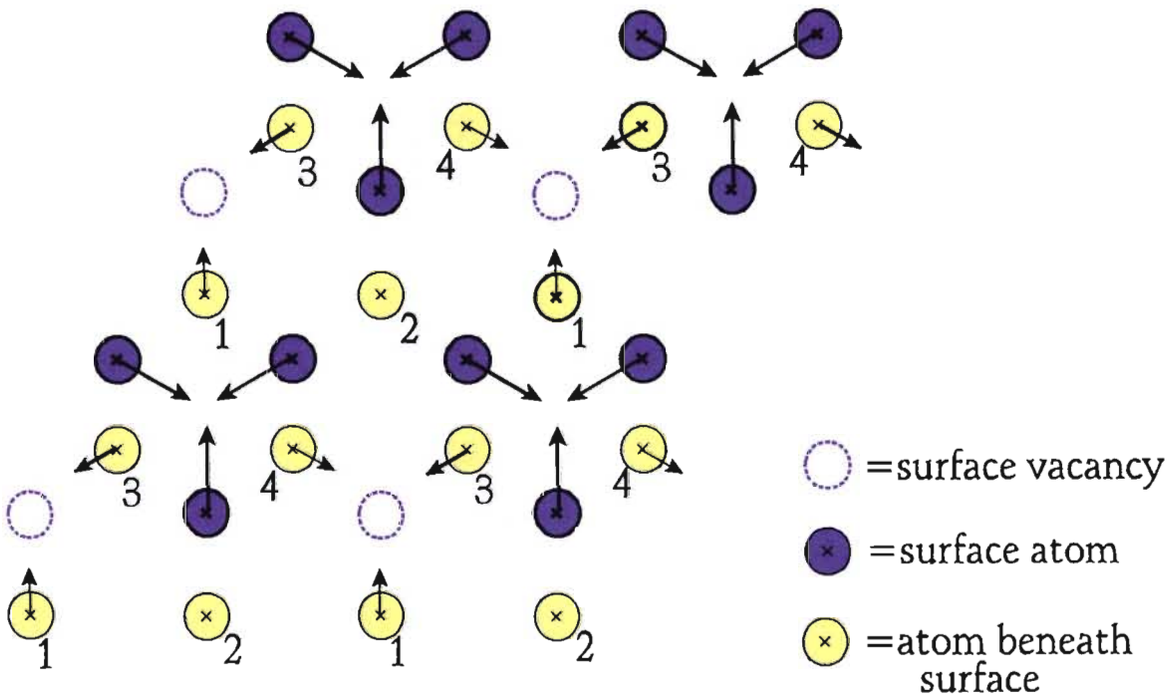

Figure 8.4 Relaxations of atoms due to creation of a surface vacancy on the Ir(111) surface

All of the surface atoms move inwards, and in the directions indicated by the arrows, by a displacement magnitude of 0.8% of a_{nn}. The atoms beneath the surface denoted by a 2 relax inwards by 0.05% of a_{nn}. The remaining atoms beneath the surface, namely those indicated by 1, 3 and 4, move outwards, and in the direction indicated by the arrows. Their overall displacement is 0.2% of a_{nn}.

The movement of the atoms, unlike with the FCC and HCP adatoms, is not in the expected direction if one just considers the atoms to behave as a classical set of balls, where one would expect the three atoms in the plane of the vacancy to move toward the vacancy to fill this gap. The atoms in fact move in the opposite direction. The reason for

this is that each of these atoms originally had 12 nearest-neighbour bonds in this crystallographic structure. The formation of the surface, as well as the formation of the vacancy, has meant that each of these atoms has lost 4 nearest-neighbours. These atoms therefore move toward one another, in an attempt to restore their electronic coordination, and increase their electronic density. The atoms in the layer beneath the surface move toward one another for the same reason, as they have each lost 1 nearest-neighbour in the formation of the vacancy. As an illustration of this point, the nearest-neighbour bonds of the vacancy are shown in Figure 8.5 below.

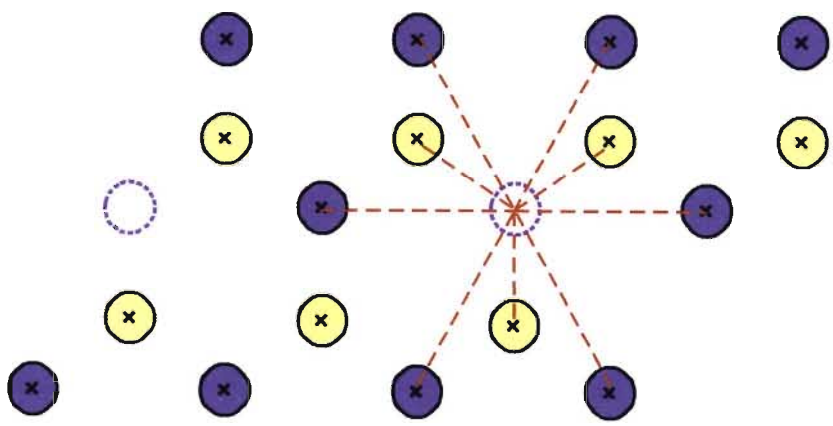

Figure 8.5 Nearest-neighbour bonds of the surface vacancy on the Ir(111) surface

8.7 Conclusion

We have computed the formation energy of a single adatom on the FCC and HCP sites on the Ir(111) surface, and have found, in agreement with experiment, that the HCP is the energetically favoured site. This result is only evident once the atoms have been allowed to fully relax. The accuracy of our calculations is limited due to the finite size effects of the 2×2 surface supercell, and the (442) Monkhorst-Pack $\boldsymbol{k}$-point mesh to which we have been restricted as a result of our computational resources.

In principle, if a large supercell is used in such calculations, so that the slabs on either side of the surface are separated sufficiently, it should only be necessary to sample the Brillouin zone at one point in this direction (ie the z-direction). However, the limitations on our computational resources have meant that remnant interactions between the surfaces can not be disregarded, and the Brillouin zone should hence be sampled accordingly.

In investigating the atomic relaxations, we have found that the atoms in the layer beneath the surface layer are displaced by a small amount when relaxations are fully accounted for. Since the magnitude of their displacement is around 14% of the magnitude of the displacements of the surface layer atoms, it seems an oversimplification to ignore the movement of these atoms in the relaxation process, as many authors have done. Our work is the only work to date which allows for the full relaxation of all of the atoms in the supercell when computing adatom formation energies on the Ir(111) surface.

We have also computed the surface vacancy formation energy, and investigated the associated atomic relaxations. Studies of the surface vacancy on Ir(111) have not been carried out before.

Chapter 9

Concluding Remarks

In this work the density functional theory in the local density approximation has been applied to the study of various physical properties of iridium. The methodology is based on the plane wave pseudopotential method, and we have used the Troullier and Martins[35] pseudopotentials in our work. Electronic structure codes known as BEST have been used, in which the iterative scheme of choice is a variation of the preconditioned steepest descent algorithm, together with a subspace diagonalisation, developed by Chetty *et al.*[6]

In the course of this work, computer codes were developed to enhance the rapid convergence of the total energy through implementation of the modified Broyden mixing scheme used for mixing the charge densities between iterations. Comparisons of this mixing scheme with the linear and Anderson schemes were made, and various input parameters were investigated for optimum implementation of this scheme. Convergence was significantly accelerated with the Broyden mixing scheme.

Bulk properties of iridium were investigated, and the results were compared with other experimental and theoretical results. Our results compare favourably with experiment. The effects of pressure on iridium were then investigated, through implementation of the "pressure dependant bond-orientation model", developed by ourselves as an extension to the model developed by Chetty and Weinert[7]. A claim by experimentalists that a 14-layer superlattice structure exists for iridium under pressure was investigated, and the conclusion to our calculations was that no such structure exists under conditions of hydrostatic pressure. In the experimental process, large uniaxial pressures could exist, giving rise to the possibility of metastable structures. However, it is difficult to predict such structures theoretically. We believe that more experimental work needs to be done to study this system at high pressure.

The ideal and relaxed low-index surfaces of iridium were investigated, and the surface formation energies and interplanar relaxations compared with other theoretical and experimental results. Atoms were allowed to relax fully, and convergence of the total energy results with $\boldsymbol{k}$-point sampling was investigated.

The adsorption of adatoms onto the Ir(111) surface was investigated, with full atomic relaxations being taken into account. The results of our computations showed favourable agreement with experiment, where it was found that an HCP adatom site is energetically favoured over the expected FCC adatom site. No other theoretical or semi-empirical work done on this system has allowed for full relaxation of the atoms. We also computed the energy of formation of the surface vacancy, which has not previously been calculated.

In future work we intend to explore the energy of formation of dimers and trimers of various geometries on the Ir(111) surface. In order to do this, we will need to consider surface unit cells of at least 3×3 in dimension. We further intend to study diffusion barriers for the migration of single adatoms, as well as dimers and trimers, across the surface. In each of these calculations we will consider full atomic relaxations, as these

have not been taken into account in any previous work on these systems. The continuation of this work is contingent on us acquiring more powerful computational resources.

Appendix A

Adaptations to the Density Functional Theory

The density functional theory is an exact ground state theory. Due to its variational approach, it is not possible to apply the Kohn-Sham scheme in a straightforward manner to the study of the excited states of a system. The usual practice for such systems is to apply numerically intensive Greens-function methods, or quantum-chemical methods for smaller systems. A number of adaptations to the basic DFT have been made in recent years to achieve the study of excited systems.

The energy of exchange and correlation are incorporated into the exchange-correlation potential in the Kohn-Sham formulation. This potential is approximated through schemes such as the LDA and GGA. Various adaptations to the DFT have been to more accurately account for this energy.

In the BEST codes, the computational cost of implementing DFT is $O(N^2 \ln N)$, where N is the number of atoms in the system. This limits the size of the system which can be investigated. More efficient methods are constantly being sought, ideally methods which scale linearly with system size, otherwise known as $O(N)$ methods.

This appendix gives a very brief overview of some of the adaptations that have been made to the DFT to account for these and other limitations.

Density matrix theory has been developed in an attempt to find a more efficient method than the DFT. The central quantity in this theory is the two-particle density matrix $n(\boldsymbol{r}_1, \boldsymbol{r}_2; \boldsymbol{r}_1', \boldsymbol{r}_2')$. An example of one such formulation[84] is one which involves the expansion of the density matrix in terms of average coordinates

$$\boldsymbol{R} = \frac{(\boldsymbol{r}_1 + \boldsymbol{r}_2)}{2} \quad , \tag{A.1}$$

and relative coordinates

$$\boldsymbol{r} = (\boldsymbol{r}_1 - \boldsymbol{r}_2) \quad . \tag{A.2}$$

Due to the factorisation of the Coulomb and exchange integrals in this formulation, the energy expression becomes very simple. However, the kinetic energy is represented in real space, and is the hardest term to compute accurately. Finite element methods require too small a grid size to make the computation efficient.

In density matrix theory, linear scaling with system size is ensured by enforcing the following cut-off:

$$n(\boldsymbol{r},\boldsymbol{r}') = 0, \quad |\boldsymbol{r}-\boldsymbol{r}'| > R_c \quad . \tag{A.3}$$

In this way, the information in the density matrix is dependent only on the local environment, and hence the total amount of information is linear in the number of atoms in the system, N. This theory applies to both the ground and excited states of the system.

Time-dependent density functional theory[85] (TDDFT) was originally designed to explore time-dependent phenomena in a system. More recently it has been applied to excited states, and has been used in the investigation of optical excitations in which electron-hole pairs are formed[86]. It involves an initial solution of the ground-state Kohn-Sham equations, followed by an iterative solution of a first-order representation of the Kohn-Sham equations. Here an approximation to the first functional derivative of the time-dependent exchange correlation potential is needed. This is given by

$$f_{xc}(\boldsymbol{r},\boldsymbol{r}',t,t') = \frac{\partial v_{xc}(\boldsymbol{r},t)}{\partial n(\boldsymbol{r}',t')} \quad . \tag{A.4}$$

This is called the exchange correlation kernel. Various approximations for this kernel have been made. The adiabatic local density approximation (ALDA) is the most commonly used one in TDDFT. This approximation is discussed further in Appendix C.

Instead of approximating both the exchange and correlation energies, as is the case with most applications of density functional theory, the *exact exchange* DFT has been developed to give an exact expression for the exchange energy, and an approximation for the energy of correlation, for example by means of the LDA or GGA correlation functionals. Better approximations for energy gaps and structural properties are obtained from this extension to DFT[87].

In *spin-density functional theory* the external field can differ for the two spin components. A one-to-one correspondence is then established between the spin densities $n_\uparrow(\boldsymbol{r},t)$ and $n_\downarrow(\boldsymbol{r},t)$, and the potentials $v_\uparrow(\boldsymbol{r},t)$ and $v_\downarrow(\boldsymbol{r},t)$. Hence all quantities can be expressed as

functions of the two spin densities. The approximation that is generally used for the exchange-correlation energy is the local spin density approximation (LSDA)[28].

Gonze *et al*[88] pointed out that the basic DFT is not a sufficiently accurate theory for describing a crystal in a finite electric field, and suggested that the bulk dielectric properties in such a crystal require the state of the system to be a functional of both the density and the polarization. Martin *et al*[89] constructed a generalised form for the DFT, namely *density-polarization functional theory* (DPFT), in which the dielectric behaviour of materials can be completely described.

In large systems consisting of heavy atoms, a relativistic correction may be required. *Relativistic density functional theory*[90] is an extension to DFT which has been developed for such systems.

Appendix B

The Ceperley-Alder Form of the LDA

B.1 The variational Monte Carlo method

In variational Monte Carlo the energy of a many-body trial wavefunction $\Psi(R)$is computed for a known Hamiltonian operator in the following way:

$$E = \langle \Psi | H | \Psi \rangle = \frac{\int \Psi^*(\boldsymbol{R})\ H\ \Psi(\boldsymbol{R})\ d\boldsymbol{R}}{\int \Psi^*(\boldsymbol{R})\ \Psi(\boldsymbol{R})\ d\boldsymbol{R}} \quad , \tag{B.1}$$

where $\boldsymbol{R}$ is a 3N dimensional position coordinate of N particles. In the Monte Carlo method a sequence of $\boldsymbol{R}$'s is generated using the Metropolis random walk algorithm. By the Rayleigh-Ritz variational principle, the energy functional provides an upper bound to the exact ground state energy and will be a minimum when $\Psi(\boldsymbol{R})$ is equal to the exact ground state wavefunction.

A common form used for the trial wavefunction $\Psi(\boldsymbol{R})$ is the Slater-Jastrow type, in which a sum of Slater determinants of single-particle spin-dependent orbitals is used together with a pair-correlation factor (called the Jastrow factor):

$$\Psi(\boldsymbol{R}) = \sum_n D_n^{\uparrow} D_n^{\downarrow} \exp\left[\sum_{I,i<j} u(r_{iI}, r_{jI}, r_{ij}) \right] \quad . \tag{B.2}$$

Here I corresponds to the positions of the ions, and i and j to electron positions. The Jastrow factor u needs to take cusp conditions into account, which result from derivative discontinuities in the wavefunction at potential collision points between charged particles. The Jastrow factor is then adjusted variationally to achieve the lowest possible energy.

B.2 The Ceperley-Alder work on the electron gas

Ceperley and Alder[91] developed a method in which the variational Monte Carlo technique is applied in order to calculate the properties of an electron gas in its ground state. They extended the solution for the many-boson problem to fermions, where the wavefunctions are required to be anti-symmetric. The calculation was carried out in two steps.

The first step treats the nodes where the trial wavefunction vanishes as absorbing barriers to the process of diffusion. This yields the "fixed-node" energy, which is equivalent to the boson energy, and forms an upper bound to the correct ground-state energy of the system.

The second step, the "nodal relaxation" step, involves reversal of the sign of the contribution of a random walk as it crosses the node of the trial wavefunction. One hence obtains a set of positive walks, in which the nodes have been crossed an even number of times, and a set of negative walks, where there has been an odd number of node crossings.

The difference between these two probability densities, namely those from the first and second steps, yields a representation for the anti-symmetric wavefunction. Ceperley and Alder used the nodes of the Hartree-Fock wavefunction for the trial wavefunction.

Implementation of this method, if run for a sufficiently long time on the computer, can give as precise a solution for the ground state properties of the electron gas as is required.

B.3 The Perdew and Zunger parametrisations

For the unpolarized homogeneous electron gas, Perdew and Zunger[92] derived the following parametrised expressions from the work of Ceperley and Alder:

$$\varepsilon_{XC}(r_s) = \varepsilon_X(r_s) + \varepsilon_C(r_s) \quad , \tag{B.3}$$

where

$$\varepsilon_X(r_s) = -\frac{0.4582}{r_s} \quad , \tag{B.4}$$

and

$$\varepsilon_C(r_s) = \left\{ \begin{array}{ll} \dfrac{-0.1423}{(1+1.0529\sqrt{r_s}+0.3334r_s)} & \text{for } r_s \geq 1 \\ -0.0480+0.0311\ln r_s-0.0116r_s+0.0020r_s\ln r_s & \text{for } r_s < 1 \end{array} \right\} . \qquad \textbf{(B.5)}$$

Appendix C

Extensions to the Local Density Approximation

C.1 Limitations of the local density approximation

The LDA equates the exchange-correlation energy for the local value of the density with that of a uniform electron gas which has the same density. It was initially formulated for systems with slowly varying electron densities. Although the LDA has yielded surprisingly accurate results, there are a number of instances in which it does not yield satisfactory results. Where a system is far from being homogeneous, for instance at a surface, the LDA tends to fail in its representation of the system. In addition, there is a general tendency towards overestimation of cohesive energies. In particular, in applications to molecules, the molecular binding energies are consistently in error. This is due to the underestimation of the exchange-correlation contribution at regions of low electron density. The dielectric constant is also overestimated by 10-40% in the LDA, as a

result of the neglect of a polarization- dependent exchange correlation field. The LDA also fails for excited state properties. The band gaps in insulators, for instance, are underestimated by as much as 2eV.

C.2 Extensions to the local density approximation

The *local spin density approximation* (LSDA) applies to open-shell systems and magnetic solids. Here the exchange-correlation energy not only depends on the local electron density, but also on the local spin density. This is the form of the exchange-correlation functional which is used in spin-density functional theory.

The *adiabatic local density approximation* (ALDA) has become the standard approximation in the time dependent density functional theory (TDDFT), which has been discussed in Appendix A. The general form for the time-dependent exchange correlation kernel is given in equation **(A.4)** in Appendix A. In the ALDA, the long wavelength limit for this kernel is equal to that for the static exchange-correlation functional for the homogeneous electron gas in reciprocal space:

$$f_{xc}^{ALDA} = \lim_{\boldsymbol{G} \to 0} f_{xc}^{hom}(\boldsymbol{G}) \quad . \tag{C.1}$$

It can be expressed in terms of the exchange correlation energy per particle in the homogeneous electron gas $\varepsilon_{xc}^{hom}(n(\boldsymbol{r}))$ in the following way[93]:

$$f_{xc}^{ALDA} = \frac{d^2}{dn^2}\left[n\, \varepsilon_{xc}^{hom}(n) \right] \quad . \tag{C.2}$$

The ALDA is computationally simple and efficient, and it is claimed that to date there are no approximations which lead to better exchange correlation kernels than this one[94]. It is therefore the most frequently used approximation within the TDDFT.

Examples of other approximations which have been used in TDDFT are *the frequency-dependent LDA*[95], which is an attempt to overcome the ambiguity which arises when the LDA is applied to non-local quantities; the *random-phase approximation*[93], in which all dynamic exchange-correlation effects are ignored; the *Petersilka-Gossman-Gross*[96] derivation, in which an exact-exchange kernel is constructed, and correlation effects are ignored; and the *Burke-Petersilka-Gross*[97] approximation, which is a hybrid formula designed to improve on excitation spectra for small atoms. We will not look at these approximations in detail here.

Kohn and Mattsson[98] have developed a technique for handling inhomogeneities at the edges of a system. They proposed an exchange-correlation functional specifically designed for the edge part of the system, and a separate functional for the interior region. They did this by introducing an *edge electron gas* from which the functional is derived. Armiento and Mattsson[99] extended this idea to apply to systems which may contain inhomogeneities throughout, not just in the edge region. They proposed the use of different functionals in the different regions of the system.

Appendix D

Sampling of the Brillouin Zone

D.1 Introduction

The application of Bloch's theorem for a periodic structure allows real space integrals for an infinitely extended system to be replaced by reciprocal space integrals over the first Brillouin zone. These integrals may be approximated through summation of the integrand values at a finite number of points in the Brillouin zone. These points are called the special $\boldsymbol{k}$-points. A sufficiently dense set of $\boldsymbol{k}$-points is required for convergence of the results.

Baldereschi[100] developed a method for finding a single point in the Brillouin zone, called the "mean value point" $\boldsymbol{k}^*$, which would give the best approximation to the averaging of some function $f(\boldsymbol{k})$ over the entire zone:

$$\bar{f} = \frac{\Omega}{(2\pi)^3} \int f(\boldsymbol{k})\, d\boldsymbol{k} = f(\boldsymbol{k}^*) \quad . \tag{D.1}$$

Chadi and Cohen[101] extended this to generate a number of representative points in the Brillouin zone. Monkhorst and Pack[45] later developed a more systematic way of producing $\boldsymbol{k}$-points within the Brillouin zone over which integrations over the zone could be done. This scheme, which is briefly outlined below, ensures that the $\boldsymbol{k}$-points are distributed homogeneously throughout the Brillouin zone.

D.2 Outline of the Monkhorst-Pack scheme

In the Monkhorst-Pack scheme, a sequence of numbers, u_r, is generated by the expression

$$u_r = (2r - q - 1) / 2q \quad , \tag{D.2}$$

for r running from 1 through to q. Here q is an integer value which determines the number of special points to be chosen. We then define a set of distinct points

$$\boldsymbol{k}_{prs} = u_p \boldsymbol{b}_1 + u_r \boldsymbol{b}_2 + u_s \boldsymbol{b}_3 \quad , \tag{D.3}$$

where the $\boldsymbol{b}_i$ are the reciprocal lattice vectors. From **(D.3)** we thus have q^3 uniformly spaced points in the Brillouin zone. Making use of the lattice point group symmetry, we can significantly reduce this number of points. To do this we define a set of vectors, called a "star", in the following way:

$$A_m(\boldsymbol{k}) = N_m^{-½} \sum_{|\boldsymbol{R}|=C_m} e^{i\boldsymbol{k}\cdot\boldsymbol{R}} \quad , \tag{D.4}$$

where the $\boldsymbol{R}$ vectors are the Bravais lattice vectors which are related to each other by the lattice point group operations. N_m is the number of terms in the mth star of $\boldsymbol{R}$.

Thus for a function $f(\boldsymbol{k})$ which we wish to integrate in reciprocal space, we would approximate this integral by the following summation over the set of $\boldsymbol{k}_i$ points:

$$F(\boldsymbol{k}_i) = \sum_m F_m \, A_m(\boldsymbol{k}_i) \quad , \tag{D.5}$$

where

$$F_m = \frac{1}{q^3} \sum_{j=1}^{P(q)} w_j \, F(\boldsymbol{k}_j) \, A_m(\boldsymbol{k}_j) \quad . \tag{D.6}$$

Here $P(q)$ is the symmetry-dependent number of points from those generated in **(D.3)**, and w_j is the weighting associated with each $\boldsymbol{k}_j$. This weighting indicates the number of $\boldsymbol{k}$-vectors that are represented by each special point through the symmetry operations of the relevant crystallographic structure.

Appendix E

Fast Fourier Transforms

The plane wave representation of the molecular dynamics equation of motion (the Car-Parrinello method) can be written in the following form

$$\mu \ddot{c}_{i,\boldsymbol{k}+\boldsymbol{G}} = -\left[\frac{\hbar^2}{2m}|\boldsymbol{k}+\boldsymbol{G}|^2 - \lambda_i\right] c_{i,\boldsymbol{k}+\boldsymbol{G}} - \sum_{\boldsymbol{G}'} V_T(\boldsymbol{G}-\boldsymbol{G}')\, c_{i,\boldsymbol{k}+\boldsymbol{G}'} \quad , \tag{E.1}$$

where μ represents a fictitious mass associated with the electronic wavefunctions, and the λ_i are Lagrange multipliers which ensure orthogonality of the wavefunctions. The total potential $V_T(\boldsymbol{G})$ is given by

$$V_T(\boldsymbol{G}-\boldsymbol{G}') = V_{ion}^{Ps}(\boldsymbol{G}-\boldsymbol{G}') + V_H(\boldsymbol{G}-\boldsymbol{G}') + V_{XC}(\boldsymbol{G}-\boldsymbol{G}') \quad . \tag{E.2}$$

Here the ionic pseudopotential is purely local. Written in another way,

$$\mu \ddot{c}_{i,\boldsymbol{k}+\boldsymbol{G}} = -\left[\frac{\hbar^2}{2m}|\boldsymbol{k}+\boldsymbol{G}|^2 - \lambda_i\right] c_{i,\boldsymbol{k}+\boldsymbol{G}} - \int \left[V_T(\boldsymbol{r})\,\psi(\boldsymbol{r})\right] e^{i(\boldsymbol{k}+\boldsymbol{G})\cdot\boldsymbol{r}} d^3\boldsymbol{r} \quad . \tag{E.3}$$

Hence the product of the Kohn-Sham Hamiltonian with the wavefunction has been divided into two parts, one which is diagonal in real space, and the other in reciprocal space. The wavefunctions are therefore Fourier transformed from reciprocal into real space, whereupon the contribution to the acceleration by operation of the potential on these wavefunctions is calculated in real space. These contributions are then Fourier transformed into reciprocal space.

One therefore requires an efficient means of transforming between real and reciprocal space.

The definition of the discrete Fourier transform of an input sequence $f[n]$ of length N is

$$F(k) = \sum_{n=0}^{N-1} f[n]\, e^{2\pi i / N} \quad , \qquad \textbf{(E.4)}$$

the solution of which is an $O(N^2)$ process, as is illustrated in Figure E.1. This is because the summation from $n=0$ to N-1 occurs for each index k, of which there are N.

By way of illustration, we have performed the discrete Fourier transform on number sequences of increasing length, and have generated a graph of time taken for the transform plotted against system size (Figure E.1 on the following page). This graph illustrates the $O(N^2)$ nature of the discrete transform.

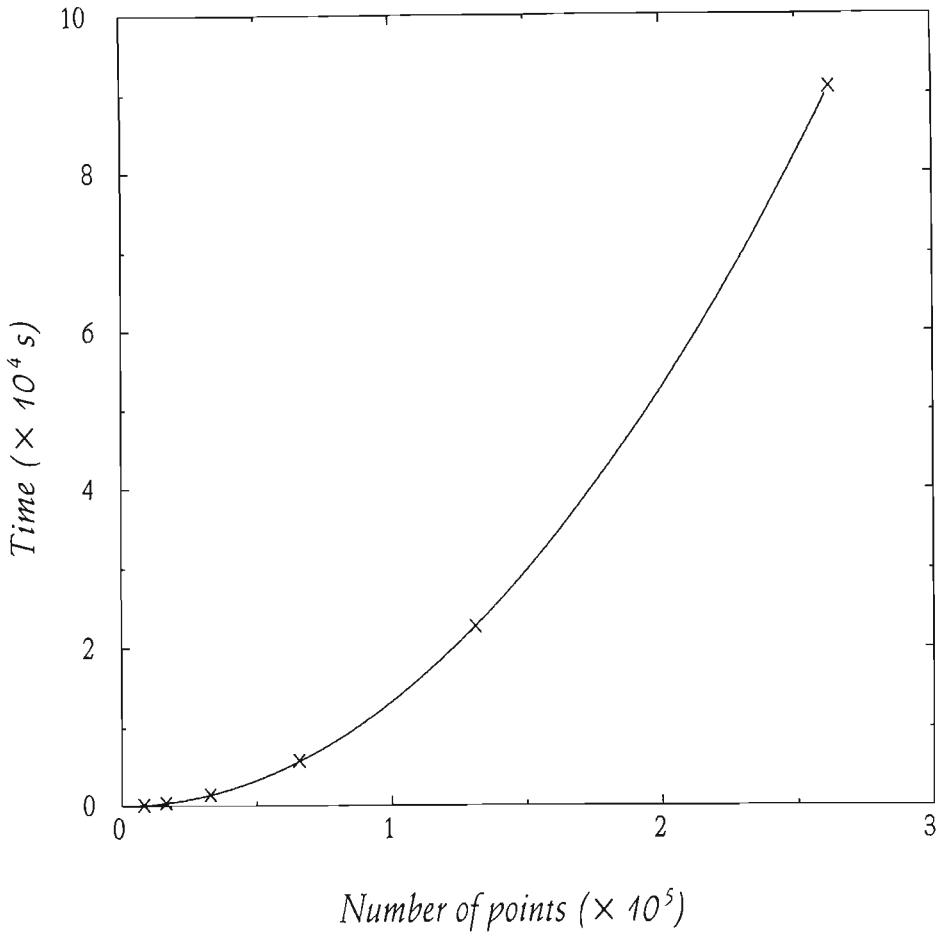

Figure E.1 Discrete Fourier transform applied to number sequences of increasing length. Computational time scales quadratically with number of points.

A much more efficient method is the fast Fourier transform (FFT), which requires $O(N \ln N)$ operations. Danielson and Lanczos[102] developed a lemma, in which they proved that a discrete Fourier transform of length N can be rewritten as the sum of two discrete Fourier transforms, each of length $N/2$. One of these is formed from the even-numbered points of the original N, the other from the odd-numbered points. This lemma can be used recursively, dividing each of the two sets obtained above into two, leaving

four sets of length $N/4$, and so on, until one is left with transforms of length one. At this point one is left with a one-point transform corresponding with the pattern of e's and o's (corresponding to an even- or odd-numbered subset of data at each division). In order to identify which input number f_n is associated with the one-point transform, the value of n associated with the pattern of e's and o's can be retrieved by a process is called bit-reversal. Here, the pattern of e's and o's is reversed, and each e is associated with a 0, each o with a 1. This yields a binary number which is precisely the number n corresponding to f_n.

After the process of bit-reversal, adjacent single-point transforms are then combined into 2-point transforms, which are combined into 4-point transforms, and so on until the entire data set is combined into one transform. Each operation takes $O(N)$ operations, and since there are $\ln N$ combinations, the entire algorithm is an $O(N \ln N)$ process.

The Fourier transform of a wavefunction from reciprocal space into real space hence requires $N_{RS} \ln N_{RS}$ operations, where N_{RS} is the number of points on the real space grid. N_{RS} is approximately 16 times the number of plane waves in the wavefunction. This is because the charge density has components with wave vectors up to double the cut-off wave vector for the electronic wavefunctions, requiring the FFT grid to have double the density of the real space grid in each direction. Performing a Fast Fourier Transform on a single band therefore requires $N_{FFT} = 16\, N_{PW} \ln N_{PW}$ operations.

The fast Fourier transform, as given in Numerical Recipes[103], has been applied to sequences of increasing length, and the consequent graph of the number of operations plotted against system size is shown in Figure E.2. This graph illustrates the $O(N \ln N)$ nature of the FFT.

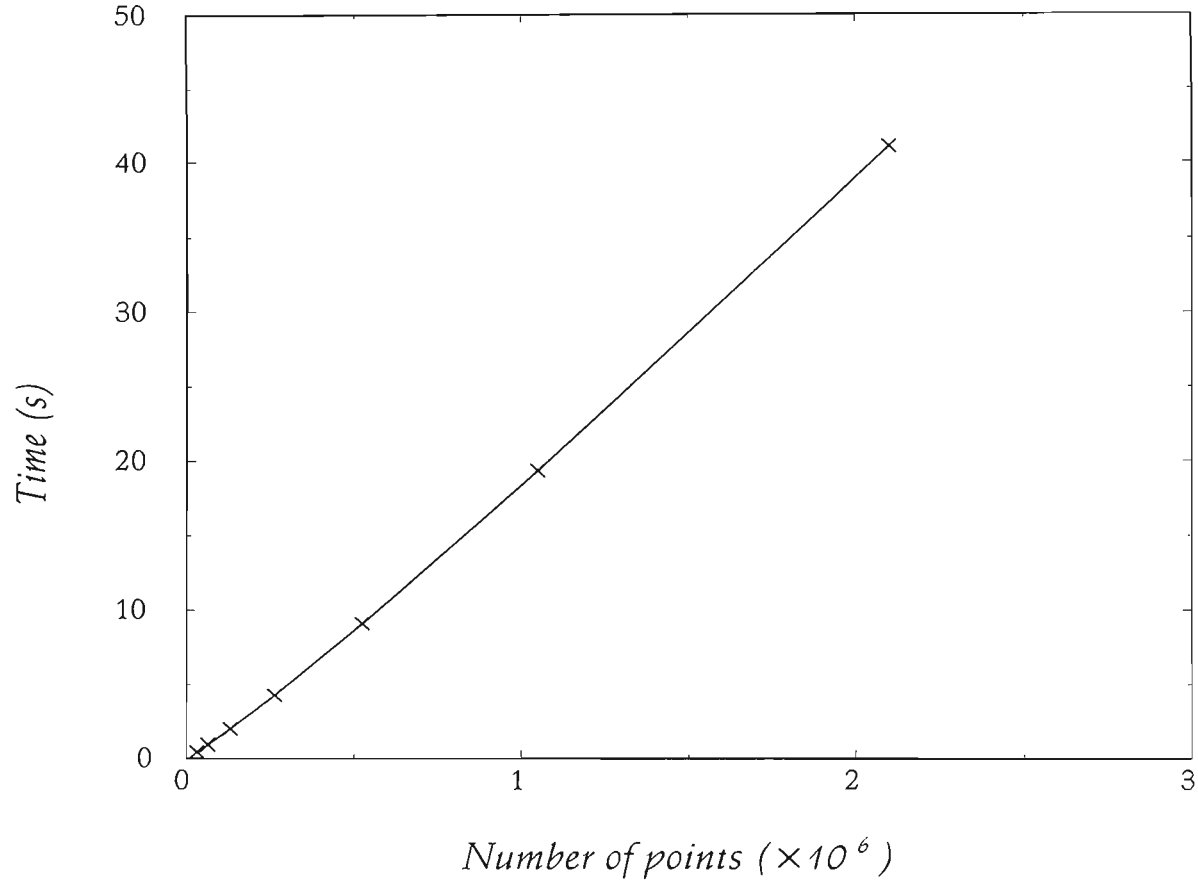

Figure E.2 Fast Fourier transform applied to number sequences of increasing length (N). Time scales as ($N \ln N$).

References

1. S.C. Wang and G. Ehrlich, Phys. Rev. Lett. **62**, 2 297 (1989)
2. S.C. Wang and G. Ehrlich, Surf. Sci. **217**, L 397 (1989)
3. S.C. Wang and G. Ehrlich, Surf. Sci. **224**, L 997 (1989)
4. S.C. Wang and G. Ehrlich, Phys. Rev. Lett. **68**, 1 160 (1992)
5. C. Chen and T.T. Tsong, Phys. Rev. B **41**, 12 403 (1990)
6. N. Chetty, M. Weinert, T.S. Rahman and J.W. Davenport, Phys. Rev. B **52**, 6 313 (1995)
7. N. Chetty and M. Weinert, Phys. Rev. B **56**, 10 844, (1997)
8. P. Hohenberg and W. Kohn, Phys. Rev. **136**, 3 864 (1964)
9. R. Car and M. Parrinello, Phys. Rev. Lett. **55**, 2 471 (1985)
10. D.F. Shanno, Math. Oper. Res. **3**, 244 (1978)
11. Y. Cerenius and Dubrovinsky, J. Alloys and Compounds **306**, 26, (2000)
12. J.C. Slater, Phys. Rev. **81**, 385 (1951)
13. J.C. Slater, Int. J. Qu. Chem. Symp. **9**, 7 (1975)
14. E.P. Wigner, Phys. Rev. **46**, 1 002 (1934)
15. D. Pines, *"Elementary Excitations in Solids"*, W. A. Benjamin, Inc.,New York (1963)
16. M. Gell-Mann and K. Brueckner, Phys. Rev. **106**, 364 (1957)
17. J. Perdew and A. Zunger, Phys. Rev. B **23**, 5 048 (1981)
18. D.M. Ceperley and B.J. Alder, Phys. Rev. Lett. **45**, 566 (1980)
19. W. Kohn and P. Vashishta, in *"Inhomogeneous Electron Gas"*, N.H. March and S. Lundqvist (Eds), Plenum, New York (1983)
20. D.C. Langreth and M.J. Mehl, Phys. Rev. Lett. **47**, 446 (1981)

21. D.C. Langreth and M.J. Mehl, Phys. B **28**, 1 809 (1983)

22. http://www.physics.ohio-state-edu/aulbur/bdft/bdft7.html

23. J.P. Perdew, Phys. Rev. Lett. **55**, 1 665 (1985)

24. D.C. Langreth and J.P. Perdew, Phys. Rev. B **21**, 5 469 (1980)

25. J.P. Perdew, in *"Electronic Structure of Solids '91"* , P. Ziesche and H. Eschrig (Eds), Akademie-Verlag, Berlin (1991)

26. I-H. Lee and R.M. Martin, Phys. Rev. B **56**, 7 197 (1997)

27. J.P. Perdew, K. Burke and M. Erzerhof, Phys. Rev. Lett. **77**, 3 865 (1996)

28. W. Kohn and C.J. Sham, Phys. Rev. **140**, A 1 133 (1965)

29. V. Heine, Sol. St. Phys. **24**, 1, (1970)

30. C. Herring, Phys. Rev. **57**, 1 169, (1940)

31. J.C. Slater, Phys. Rev. **51**, 846, (1937)

32. C. Herring and A.G. Hill, Phys. Rev. **58**, 132, (1940)

33. J.C. Philips and L. Kleinman, Phys. Rev. **116**, 287 (1959)

34. E. Antoncik, J. Phys. Chem. Solids **10**, 314, (1959)

35. N. Troullier and J.L. Martins, Phys. Rev. B **43**, 1 993, (1991)

36. G.B. Bachelet, D.R.Hamann and M. Schlüter, Phys. Rev. B **26**, 4 199 (1982)

37. G.P. Kerker, J. Phys. C **13**, L 189 (1980)

38. X. Gonze, P. Käckell and M. Scheffler, Phys. Rev. B **41**, 12 264, (1990)

39. M. Boon, M. Methfessel and F. Mueller, J. Phys. C **19**, 5 337 (1986)

40. G. Lehmann and M. Taut, Phys. Status Solidi B **54**, 469 (1972)

41. P.E. Blöchl, O. Jepsen and O.K. Anderson, Phys. Rev. B **49**, 16 223 (1994)

42. C.J. Pickard and M.C. Payne, Phys. Rev. B **59**, 4 685 (1999)

43. M. Methfessel, M. Boon and F. Mueller, J. Phys. C **16**, 1 949 (1983)

44. J.E. Müller and J.W. Wilkins, Phys. Rev. B **29**, 4 331 (1984)

45. H.J. Monkhorst and J.D. Pack, Phys. Rev. B **13**, 5 188, (1976)

46. P.P. Ewald, Ann. Phys. (Leipzig) **64**, 253 (1921)

47. R.E. Cohen, M.J. Mehl and D.A. Papaconstantopoulos, Phys. Rev. B **50**, 14 694 (1994)

48. M.J. Mehl and D.A. Papaconstantopoulos, Phys. Rev. B **54**, 4 519 (1996)

49. http://www.accelrys.com/technology/qm/erich/choices.html

50. R. Fletcher and C.M. Reeves, Comp. J. **7**, 149 (1964)

51. http://cmt.dur.ac.uk/Castep_Lectures1/lecture15.pdf

52. H. Hellmann, in *Einführung in die Quantumchemie*, Deuticke, Leipzig, (1937)

53. R.P. Feynman, Phys. Rev. **56**, 340 (1939)

54. D.F. Shanno, Math. Oper. Res. **3**, 244 (1978)

55. S.S. Oren and E. Spedicato, Math. Programming **10**, 70 (1976)

56. D.G. Anderson, J. Assoc. Comput. Mach. **12**, 547 (1964)

57. D.R. Hamann, Phys. Rev. Lett. **42**, 662 (1979)

58. C.G. Broyden, Math. Comput. **19**, 577 (1965)

59. G.P. Srivastava, J. Phys. A **17**, L 317 (1984)

60. http://www.speclab.com/elements/iridium.htm

61. C. Kittel, *Introduction to Solid State Physics*, 6th ed. (Wiley, New York, 1986)

62. A.S. Ivanov, M.I. Katsnelson, A.G. Mikhin, Yu.N. Osetskii, A.Yu. Rumyantsev, A.V. Trefilov, Yu.F. Shamanaev and L.I. Yakovenkova, Phil. Mag. B **69**, 1 183, (1994)

63. B.A. Greenberg, M.I. Katsnelson, V.G. Koreshkov, Yu.N. Osetskii, G.V. Peschanskikh, A.V. Trefilov, Yu.F. Shamanaev and L.I. Yakovenkova, Phys. Status Solidi (b), **158**, 441, (1990)

64. R. Heid, K-P. Bohnen, K. Felix, W. Reichardt and K.M. Ho, J. Phys. Cond. Matt. **10**, 7 967, (1998)

65. A. Filippetti and V. Fiorentini, Surf. Sci. **377**, 112 (1997)

66. G. Boisvert and L.J. Lewis, Phys. Rev. B **52**, 9 078, (1995)

67. Y. Cerenius and Dubrovinsky, J. Alloys and Compounds **306**, 26, (2000)

68. Y.S. Touloukian, R.K. Kirby, R.E. Taylor and P.D. Deai, *Thermophysical Properties of Matter, Thermal Expansion - Metallic Elements and Alloys* Vol. 12, Plenum, New York (1975)

69. V. Fiorentini, M. Methfessel and M. Scheffler, Phys. Rev. Lett. **71**, 1 051 (1993)

70. W.R. Tyson and W.A. Miller, Surf. Sci. **62**, 267 (1977)

71. P. van Beurden and G.J. Kramer, Phys. Rev. B **63**, 165 106 (2001)

72. P.R. Watson, M.A. Van Hove and K. Hermann, *Atlas of Surface Structures: Based on the NIST Surface Structure Database (SSD)* American Chemical Society, Washington, **1A** (1994)

73. B. Piveteau, D. Spanjaard and M. C. Desjonquères, Phys. Rev. B **46**, 7 121, (1992)

74. G. Boisvert, L.J. Lewis, M.J. Puska and R.M. Nieminen, Pjys. Rev. B **52**, 9 078 (1995)

75. S. Papadia, B. Piveteau, D. Spanjaard and M.C. Desjonquères, Phys. Rev. B **54**, 14 720 (1996)

76. M. Habar, S. Ouannasser, L. Stauffer, H. Dreyssé and L.T. Wille, Surf. Sci. **352-354**, 5 (1996)

77. M. Habar, L. Stauffer, H. Dreyssé and L.T. Wille, J. Phys.: Condens. Matter **12**, 7 005 (2000)

78. J.C. Hamilton, M.R. Sørensen and A.F.Voter, Phys. Rev. B **61**, R 5 125 (2000)

79. K-D. Shiang, C.M. Wei and T.T. Tsong, Surf. Sci. **301**, 136 (1994)

80. C.M. Chang and C.M. Wei, Phys. Rev. B **54**, 17 083 (1996)

81. S.C. Wang and G. Ehrlich, Surf. Sci. **239**, 301 (1990)

82. O.S. Trushin, M. Kotrla and F. Máca, Surf. Sci. **389**, 55 (1997)

83. P. van Beurden and G.J. Kramer, Phys. Rev. B **63**, 165 106 (2001)

84. F.R. Manby, P.J. Knowles and A.W. Lloyd, Chem. Phys. Lett. **335**, 409 (2001)

85. E. Runge and E.K.U. Gross, *"Density Functional Theory"*, Springer, Berlin (1990)

86. K. Tatarczyk, A. Schindlmayr and M. Scheffler, Phys. Rev. B **63**, 235 106 (2001)

87. http://www.physics.ohio-state-edu/aulbur/bdft/bdft14.html

88. X. Gonze, P. Ghosez and R.W. Godby, Phys. Rev. Lett. **74**, 4 035 (1995)

89. R.M. Martin and G. Ortiz, Phys. Rev. B **56** , 1 124 (1997)

90. R.M. Dreizler and E. Engel, *"Density Functionals: Theory and Applications"*, Daniel Joubert (Ed.), Springer (1998)

91. D.M. Ceperley and B. J. Alder, Phys. Rev. Lett. **45**, 566, (1980)

92. J. Perdew and A. Zunger, Phys. Rev. B **23**, 5 048 (1981)

93. K. Tatarczyk, A. Schindlmayr and M. Scheffler, Phys. Rev. B **63**, 235 106 (2001)

94. S.J.A. van Gisbergen, J.G. Snijders and E.J. Baerends, J. Chem. Phys. **109**, 10 657 (1998)

95. E.K.U. Gross and W. Kohn, Phys. Rev. Lett. **55**, 2 850 (1985)

96. M. Petersilka, U.J. Gossmann and E.K.U. Gross, Phys. Rev. Lett. **76**, 1212 (1996)

97. K. Burke, M. Petersilka and E.K.U. Gross, in *Recent Advances in Density Functional Methods*, P. Fantucci and A. Bencini (Eds) World Scientific, Vol III, Singapore, 2002

98. W. Kohn and A.E. Mattsson, Phys. Rev. Lett. **81**, 3 487 (1998)

99. R. Armiento and A.E. Mattsson, Phys. Rev. B **66**, 165 117 (2002)

100. A. Baldereschi, Phys. Rev. B **7**, 5 212, (1973)

101. D.J. Chadi and M.L. Cohen, Phys. Rev. B **8**, 5 747, (1973)

102. G.C. Danielson and C. Lanczos, Journal of the Franklin Institute **233**, 365, (1942)

103. W.H. Press, S.A. Teukolsky, W.T. Vetterling and B.P. Flannery, *Numerical Recipes in FORTRAN - The Art of Scientific Computing (2nd Edition)*, Cambridge Univ. Press, Cambridge (1992)

Biography

Sharon Grussendorff was born in 1969 in Pietermaritzburg, South Africa, and grew up in a number of diverse South African towns, such as Mooi River, Mafikeng, Pretoria, and Port Shepstone. Sharon is aware of the negative consequences of the educational inequity in South Africa, and has thus for the past 10 years been involved in lecturing and coordinating the Physics course of the Science Foundation Programme, which is a year-long programme run at the University of Natal, aimed at laying a sound educational foundation in the sciences, and broadening access to tertiary education, for those who would not otherwise have this opportunity due their disadvantaged educational backgrounds.

Sharon has been fully involved in university life in her time of study, having been chair of the Students' Christian Association, an assistant Warden at the Denison student residence, and a member of the university squash team. She is also very involved in her church, belongs to a bookclub, and regularly plays tennis and squash for exercise and enjoyment.